Optical Microring Resonators for Photoacoustic Imaging and Detection

by

Sung-Liang Chen

A dissertation submitted in partial fulfillment
of the requirements for the degree of
Doctor of Philosophy
(Electrical Engineering)
in The University of Michigan
2012

Doctoral Committee:

Professor L. Jay Guo, Chair
Professor Theodore B. Norris
Professor Herbert Graves Winful
Assistant Professor Xueding Wang
Associate Research Scientist John A. Nees

To my parents and siblings: Your love and dedication made this possible

Acknowledgements

It is a great pleasure to thank those who made this dissertation possible. First and foremost, I would like to show my gratitude to my advisor, Prof. L. Jay Guo, who has supported me throughout Ph.D. study with his patience, encouragement, and guidance. Without his supports, this dissertation would not have been possible, and I cannot thank him enough for what he has done for me in the past several years. I am also highly thankful to my committee members, Prof. Theodore B. Norris, Prof. Herbert Graves Winful, Prof. Xueding Wang, and Dr. John A. Nees, for their valuable suggestions throughout this study.

I would like to acknowledge all current and past Guo Research Group members, Dr. Se Hyun Ahn, Dr. Chung-Yen Chao, Dr. Yi-Hao Chen, Dr. Li-Jing Cheng, Dr. Philip Choi, Dr. Moon Kyu Kwak, Prof. Dawen Li, Dr. Myung-Gyu Kim, Dr. Carlos Pinar, Prof. Haofei Shi, Dr. Ting Xu, Dr. Hyoung Won Baac, Alex Kaplan, Hyunsoo Kim, JaeYong Lee, Kyu-Tae Lee, Dr. Tao Ling, Xiaodong Liu, Brandon Lucas, Jong G. Ok, Ashwin Panday, Dr. Hui Joon Park, Xin Tu, Yi-Kuei Wu, Cheng Zhang, Peng Zhu, for their kindness and help for my study. I would also like to acknowledge the staff and student members of Lurie Nanofabrication Facility and Solid-State Electronics Laboratory for their kind help during my study. It was a great luck for me to work with wonderful

facility and people. My special thanks go to Dr. Sheng-Wen Huang, Dr. Tao Ling, Dr. Zhixing Xie, You-Chia Chang, Kuang-Wei Lin, and Dr. Tzu-Yin Wang for their help in theoretical and experimental works for my dissertation.

Lastly, I offer my regards and blessings to all of those who supported me in any respect during the completion of Ph.D. study.

Table of Contents

List of Figures

List of Tables

Abstract

This work is to utilize the superior characteristics of polymer microring resonators in ultrasound detection to push the application of photoacoustic imaging to an entirely new level.

We first demonstrated significantly improved imaging quality for photoacoustic tomography (PAT) using microring detectors. For wideband PAT, the microring detectors were able to faithfully detect both the boundaries and the inner structure, while piezoelectric detectors can only preserve one of the two aspects. For high-resolution PAT over a large imaging area, we imaged 50 μm black beads and found that microrings produced high-resolution imaging over a 16-mm-diameter imaging area while the 500 μm piezoelectric detectors only obtained high-resolution imaging over a small area around center.

Pure optical photoacoustic microscopy (PAM) has been demonstrated. Microring ultrasonic resonators were applied in *in vivo* photoacoustic imaging for the first time. Good imaging signal-to-noise ratio and high axial resolution of 8 μm were calibrated. As a comparison, a commercial hydrophone with similar sensitivity produced a low axial resolution of 105 μm.

A 5 mm miniaturized probe consisting of a fiber to deliver excitation laser pulses and microring detectors for ultrasound detection has been fabricated for photoacoustic endoscopy. The calibrated high radial resolution of 21 μm was higher than other types of endoscopic photoacoustic probes, around 40 μm or larger.

A photoacoustic correlation spectroscopy (PACS) technique was proposed. In a proof-of-concept experiment, we demonstrated low-speed flow measurement of ~15 μm/s by the PACS technique. We also demonstrated *in vivo* flow speed measurement of red blood cells in capillaries in a chick embryo model by PACS. Other techniques might have difficulties to measure it due to the low signal contrast and/or poor resolutions.

We also proposed terahertz electromagnetic pulse detection by photoacoustic method. We used carbon nanotube composites as efficient photoacoustic transmitters and microrings as sensitive detectors. The photoacoustic method provides low-cost and real-time terahertz detection (~μs), which is difficult by conventional terahertz detectors, such as a bolometer or a pyroelectric detector.

Chapter 1 Introduction

1.1 Motivation

Medical diagnosis and therapy are greatly benefited by the advances of medical imaging techniques, such as photoacoustic imaging, ultrasound imaging, optical imaging, and magnetic resonance imaging (MRI). Each imaging modality has its advantages and disadvantages, and can be used for some specific diseases. Photoacoustic imaging detects optical absorption within biological tissues and provides valuable physiological properties, such as hemoglobin concentration and oxygen saturation. As a result, the promising imaging modality has been rigorously investigated over the past decade [1-3].

High-frequency photoacoustic imaging enables better image resolution, potentially moving photoacoustic imaging toward various clinical applications. In photoacoustic imaging, a detector or detector array is required for the detection of photoacoustic waves. Despite the type of detectors, the imaging quality, quantified by spatial resolution and signal-to-noise ratio (SNR) at a certain depth, are greatly influenced by the size, sensitivity, angular response, and frequency response of a single detector or array of detector elements. Currently, the fabrication of a detector or array elements with small device size, high sensitivity, wideband frequency response, and wide acceptance angle is still challenging, restricting the development of high-frequency

photoacoustic imaging.

Based on the detection mechanism, the detectors can be categorized into three types. The first is piezoelectric transducers. Currently, these are the most commonly used for photoacoustic imaging because piezoelectric technology is well developed for medical ultrasonic imaging. The second is capacitive micromachined ultrasound transducers (CMUTs), a type of device studied since the 1990s. However, the above two technologies still have difficulties in the fabrication of suitable detectors for high-quality photoacoustic imaging. Recently, a third detection mechanism, resonant optical detection, has been investigated and has the potential to ward off the technical issues of piezoelectric and CMUT detectors. Resonant optical devices include microrings, etalons, fiber gratings, and Bragg grating waveguides. The first has been rigorously studied in our lab. This thesis presents the advantages of microring ultrasonic detectors, and then demonstrates various applications to photoacoustic imaging.

1.2 Ultrasonic detectors

Piezoelectric effect was discovered in 1880 and started to be used for various applications since the 1950s. Currently, piezoelectric sensors are increasingly used in medical instruments and can be regarded as a mature technology with excellent inherent reliability. They are able to convert pressure to an electrical signal by the piezoelectric effect, providing an acoustic detection mechanism. However, several disadvantages limit their application in photoacoustics. First, the sensitivity of piezoelectric transducers depends on the element size. High-frequency flat transducers usually have an element

size larger than 1 mm to maintain reasonable sensitivity. Although an electronic scan system can be attached to form a synthetic aperture for beam-forming applications, the large element size and narrow acceptance angle greatly restrict the aperture size for high-frequency beams, resulting in very poor resolution. Second, high-frequency focused transducers usually have very low f-numbers, severely obstructing the depth of the field. Third, to develop arrays for real-time imaging, besides the sensitivity issue, piezoelectric technology suffers from challenging fabrication and complex electrical interconnects. Piezoelectric sensors are certainly not desirable detectors for high-resolution, μm to tens of μm, clinical imaging applications.

Advances in fabrication technology have promoted the development of high-performance CMUTs [4-8]. A CMUT is composed of a capacitor cell a metalized membrane as a top electrode and a doped silicon substrate as a bottom electrode. The working principle is that the acoustic stress modulates the capacitor spacing, producing an electronic signal. CMUTs provide some advantages over piezoelectric transducers. CMUTs generally have a wider bandwidth than piezoelectric sensors and, thus, offer better axial resolution, making them favorable for the imaging of smaller objects [9-10]. For array fabrication, CMUTs use the advanced micromachining techniques used for integrated circuits, acquiring the advantages of flexible design, low cost, smaller size, and unique wafer design of front-end electronics [11-13]. However, the transduction efficiency currently is lower than that of piezoelectric transducers. The low sensitivity of CMUTs limits their application where high propagation depth of is required. For high-frequency photoacoustic tomography, small size detectors are desired, as detailed in Chapter 3. Small sized elements of CMUTs decreased the SNR further [14].

Reliability is another important issue which needs to be addressed. Moreover, the acoustic crosstalk in CMUT arrays has not been solved, and remains an ongoing research topic [15]. Although CMUT technology shows promise in some aspects, there are some major challenges left to overcome before high-frequency high-sensitivity CMUTs can be fabricated and used in practical photoacoustic imaging applications.

As a result of the advances in optics, telecommunications, and micro and nano fabrication techniques, resonant optical detection has emerged as a promising alternative to piezoelectric transducers and CMUT. In resonant optical detection of ultrasound, the interaction of an optical field with ultrasound waves is utilized. Acoustic pressure modulates the probing optical field within a resonant cavity. With a sharp cavity resonance, the optical response is amplified, giving high sensitivity to ultrasonic detection. Devices based on this technique, including microrings [16-24], etalons [25-39], fiber gratings [40], dielectric multilayer interference filters [41], and Bragg grating waveguides [42], have been studied.

Microrings are one of the most promising and simplest approaches. A microring resonator device is composed of a straight waveguide coupled with a ring waveguide, where the microring serves as an optical resonator. It can be shown that when the optical resonance condition is satisfied, the total field of the optical wave returning to the coupling section from the ring waveguide coupler is π out of phase with the optical wave propagating through the coupler region in the straight waveguide, resulting in destructive interference. Thus, the transmission spectrum of the device will have resonance dips.

Based on our current understanding, the principle for the detection of ultrasound

signal is that the acoustic pressure deforms the polymer waveguide and changes the effective index of the propagating mode. Additionally, there is an elastooptic effect that contributes to the effective index change. In microring ultrasonic sensors, detections can be made by measuring the output intensity changes from the device at a fixed wavelength. The scheme is useful for detecting very small change in the effective index, creating a mechanism for sensitive ultrasound detection. Other than being used as sensitive ultrasonic sensors, microrings with broad bandwidth in excess of 90 MHz will significantly expand the frontiers of high-frequency ultrasound and photoacoustic imaging. Microring arrays have also been investigated and demonstrated [17-18]. One of the most significant advantages of microring detectors over piezoelectric ones is that small size and spacing of each array element can be easily achieved by the micro and nano fabrication techniques. Small element size and spacing make it suitable for synthetic aperture imaging at frequencies over 100 MHz. Also, the wavelength division multiplexing concepts can be utilized to enable array operation [17]. Additionally, cross-coupling of light occurs only when array element spacing is on the order of the optical wavelength, avoiding some troublesome crosstalk issues encountered when using piezoelectric and CMUT techniques. Another exciting advantage of microring resonators is the potential for miniaturization, which enables a catheter-type sensor to fit into small volumes.

1.3 Photoacoustic imaging

Advances in biomedical imaging have drastically improved the detection and

staging of cancer. However, current technologies mostly concentrate on the diagnosis of clinically obvious cancers. The ability to detect cancers at early stages [43-45] is strongly desired in the development of every biomedical imaging modality. Most imaging techniques, such as X-ray computerized tomography [46-47], ultrasound [48-49], and MRI [50], are limited in their ability to detect small tumors with high specificity. In most cases, the detectable lesions have grown to at least 1 cm in diameter. In other words, these techniques significantly reduce the probability of successful therapy since the tumors often cannot be identified before reaching the lethal range. Consequently, it is imperative to develop new, non-invasive modalities for early detection of cancers, requiring both high contrast and high resolution, preferably in real time.

Because the optical properties of biological tissue are intrinsically sensitive to tissue abnormalities and functions, optical imaging can provide sensitive contrast information in biological tissue, which potentially enables early detection of cancers. Optical absorption properties can be used to quantify angiogenesis. They can also be used to deduce certain physiological parameters such as the oxygen saturation of hemoglobin, an important diagnostic parameter of cancers, and the concentration of hemoglobin. However, strong light scattering in tissues restrict the imaging depth less than 1 mm, as in optical coherence tomography [51-53], or cause the poor imaging resolution, as in diffusive optical tomography [54-56]. On the contrary, ultrasound scattering is much weaker and thus yields good resolution at sufficient depth, but pure ultrasound imaging suffers from low contrast [57]. To meet all the requirements of high-quality imaging, combinations of optical and ultrasonic technologies have been explored,

which merges the contrast advantages of optical imaging with the resolution advantages of ultrasound imaging. Photoacoustic imaging represents such a hybrid technology [58-71].

Photoacoustic imaging is based on the photoacoustic effects, which means the generation of acoustic waves by the absorption of electromagnetic energy. Alexander Graham Bell first reported the observation of sound generated by light in1880. Typically, a pulsed laser is used for biomedical imaging applications. When the laser energy is absorbed by the imaging target, a small temperature rise causes thermal expansion by the thermoelastic mechanism and generates acoustic waves. Induced acoustic waves range widely in the frequency spectrum and are measured by ultrasonic detectors placed around the sample in a pre-determined geometry. Then, recorded photoacoustic signals are used for imaging reconstruction. The imaging contrast is provided by the optical properties of biological tissues, including absorption coefficients, heat capacity, and thermal expansion coefficients. The resolution is at multiple length scales decided by the frequency of the ultrasound waves. In the last decade, photoacoustic imaging is the fastest-growing area of biomedical imaging technology. This can be evidenced by the fast-growing publications in the field of photoacoustics these years. It has been successfully studied in breast cancer detection [58-59], small animal imaging [60, 63], functional imaging [65-66], intravascular imaging [68-69, 71], and eye imaging [70].

The two principle components in a photoacoustic imaging system are a pulsed laser and an ultrasonic detector. For the former, the wavelength should be properly chosen to optimize both optical penetration depth and optical absorption contrast

between cancerous and normal tissues. The pulse duration is another factor for high-resolution imaging. For the cancer detection, a single detector with high sensitivity and very wideband response is imperative. For array detectors, elements with small size and spacing enable three-dimensional real-time high-resolution photoacoustic imaging, useful in clinical applications. Microrings have shown promising results and have potential to be one of the most suitable detectors in the photoacoustic systems.

1.4 Dissertation overview

Although microring resonators have been intensely investigated for a few decades and used in various applications, they have only been explored as ultrasonic detectors since 2004. Before use in practical photoacoustic imaging applications, the devices should be calibrated and tested in phantom experiments. This thesis describes the benefits of microring ultrasonic detectors, and focuses on the applications of photoacoustic imaging in various schemes.

Chapter 1 provides a brief introduction and motivation. Three ultrasonic detectors are compared. The requirement to achieve photoacoustic imaging with high resolution, μm to tens of μm, at large imaging depths, several mm to 1 cm, are described.

Chapter 2 presents the polymer microring resonators, including the underlying principles and device preparation. The optical resonance, frequency response of over 90 MHz at –3 dB, noise-equivalent pressure of 21.4 Pa over 1 to 75 MHz, and angular response of microring resonators, +/− 40° at –6 dB for a 20 MHz acoustic signal, are

characterized. Applications to delay-and-sum beam-forming photoacoustic imaging using a synthetic aperture are demonstrated.

Chapter 3 describes the significantly improved imaging quality of photoacoustic tomography using microring detectors. First, wideband response of microrings can faithfully reconstruct the inner structure, corresponding to low ultrasonic frequencies, and boundaries, corresponding to high ultrasonic frequencies. Second, several small sizes of microring detectors with ultra-low noise are also tested, showing extremely promising imaging results, high resolution and high contrast over a large imaging area.

Chapter 4 details the application of microring resonators in photoacoustic microscopy. A preliminary test in an *in vivo* imaging of mouse ear and an *ex vivo* imaging of mouse bladder is used to show the potential of microring resonators in clinical applications. Design of photoacoustic microscopy based on the coaxial scheme and reflection mode using microrings on a transparent substrate for convenient animal studies is also presented.

Chapter 5 shows that the polymer microring resonators have the potential to be applied to endoscopic photoacoustic imaging. A miniaturized photoacoustic catheter, including light source and microring detector, has been fabricated and calibrated. The results show that we can achieve a small probe size of 5 mm in diameter and a high radial resolution of 21 μm. Further improvement to prepare the catheter for clinical applications will be discussed.

Chapter 6 introduces a new application of photoacoustic effects, photoacoustic correlation spectroscopy (PACS), which is inspired by fluorescence correlation spectroscopy. Current blood velocimeters such as laser Doppler velocimetry and

optical/ultrasound particle image velocimetry have limited sensitivity and resolution, restricting their applications to measure blood flow speed in capillaries. We proposed the PACS technique to measure it. The principles of PACS will be given. A phantom experiment will be performed as a proof-of-concept experiment. In the experiment, low-speed flow measurement, ~15 μm/s, was demonstrated. *In vivo* blood flow speed measurement in the capillaries in a chick embryo model is also demonstrated.

Chapter 7 described an interesting application of photoacoustic detection using microring resonators. We proposed a terahertz (THz) electromagnetic pulse detector consisting of an efficient photoacoustic transmitter, a composite of carbon nanotube and polymer, and an optical microring resonator as a sensitive photoacoustic sensor. Calibration of the photoacoustic-based THz detector will be presented. We showed the real-time detection, which is difficult by current THz detectors such as a bolomter or a pyroelectric detector.

Chapter 8 summarizes all work, highlights main contributions of each work, and discusses the future experiments to be conducted.

Chapter 2 Microring ultrasonic sensors

2.1 Principles of microring ultrasonic sensors

A microring resonator device, shown in Figure 2.1 (a), is composed of a straight waveguide, also called bus waveguide, coupled with a ring waveguide, where the microring serves as an optical resonator. Resonance occurs when the round-trip phase change of an optical wave propagating in the ring waveguide equals to $2m\pi$, where m is an integer. When the cross-coupled intensity (the coupling ratio from the straight waveguide to the ring waveguide) is balanced by the total loss inside the resonator, this condition is called critical coupling. If the cross-coupled intensity exceeds the total loss inside the resonator, the resonator lies in the regime of over coupling. By contrast, if the total loss inside the resonator exceeds the cross-coupled intensity, it lies in the regime of under-coupling. A steady effect of cross-coupled intensity and the loss inside the resonator results in the resonance dips in the transmission spectrum, as shown in Figure 2.1 (b). The contrast, defined as the ratio of on-resonance intensity to off-resonance intensity, degrades when the coupling condition is away from the critical coupling. From the definition of the Q factor (the ratio of the total stored energy of a resonator to the loss energy per cycle), the Q factor of a resonator increases as loss decreases.

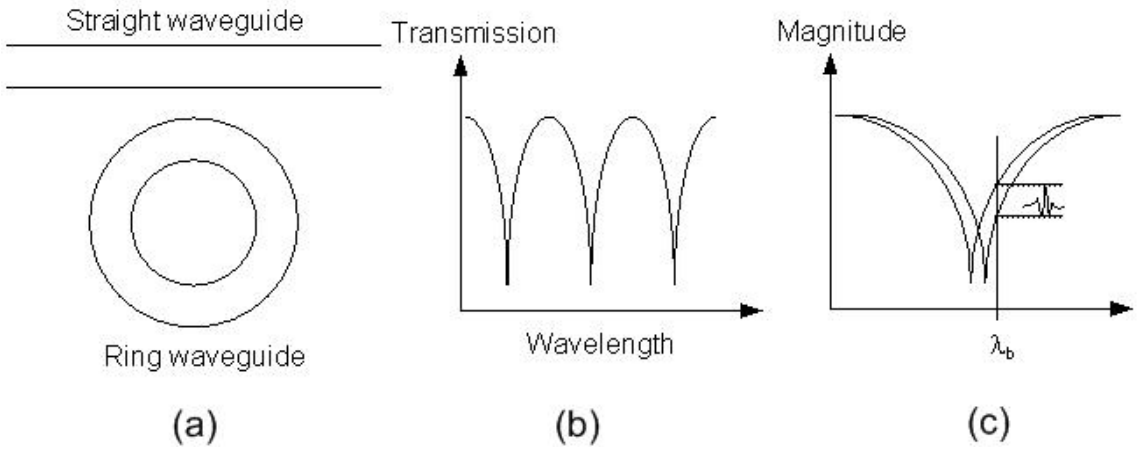

Figure 2.1 Schematic of (a) a microring resonator; (b) its resonance spectrum; and (c) ultrasound detection using the optical resonance of a microring sensor: ultrasound pressure pulse causes dynamic shift of resonance wavelength, producing a modulated intensity in the form of a pulse in the light output.

As an ultrasonic sensor, polymer microring resonators experience a strain field, caused by incident acoustic waves, which slightly deform the waveguide shape. The change in waveguide cross section directly modifies the effective refraction index of the guided mode. Moreover, the strain will also alter the refractive indices of the waveguide material and its surroundings, usually water, via the elasto-optic effect. Hence, the resonance condition is modulated. Detailed theoretical calculation can be found in [17]. Ultrasound detection is illustrated in Figure 2.1 (c). When the device is probed at a fixed wavelength with a high slope in the transmission spectrum, the output intensity can be modulated by the ultrasound wave, which is then recorded by a high-speed photodetector. Accordingly, high sensitivity detection requires high Q resonators.

2.2 Device preparation

A nanoimprint technique [72] was used to fabricate the polymer microring device due to its simplicity, high fidelity, and precise dimension control. Detailed fabrication processes of polystyrene (PS) microring resonators have been described previously [73]. The substrate was ~3 μm SiO_2 on a 0.5-mm-thick Si. The channel waveguide was fabricated. In the following work, the cross section of waveguides was designed as 2 μm × 2 μm for single mode operation at an optical wavelength of 1550 nm; while it was 1.4 μm × 1 μm (height by width) for single mode operation at an optical wavelength of ~780 nm. The schematic of cross-section view of the PS waveguide is shown in Figure 2.2. The developed microrings have a diameter of 100, 90, 60, and 40 μm and will be used to show the different applications. The gap in the coupling region between the microring and straight waveguides is several hundred nanometers. For easy ultrasound measurement, fibers were butt-coupled to the straight waveguide and glued at the cleaved edges of the silicon substrate using UV curable epoxy. The schematic of fiber-glued

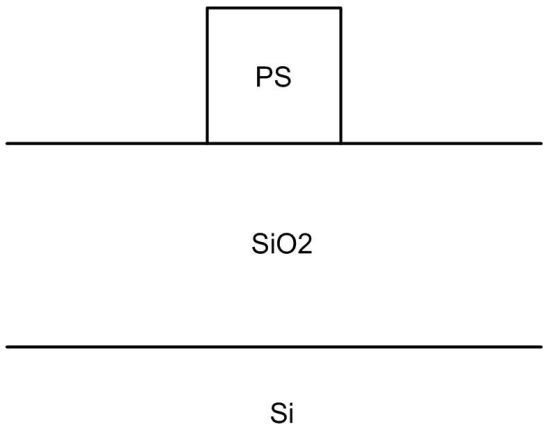

Figure 2.2 Schematic of cross-section view of the PS waveguide.

microring device was shown in the lower part of Figure 2.3. To achieve high sensitivity ultrasound detection, the light intensity coupled into the polymer waveguides should be maximized. Thus, a single-mode fiber was used as an input fiber to provide better mode matching. The output light was collected by a multimode fiber with a core diameter of 62.5 μm. Note that in the photoacoustic tomography discussed in Chapter 3, the sensor chip was rotated around the object and therefore polarization maintaining fibers were used to avoid changes to the power coupled into the waveguide at a specific polarization, which might alter the slope in the transmission spectrum and cause change of sensitivity to ultrasound at different sensor positions.

2.3 Devices calibration

2.3.1 Sensitivity

The setup shown in Figure 2.3 was used to measure the noise-equivalent pressure (NEP) and the sensitivity of microring devices. A continuous-wave tunable laser source was connected to the device's input fiber, and the output fiber was connected to a photodetector (1801-FC and 1811-FC, New Focus, San Jose, CA) with an electrical bandwidth of 25 kHz–125 MHz. The photodetector was coupled output to a digital oscilloscope for data collection.

Table 2.1 shows the specifications of the devices we have developed [19, 22, 24]. The first generation device, MR-100 (MR: microring, 100: device size), was calibrated. Using the dc output from the photodetector, we measured the device's transmission spectrum, shown in Figure 2.4(a), with an input power of 4.2 mW. The Q factor was

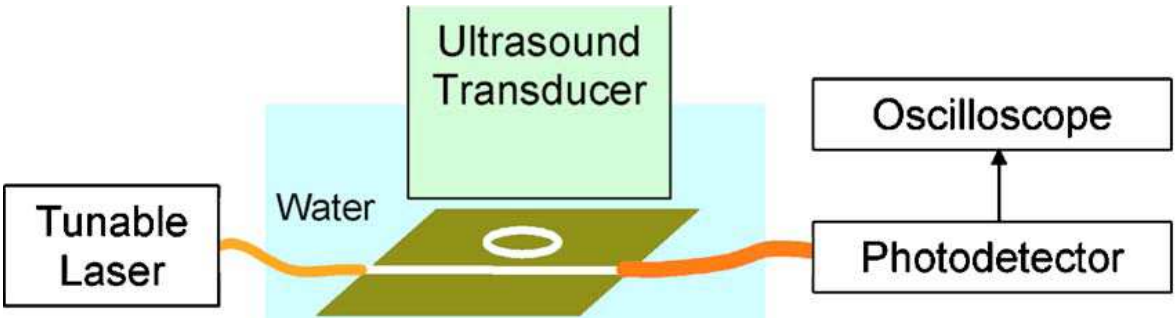

Figure 2.3 Experimental setup to measure the NEP and the sensitivity of a polymer microring resonator. The distance between the ultrasound transducer and the resonator was 1.5 mm.

estimated to be 6000. The off-resonance light transmission shows that around 9% of the probing light was collected by the photodetector mainly due to mode mismatch at the fiber-waveguide coupling region. The transmission ratio can be improved with better device preparation. For example, tapered shape can be designed at the straight waveguide to have larger cross section at the side close to input fiber, reducing mode mismatch between the input fiber and the straight waveguide.

A 20 MHz unfocused transducer (V316, Panametrics NDT, Waltham, MA) with a

	Operating wavelength	Device diameter	Q factor	Sensitivity (mV/kPa)	NEP @ 1-75 MHz	Reference
MR-100	1550 nm	100 μm	6000	11	230 Pa	[19]
MR-90	1550 nm	90 μm	20000	36.3	88 Pa	[22]
MR-6040	780 nm	60 μm (and 40 μm)	400000	66.7	21.4 Pa	[24]

Table 2.1 Developed microrings with calibrated Q factors, sensitivity, and NEPs.

3.18 mm diameter was used to insonify the microring. It launches a peak pressure of 30 kPa around its surface, calibrated using a hydrophone [18], when driven by a 10 V peak-to-peak one-cycle 20 MHz sinusoidal wave. The acoustic coupling medium was de-ionized water. The optical probing wavelength and input power were set to 1555.51 nm and 5.5 mW, respectively. Ultrasound signals were detected by the ac output of the photodetector.

Figure 2.4(b) shows a recorded signal trace and Figure 2.4(c) shows the spectra of the signal and an acoustic waveform measured by the hydrophone. The ringing waveform

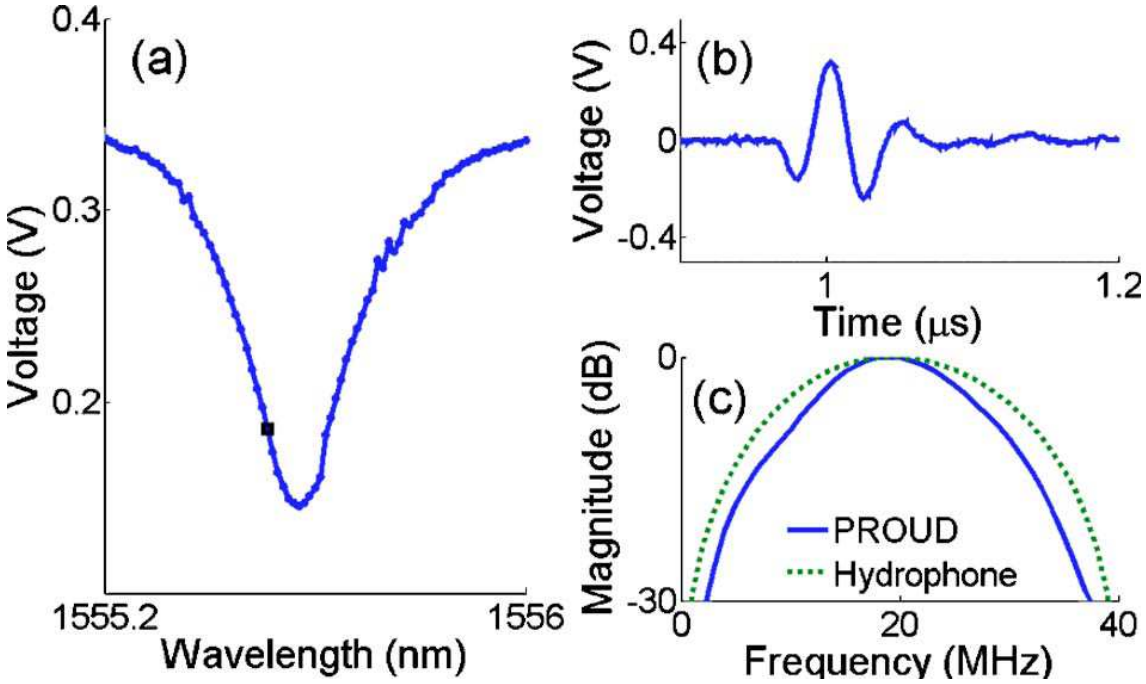

Figure 2.4 (a) Optical transmission spectrum of polymer microring resonator (MR-100). The input power was 4.2 mW. The resonance wavelength and the bandwidth were 1555.57 nm and 0.24 nm, respectively. (b) Single-shot acoustic waveform measured by the resonator. The positive peak corresponds to 30 kPa. The optical probing wavelength and input power were set to 1555.51 nm [indicated with a square in (a)] and 5.5 mW, respectively. (c) Spectra of acoustic waveforms measured by the resonator and a hydrophone.

following the main pulse signal was due to reflections within the silicon substrate, which can be removed by changing substrate materials and/or structures. Since a 30 kPa acoustic pressure produced an output voltage of 332 mV, the sensitivity of the microring device was 11 mV/kPa. The root-mean-square noise levels were 1.5, 2.2, and 2.5 mV over 1 to 25, 1 to 50, and 1 to 75 MHz bandwidths, respectively, and the corresponding NEPs, a measure of the minimum detectable pressure of the device, were 0.14, 0.20, and 0.23 kPa [=(2.5 mV)/11 mV/kPa)] by extrapolating the sensitivity to other frequencies, 1 to 75 MHz. Since the frequency response of the device was over 90 MHz at −3 dB, which will be described below, it is valid to do the extrapolation of sensitivity from 20MHz to other frequencies below 90 MHz. Compared to the previous best result, 4.1 kPa over 5–75 MHz [18], we have improved NEP by more than one order of magnitude. The same level of NEP was achieved using a Fabry–Pérot etalon with a detection bandwidth of 20 MHz and a detector diameter of 50 μm [74]. The tested microring device is 20 times more sensitive than a 75 μm piezoelectric polyvinylidene fluoride (PVDF) transducer (HPM075/1, Precision Acoustics, Dorchester, Dorset, UK; http:// www.acoustics.co.uk/products/hpm075-1), which has an NEP lower bound of 6 kPa [=(60 μV)/(10 nV/Pa)] over a 100 MHz bandwidth considering only the noise from its matched preamplifier (HP1, Precision Acoustics). In addition, microring's NEP can be further reduced by coupling more detection light into a device or by increasing its *Q* factor. Following the calibration similar to that used for MR-100, the Q factors and NEPs of MR-90 and MR-6040 were obtained.

2.3.2 Frequency response

A wideband optoacoustic source was utilized to measure the detection bandwidth of a microring device. The MR-100 was used in this calibration. A 100 nm thick chromium film was deposited onto a glass substrate. Illuminating such a film with a wide-spot nanosecond laser pulse generates a planar acoustic wave with a temporal profile duplicating that of the excitation laser pulse shape [75-76]. The chromium film was placed 540 μm above a microring device and was illuminated by a 532 nm pulsed frequency-doubled Nd-YAG (yttrium aluminum garnet) laser (Surelite I-20, Continuum, Santa Clara, CA) with a spot size of 4.5 mm in diameter. The acoustic coupling medium was de-ionized water. An acoustic pulse signal detected by the microring device and a laser pulse temporal profile detected directly by the same photodetector are shown in Figure 2.5(a). Figure 2.5(b) presents corresponding spectra together with the estimated

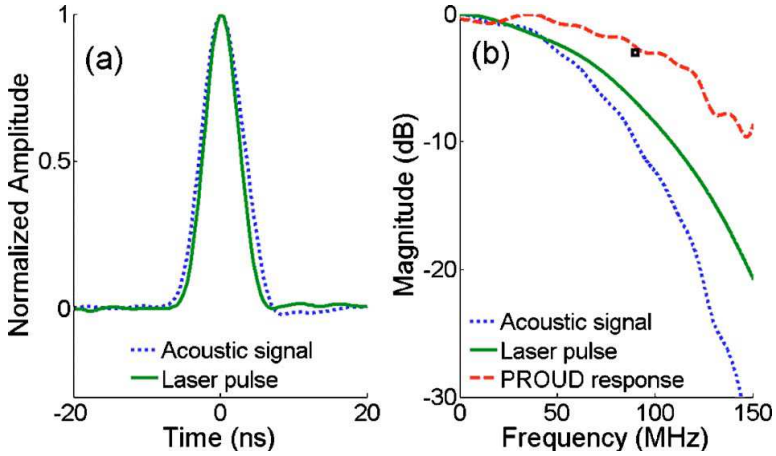

Figure 2.5 (a) Acoustic signal detected by a polymer microring resonator and laser pulse profile detected by the photodetector. (b) Spectra of the signals and frequency response of the resonator. A square indicating (90 MHz, −3 dB) is shown as a reference. The detection bandwidth of the resonator is over 90 MHz at −3 dB.

frequency response of the device, obtained by taking the difference of the two spectra and compensating for acoustic attenuation in water assuming an attenuation coefficient of 2.2 $\times 10^{-4}$ dB/mm MHz^2 [77]. The detection bandwidth of the microring device was over 90 MHz at −3 dB. As a reference, limited by equipment, we could only confirm a detection bandwidth of 55 MHz previously [17]. To be able to measure a detection bandwidth of hundreds of megahertz, a wider band photodetector and a more uniform and wideband planar wave are required. More detailed analysis of the limitation of frequency response will be discussed in Chapter 4.

2.3.3 Angular response

A photoacoustic method was used to test the angular dependence of sensitivity for the microring (see Figure 2.6). The MR-100 was firstly calibrated. A 49-μm diameter black polystyrene (PS) microsphere (BK050, Microgenics Corp., Fremont, CA) was set in a gel created by mixing 1.5% agarose (GPG/LE, American Bioanalytical, Natick, MA) with water. The microsphere was placed very close to the surface of the gel to minimize acoustic absorption. A 532 nm pulsed frequency-doubled Nd-YAG laser (Surelite I-20, Continuum, Santa Clara, CA) was used to illuminate the microsphere. The bead's optical absorption at this wavelength causes transient heating and expansion of the sphere, and subsequently, generation of a spherical acoustic pulse.

The angular sensitivity for the microring is shown in Figure 2.7 for frequencies of 10, 15, and 20 MHz signals. Signal levels at these frequencies were extracted by applying bandpass filters centered at the corresponding frequencies to the recorded acoustic pulses,

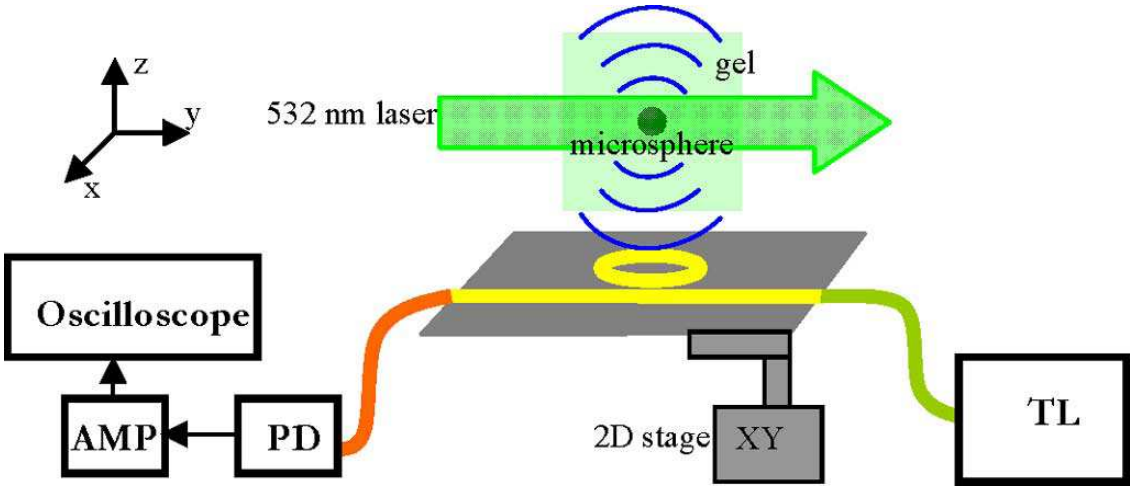

Figure 2.6 Experimental apparatus (similar to Fig. 2.2) for measuring angular sensitivity of the microring resonator and imaging of a 49 μm microsphere. The PS microsphere produces a spherical wave, and the microring is scanned tangentially to the wave. The gel bulk and the microring were submerged in deionized water.

and then, detecting the peaks. The angular sensitivity shows frequency-dependant behavior. Such a frequency-dependent behavior can be understood by considering a ring piston transducer, where the theoretical angular response or directivity D, is given by [78] $D(\theta) = J_0(ka \sin(\theta))$, where J_0 is the Bessel function of the first kind, $k = \omega_a / c$ is the

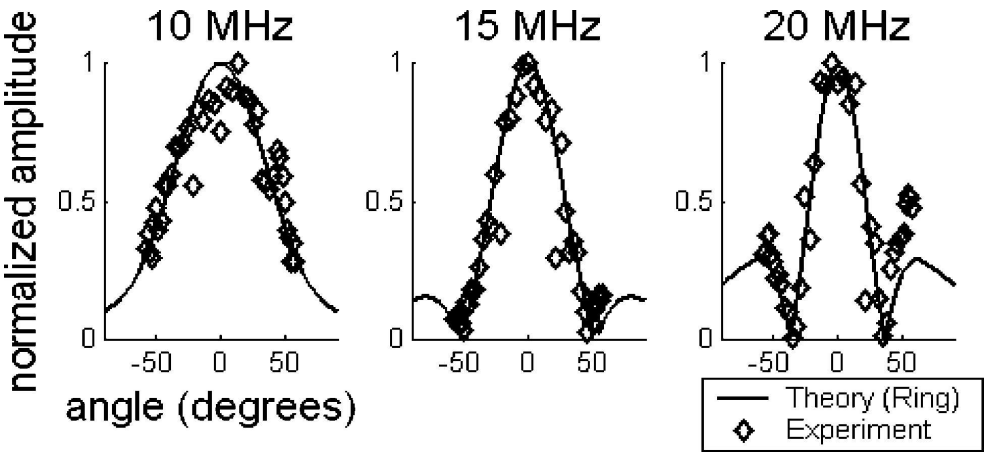

Figure 2.7 Calculated and measured angular sensitivity of the MR-100 at frequencies of 10, 15, and 20 MHz. Experimental results agree well with the theoretical curves.

wavenumber of the incident acoustic signal, a the average radius of the element, and θ the incident angle of the acoustic wave. The theoretical curve is also shown in Figure 2.7, which fits well with the experimental data. For a given k, an element will generally have a wider angular sensitivity when the ring radius is reduced. One method of characterizing the angular response is to measure the −6 dB beamwidth, or full-width at half maximum (FWHM). For beam-forming applications, the beamwidth of the main lobe should extend to +/− 40◦ incidence. For a 20 MHz bandwidth, the element diameter must be less than 50 μm, and for 50 MHz bandwidth, must be smaller than 25 μm in order to comply with these requirements. Following calibration similar to that used for MR-100, the angular response of MR-6040 was obtained, as shown in Figure 2.8.

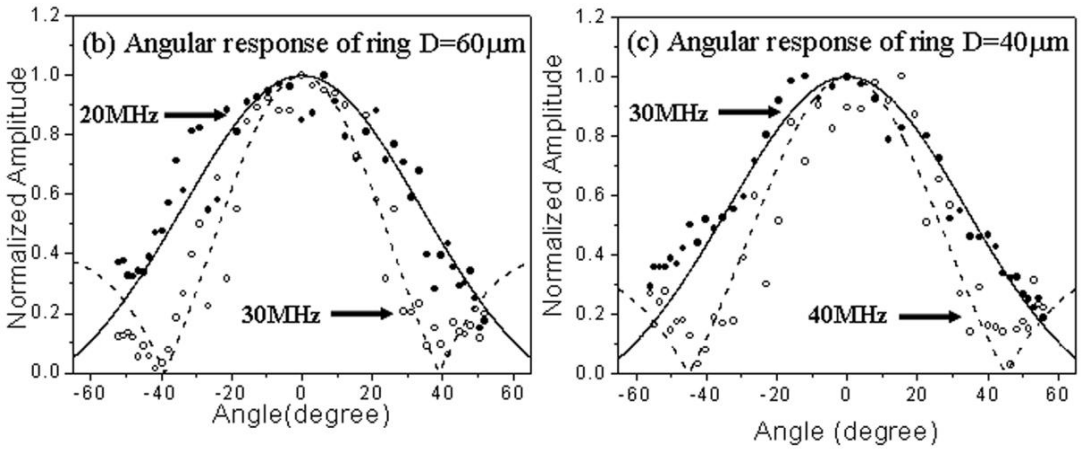

Figure 2.8 Eexperimental data (dot) and theoretical calculation (line) of angular response of the polymer microrings with (b) D = 60 μm at 20 MHz (solid dot and line) and 30 MHz (empty dot and dash line), and with (c) D = 40 μm at 30 MHz (solid dot and line) and 40 MHz (empty dot and dash line).

2.4 Applications to high-sensitivity beam-forming imaging

2.4.1 Beam-forming experiments

We use photoacoustic imaging to quantitatively explore the potential of low NEP of polymer microring resonators. Microirng MR-100 was used here. The experimental setup used to test the microring device for three-dimensional (3-D) photoacoustic imaging is shown in Figure 2.9. A 49-μm diameter black PS bead was first fixed in a gel made by mixing water and 1% agarose (GPG/LE, American Bioanalytical, Natick, MA). Then the phantom was placed in deionized water. A 532 nm pulsed laser (Surelite I-20 with ~ 6 ns pulse width, Continuum, Santa Clara, CA) was used to illuminate the bead.

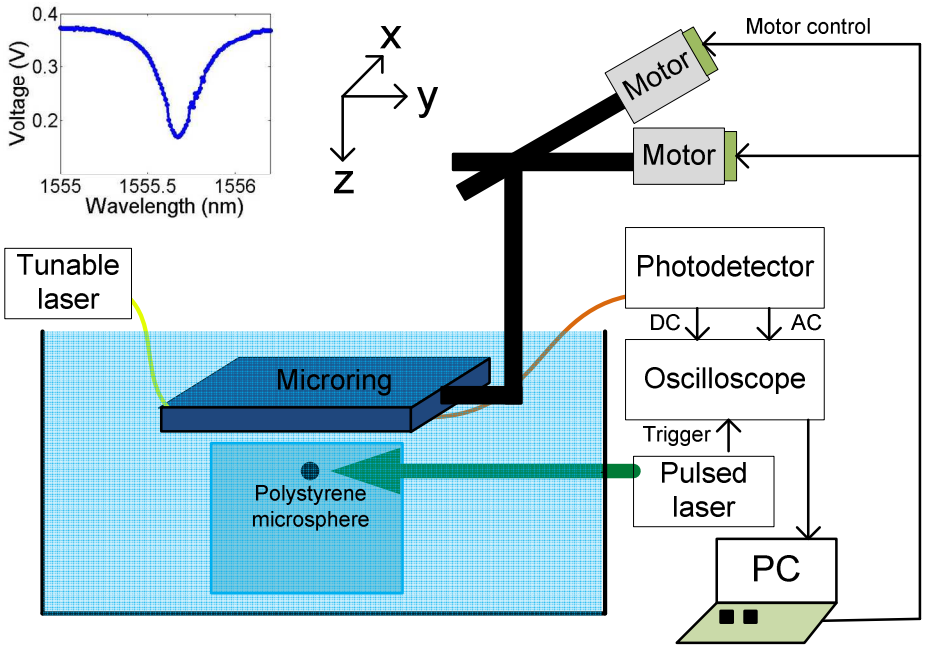

Figure 2.9 Experimental setup for 3-D photoacoustic imaging. A 2-D translation stage scanned a microring device to form a synthetic 2-D array. A bead placed in a gel block was imaged. The gel and the microring device were submerged in deionized water. Inset: transmission spectrum of the microring MR-100 at an input power of 4.2 mW.

The 4.5 mm beam width was delivered to the phantom width was ~ 4.5 mm without any focusing. A synthetic disk-shaped two-dimensional (2-D) array was formed by scanning the device using a 2-D translation stage.

First, we measured the transmission spectrum of the microring device. The measured transmission spectrum at a laser input power of 4.2 mW was shown in the inset of Figure 2.9. From the spectrum, the probing wavelength was chosen at 1555.6 nm to maximize the slope and thus the sensitivity. The 49-μm diameter black PS bead (BK050, Microgenics Corp., Fremont, CA) was illuminated at a laser fluence of 0.35 mJ/cm^2. The array had 249 elements with a step size of 0.1 mm in the x- and y-directions and a diameter of ~ 1.78 mm [= $\sqrt{249\times(4/\pi)}$ × 0.1]. Photoacoustic signals were detected at ~ 5 mm from the absorber by recording the AC output of the photodetector at different element positions. The probing light power was 5.5 mW, but due to the coupling loss the power coupled to the waveguide was about 435 μW. No signal averaging was applied in data collection and image reconstruction.

A bandpass filter with a center frequency of 28 MHz and a bandwidth of 16 MHz was applied to all element data and a delay-and-sum beam-forming algorithm with envelope detection was then used to reconstruct a 3-D image. The average noise level (root-mean-square value over a region where noise dominates) was –19.4 dB and –16.4 dB respectively relative to the image peak before and after the envelope detection. Figure 2.10 shows three 2-D cuts of the reconstructed images with a 15 dB dynamic range. The FWHM along the x (lateral), y (lateral), and z (axial) directions were 205, 260, and 100 μm, respectively. According to the array geometry and the filter, the ideal lateral and

axial resolutions are 209 and 81 μm, respectively. Therefore, the widths of the object image are reasonable for a 49 μm size bead. The lateral resolution can be improved using a larger array. Note that the bandpass filter used in the delay-and-sum beam-forming algorithm is usually not applied in photoacoustic tomography (presented in Chapter 3), which needs wideband signals to reconstruct images with a variety of spatial variation.

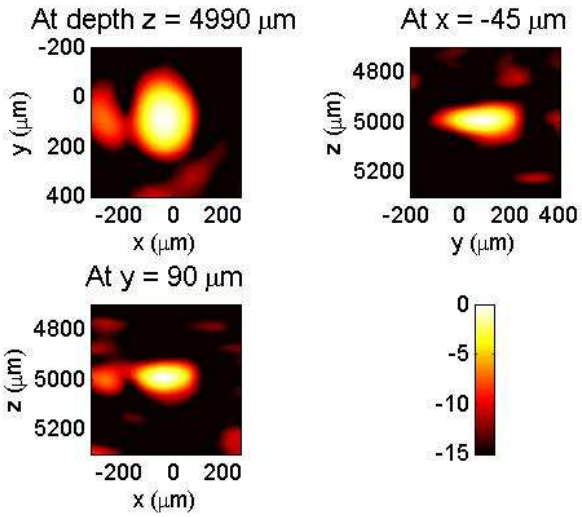

Figure 2.10 2-D cuts of 3-D photoacoustic images for a 49 μm diameter bead displayed with a 15 dB dynamic range. The average noise level was –16.4 dB relative to the image peak and no signal averaging was applied.

2.4.2 Quantitative analysis

The acoustic pressure P_{ac} generated by a spherical fluid object in an optically transparent fluid background that has the same sound speed and density as the object and measured at a distance r to the object center can be expressed as [38, 75]

$$P_{\mathbf{ac}}(t) = \frac{c^2 \beta W}{2C_p r} U(R - |r - ct|)(r - ct), \tag{2.1}$$

where R, β and C_p are the radius, thermal expansion coefficient and specific heat capacity of the object, W the absorbed energy density, c the sound speed, t the time, and $U(\xi) = 1$ for $\xi \geq 0$ and $U(\xi) = 0$ otherwise. We used this equation to estimate the expected peak pressure level to be 77.6 Pa in the imaging experiment presented in Section 2.4.1 with c = 2380 m/s [79], $\beta = 210 \times 10^{-6}$ K^{-1} [80] and C_p = 1.3 kJ/kg/K [81] for PS, R = 24.5 μm, r = 5 mm, and W = (0.35 mJ/cm^2) × πR^2 / ($4\pi R^3/3$) = 107 mJ/cm^3 assuming complete and uniform absorption in the bead. The NEP of microring devices was estimated by the applied peak pressure divided by the optical signal-to-noise ratio (SNR). The microring device has an NEP of 111.4 Pa over the passband of the aforementioned bandpass filter neglecting the effects of angular sensitivity, resulting in an effective NEP of 7.1 Pa [= (111.4 Pa) / $\sqrt{249}$] for the array used in this experiment. Thus, the estimated SNR is 20.8 dB [= (77.6 Pa) / (7.1 Pa) on linear scale], slightly higher than that in the actual imaging (19.4 dB). This small discrepancy might result from the overestimated signal levels because the sound speed of the background (1480 m/s in water) in the experiment is lower than that (2380 m/s) used in the estimation, and the finite duration of laser pulse and the water absorption (0.86 dB at 28 MHz for 5 mm propagation) are not considered.

In this work, we have demonstrated the benefits of low noise of polymer microring resonator in photoacoustic imaging. A 49 μm bead was imaged using a synthetic array with 249 elements with SNR of 16.4 dB at low laser fluence of 0.35 mJ/cm^2 and without signal averaging. As a comparison, if using a 75 μm piezoelectric

PVDF transducer, 20 times higher laser fluence would be required to achieve the same SNR [19-20]. Compared with MR-100, MR-6040 has much better sensitivity, which would give superior imaging depth.

2.5 Applications to wide-directivity beam-forming imaging

In this work, we conduct delay-and-sum beam-forming photoacoustic imaging to show the distinctive advantages provided by small microrings. 2-D and 3-D beam-forming PA imaging are presented. The setup is similar to that in Figure 2.9. Linear scan geometry was chosen because it emulates our ongoing work linear microring array work. The 100, 60, and 40 μm microrings were mounted on the motorized scanning stage to form a one-dimensional (1-D) and 2-D synthetic aperture, used for 2-D and 3-D imaging, respectively.

A 6-μm-diameter carbon fiber embedded in gel is used as a phantom to generate high-frequency photoacoustic signals. The carbon fiber is positioned parallel to the synthetic aperture of microrings at a distance of about 3 mm from the surface. The microring is scanned 5 mm in 100 μm steps parallel to the cross section of the carbon fiber. A bandpass filter spanning 20 to 60 MHz is applied to the recorded signal at each position. Then, a delay-and-sum beam-forming algorithm with envelope detection is used for 2-D image reconstruction. The application of the 20-60 MHz bandpass filter is chosen to fit the main band of photoacoustic signals generated from the 6 μm carbon fiber. The wave-field plot of the detected signals after the bandpass filter and the reconstructed image along the 1-D array is shown in Figure 2.11. Improved signal amplitudes at large

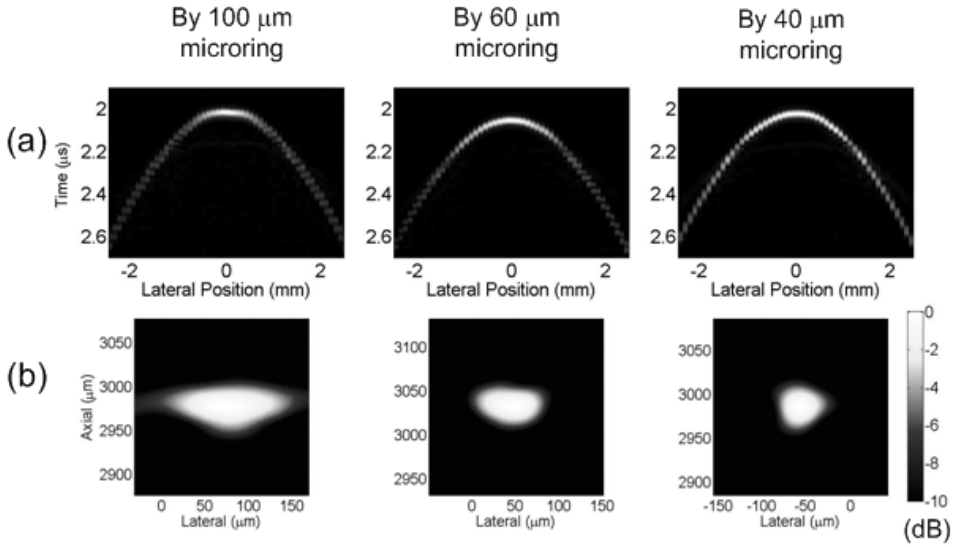

Figure 2.11 (a) Wave-field plot of the detected acoustic field along a 1-D array and (b) reconstructed image of the cross section of a 6-μm-diameter carbon fiber displayed over a10-dB dynamic range, where 0 dB represents the maximum reconstructed signal.

incident angles can be clearly seen in Figure 2.11(a) by reducing the microring size from 100 to 40 μm. The axial FWHM resolutions are similar, ~50 μm, for three sizes of microrings. This is because the same bandpass filter is used. The lateral resolution is 146, 77, and 55 μm for the case of 100, 60, and 40 μm microring, respectively. Improved lateral resolution was obtained because larger array aperture can be used in the smaller microring due to its larger acceptance angle. A filter with higher band can be used to improve the axial resolution at the expense of lateral resolution and SNR. The former is due to smaller aperture at higher frequency, and the latter is due to the mismatch between the band of photoacoustic signals and the filter. Thus, the specific bandpass filter can be chosen based on the consideration of trade-offs between resolutions and SNR. These results demonstrate that the 40 μm microrings are capable of forming detection arrays for photoacoustic imaging at resolutions of about 50 μm, representing one acoustic wavelength at a frequency of 30 MHz.

We also tested a 2-D synthetic array for 3-D photoacoustic imaging. The 50 μm PS beads fixed in a gel were imaged by 100 and 40 μm microrings. The center of the synthetic array, in the x-y plane, is defined as the origin of the coordinate system. The PS beads are placed about 3 mm above the array. The microring is scanned through a region of 5 mm by 5 mm. Bandpass filtering from 12 to 38 MHz was chosen to catch the main band of the photoacoustic signals. The reconstructed 3-D image and the 2-D cut image on the x-z plane crossing the center of the bead are shown in Figure 2.12. The lateral FWHM resolutions are ~150 and ~80 μm, respectively, imaged by the 100 and 40 μm microrings, while the axial resolution are similar, ~80 μm, by both microrings. The 3-D photoacoustic images clearly show the improved lateral resolution using 40 μm

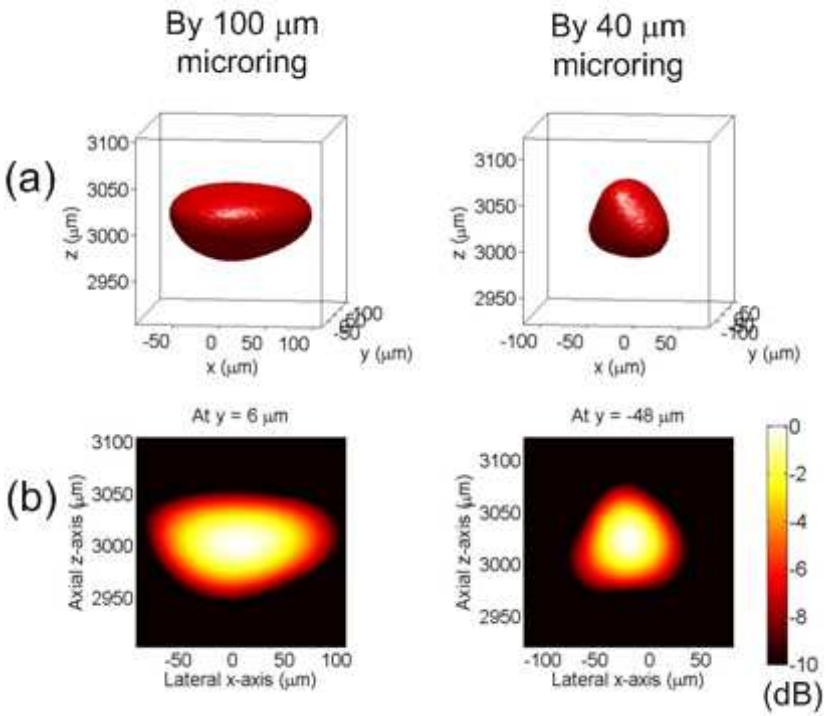

Figure 2.12 (a) –6 dB isosurface of a 3-D PA image of a 50 μm bead. (b) A 2-D image on the plane crossing the central position of the bead displayed over a 10 dB dynamic range.

microring. The wider angular acceptance characteristics of the 40 μm microring result in the improvement.

The small size microrings applied in beam-forming PA imaging demonstrated the improved lateral resolution because of a larger synthetic aperture of the microrings. Unlike piezoelectric transducers, the sensitivity of microrings is not directly related to its size. Thus, the microring has the potential to be fabricated in even smaller sizes without degrading the sensitivity with improvement in fabrication technologies.

Chapter 3 Photoacoustic tomography

3.1 Introduction

Photoacoustic tomography (PAT), also referred to as optoacoustic tomography, is the cross-sectional or three-dimensional imaging of an object using the photoacoustic effect. Optical energy deposition generates the photoacoustic pressure. As long as the photons are converted into heat, either scattered or unscattered photons can produce photoacoustic signals, allowing the photoacoustic tomography to work in the optically diffusive regime. The hybrid modality of optical imaging and ultrasound imaging combines rich optical contrast and high ultrasonic resolution. It has been applied in structural, functional [60, 82], and molecular imaging [83-84] *in vivo* in optically scattering biological tissue with high resolution at exceptional depths. Functional imaging can differentiate between live and dead tissue by measuring physiological functions such as blood flow and oxygenation. The concentrations of multiple chromophores of different colors (e.g., oxygenated and deoxygenated haemoglobin molecules in red blood cells) can be simultaneously quantified by using multiwavelength measurement. Moreover, molecular imaging can identify specific cancer cells by sensing biomarkers, which are extrinsic optical absorption contrast agents.

In photoacoustic imaging, there are two major modes: focused scanning and computed tomography. A focused ultrasonic transducer is usually used in focused scanning photoacoustic imaging, which will be presented in Chapter 4. The focus characteristic itself provides resolutions. For computed tomography, unfocused ultrasonic detectors are used. An inverse reconstruction algorithm is required to reconstruct the tomographic image. An exact closed-form reconstruction formula was studied for each of three detection configurations: planar, cylindrical, and spherical [85]. In our demonstration, we focused on a circular scan configuration to obtain a cross-sectional image, which is a two-dimensional (2-D) version of a cylindrical configuration. In circular-view photoacoustic tomography, ultrasonic detection follows a circle to acquire the photoacoustic data, which is then converted into the initial photoacoustic pressure distribution by an inverse algorithm. To enable the real-time imaging, an array of ultrasonic detectors in a circular shape can be adopted.

3.2 Motivation

3.2.1 Wideband photoacoustic tomography

For PAT, wideband response is important in the imaging reconstruction of absorbers with varied size scales. Currently, the detection typically relies on piezoelectric transducers. Piezoelectric transducers have limited bandwidth and thus can only respond to part of the spectrum of the acoustic waves. Hence, transducers with different central frequencies are employed to expand the detection bandwidth [86-87]. In general, a piezoelectric transducer with a higher central frequency can better detect the edge parts of

a structure, which has the characteristic of rapidly changing spatial absorption profile but is difficult to recognize the smooth parts of the structure with low spatial frequencies. On the other hand, a piezoelectric transducer with a lower central frequency behaves in the opposite way. Therefore, wide bandwidth receivers spanning the range of less than 1 M Hz to above 50 M Hz are essential for a complete, high-resolution, photoacoustic image reconstruction.

Optical detection in photoacoustic tomography offers several advantages. The frequency response ranges widely from low to high frequencies, enabling the interior of a large heterogeneity, including spatially slow and spatially sharp absorption, to be imaged. Thus, we used microring resonators for wideband photoacoustic tomography and demonstrated the improvement in imaging quality.

3.2.2 High-resolution photoacoustic tomography over a large imaging area

Since photoacoustic signals are 20 to 40 dB weaker than the ultrasound signals used in medical imaging, the detection methods for photoacoustic imaging typically rely on a single large size piezoelectric transducer because of its convenience and high sensitivity. The bandwidths of most piezoelectric transducers are usually limited to 60 % of the center frequency. The quality of the photoacoustic imaging can be degraded due to the large size and limited bandwidth [88]. Wideband piezoelectric detectors with very small active size can have wide detection angle but suffer from poor signal-to-noise ratio (SNR) because the sensitivity is dependent on the detector aperture size. For example, a

40 μm piezoelectric polyvinylidene fluoride (PVDF) transducer (HPM04/1, Precision Acoustics, Dorchester, Dorset, UK) has an noise-equivalent pressure (NEP) around 10 kPa over a 100 MHz bandwidth considering only the noise from its matched preamplifier (HP1, Precision Acoustics). Current reconstruction algorithm for photoacoustic imaging has been developed based on point detectors [85]. In practice, the finite-size detectors results in a trade-off between detection sensitivity and lateral resolution. As a result, optimal lateral resolution is achievable only within the focal zone, usually the center in a circular geometry. Besides, de-convolution of aperture effects may introduce artifacts and has not been accepted in clinical applications [89]. Thus, a small aperture detector with high sensitivity and wide bandwidth is highly desired for faithful reconstruction of optical absorption distributions in photoacoustic imaging.

The virtual point detector methods have been introduced to have small aperture size with high sensitivity [90-91]. However, the constructed virtual point detector has an effective size larger than 100 μm and a central frequency around 6 MHz with limited bandwidth. Such detectors can deteriorate the quality of photoacoustic imaging [88]. The sensitivity of microrings primarily depends on the optical quality factor (Q) of microring resonators rather than on the detector size directly. The optical ultrasound detection enables very wideband response, –3 dB bandwidth from DC to more than 90 MHz [19]. For this work, we have developed different sizes of microring resonators with low NEPs around 20–200 Pa over 1–75 MHz bandwidth: 100- and 90-μm-diameter microring operated at optical wavelength (λ) of 1550 nm [19, 22]; 60- and 40-μm-diameter microrings operated at λ = 780 nm [24]. The low NEP, wide acceptance angle, and wideband response provided by the microring devices will directly benefit the quality of

photoacoustic imaging. The new generation of microrings can also be applied to other ultrasound-related imaging.

3.3 Reconstruction algorithm

As has been described in the literature [75, 92], in an acoustically homogenous medium, the generation and propagation of a PA pressure wave $p(\mathbf{r},t)$ at position $\mathbf{r}$ and time t in response to a heat source can be expressed as

$$\nabla^2 p(\mathbf{r},t) - \frac{1}{c^2}\frac{\partial^2}{\partial t^2} p(\mathbf{r},t) = -\frac{\beta}{C_p}\frac{\partial}{\partial t} H(\mathbf{r},t), \tag{3.1}$$

where c is the speed of sound in the medium, β denotes the thermal coefficient of volume expansion, C_p denotes the isobaric specific heat capacity, and $H(\mathbf{r},t)$ is the heating function defined as the thermal energy converted at $\mathbf{r}$ and t per unit volume and time. The heating function can be written as the product of an optical energy absorption A within the material at position $\mathbf{r}$ and a short irradiation pulse $I(t)$, i.e.,

$$H(\mathbf{r},t) = A(\mathbf{r})I(t). \tag{3.2}$$

The $I(t)$ is usually represented as a delta-function laser pulse in the derivation. All absorbed optical energy is assumed to be converted into heat.

The algorithm in PAT is designed to reconstruct the absorption distribution $A(\mathbf{r})$ from the measured pressure $p(\mathbf{r},t)$ at various positions $\mathbf{r}$. The exact inverse solution has been derived although it is computationally time consuming [93]. Fortunately, when the scanning radius, ρ_0, is much longer than the generated PA wavelengths, λ_a, as is the case in high-resolution PAT, the inverse solution has an approximated form [92]:

$$A(\rho,\phi,z) = -\frac{C_p}{2\pi c^4 \beta}\iint_{S_0} dS_0 \cos\Theta \frac{1}{t}\frac{\partial p(\mathrm{r}_0,t)}{\partial t}\Big|_{t=\frac{|\mathrm{r}-\mathrm{r}_0|}{c}}, \tag{3.3}$$

where S_0 is the measurement surface with a cylindrical surface $\mathbf{r}_0 = (\rho_0, \square_0, z_0)$; Θ is the angle between the detector surface normal direction and the vector from the detector to the reconstruction point. From Equation (3.3), the absorption distribution can be calculated by means of modified back projection of quantity $-(1/t)((\partial p(\mathbf{r}_0,t))/\partial t)|_{t=|\mathbf{r}-\mathbf{r}_0|/c}$, which is a good approximation under the far-field condition $k\rho_0 >> 1$ and $k|\mathbf{r}\text{-}\mathbf{r}_0| >> 1$, where $k = \omega_a/c$ is the wavenumber of the acoustic signals.

The PA pressure immediately generated by a spherical fluid object, illuminated by an infinite-short laser pulse, in an optically transparent fluid background that has the same sound speed and density as the object is given by [75]

$$p_\delta(t) = \frac{c^2\beta W}{2C_p r} U(R - |r - ct|)(r - ct), \tag{3.4}$$

where W is the absorbed energy density, r is the distance from the object center, R is the radius of the object, and t is the time, and $U(\xi) = 1$ for $\xi \geq 0$ and $U(\xi) = 0$ otherwise. In practice, the measured PA pressure by an ultrasonic detector can be expressed as the convolution of multiple functions:

$$p(\mathrm{r}_0,t) = p_\delta(\mathrm{r}_0,t) * I(t) * L(t) * D(t), \tag{3.5}$$

where $L(t)$ accounts for the propagation loss in the medium, $D(t)$ is the impulse response of the detector, and * represents convolution. The last three terms in Equation (3.5) are the factors that distort the original absorption $A(\mathbf{r})$ in real applications. In the following

simulation, Equation (3.5) will be substituted into Equation (3.3) to evaluate the reconstructed PAT images.

3.4 Wideband photoacoustic tomography

We use photoacoustic imaging to quantitatively explore the potential of wideband response of polymer microring resonators. To prove the benefits of wideband response, we present the simulation results of photoacoustic tomography using both microring sensors and piezoelectric transducers to provide comparisons. Experimental results of photoacoustic tomography using polymer microring resonators are also demonstrated. Imaging resolution and issues regarding agreement between theories and experiments are discussed.

3.4.1 Wideband photoacoustic tomography: simulations

To compare our microring device with the piezoelectric transducers, images from both numerically simulated and experimental data were reconstructed in a 2-D case, which was chosen to reduce the computational and experimental complexity. For the 2-D case, the reconstruction equation can be derived from Equation (3.3) by setting $z = 0$ and using a circular measurement configuration.

Photoacoustic tomography of two polystyrene (PS) beads with diameters of 50 and 300 μm was numerically simulated. To compare the frequency response only, the beads were positioned at the center of the detection circle to neglect the effect of finite

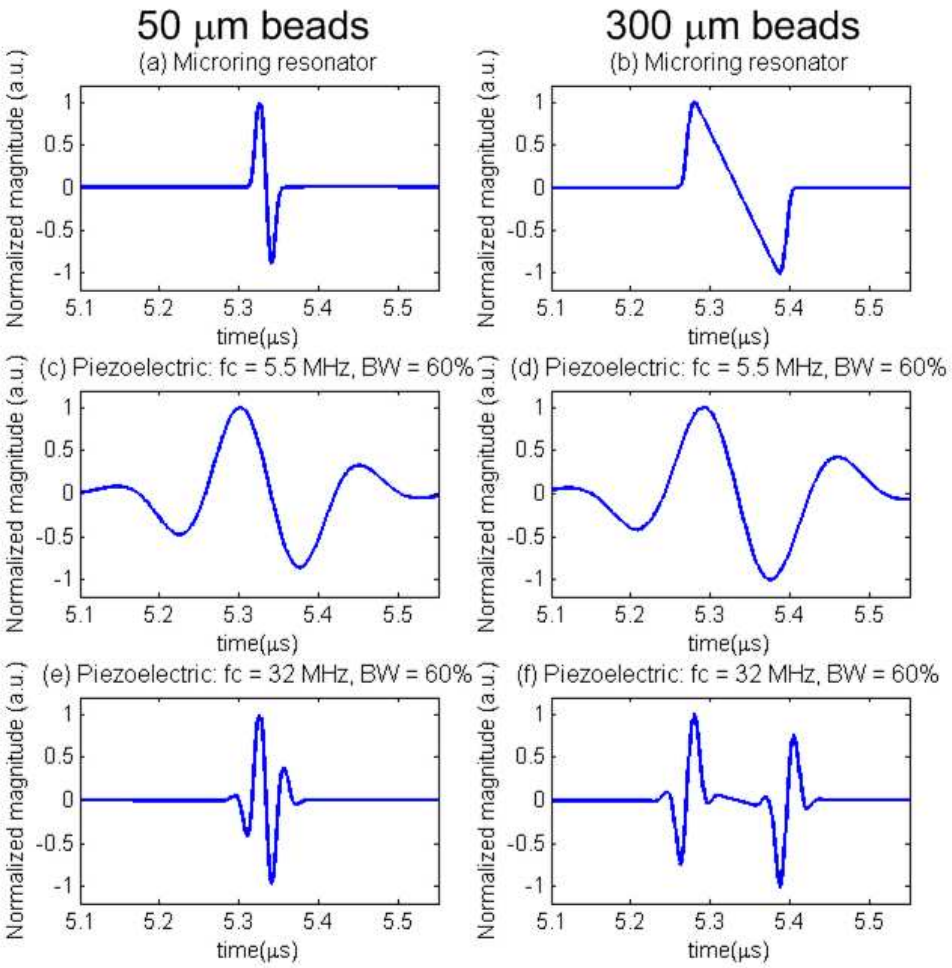

Figure 3.1 The simulated photoacoustic signals of a 50 μm PS bead (left column) and a 300 μm PS bead (right column) detected by microring resonators, piezoelectric transducers with a central frequency of 5.5 MHz and 60% bandwidth, and piezoelectric transducers with a central frequency of 32 MHz and 60% bandwidth, respectively.

detector aperture size [86, 88]. Assuming a uniform absorption distribution within the spherical beads, the analytical expression for their photoacoustic signal is given in [31, 75, 94]. The $p_\delta(\mathbf{r}_0,t)$ function with respect to t has an N shape. Figure 3.1(a) and (b) show a smoothed N shape. Since the acoustic speed of PS beads, ~ 2380 m/s [79], is different from that of its surrounding water media, 1480 m/s, we used scaled bead size in the

simulation. That is, a reduction ratio of 0.622 [= 1480 / 2380] in bead's size was used. Therefore, the effective sizes of 50 and 300 μm beads are 31.1 and 186.6 μm, respectively. The main beam of the spectrum of the N-shaped $p_\delta(\mathbf{r}_0,t)$ is of a bell shape with maximum amplitude at 32 and 5.5 MHz for the 50 and 300 μm beads, respectively. Therefore, two theoretical piezoelectric transducers with central frequency of 5.5 and 32 MHz and a –3 dB bandwidth of 60% were used. For microring resonators, the frequency response range was from DC to 90 MHz at –3 dB according to previous experimental results [19].

The radius of the circle of detection is set at 8 mm, which was chosen to be close to our experimental conditions. The angular scanning range was 2π with 72 steps and the photoacoustic signals were sampled at a sampling rate of 1 GHz. Figure 3.1 shows the simulated temporal signals detected from the 50 μm and 300 μm diameter beads using three kinds of detectors: microring resonators and piezoelectric transducers with two types of frequency response described above. Compared with the relatively sharp N-shape in Figure 3.1(b), the relatively smoothed N-shape signal in Figure 3.1(a) is mainly due to the finite duration of the pulse laser, ~ 6 ns, which is comparable to the acoustic transit time in the 50 μm PS beads, ~21 ns [= (50 μm)/(2380 m/s)]. A secondary factor is that the spectrum of 50 μm PS beads has a larger high-frequency component and thus more acoustic absorption loss was encountered. In Figure 3.1(c)-(f), the N-shape disappeared due to the impulse response of a limited bandwidth of the piezoelectric transducers. Figure 3.1(c) shows the 50 μm PS beads detected by relatively low-frequency transducers and thus the signal was largely expanded in time domain. Figure

3.1(f) is the opposite: a high-frequency transducer catches only the sharp boundary part of the N-shape. Figure 3.1(d) and Figure 3.1(e) is similar because one is the scaling of the other.

Figure 3.2(a)-(f) show the reconstructed images from the simulated signals,

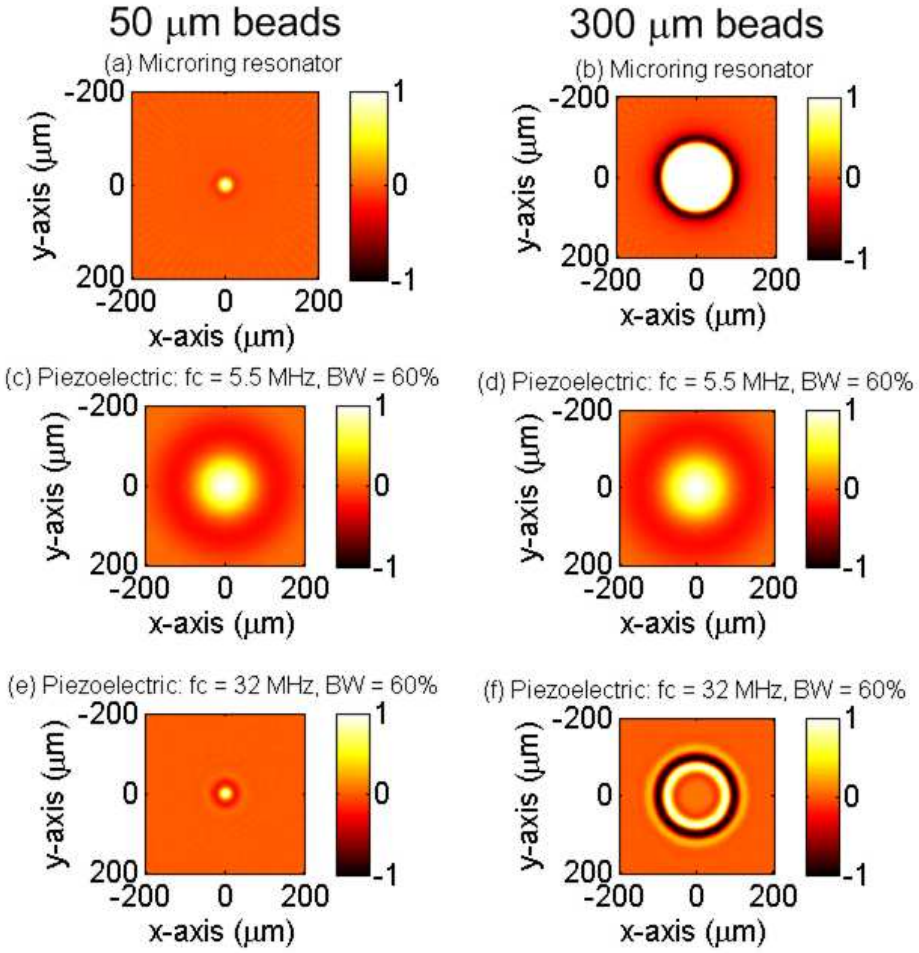

Figure 3.2 The reconstructed image of a 50 μm PS bead (left column) and a 300 μm PS bead (right column) using microring resonator detectors, piezoelectric transducers with a central frequency of 5.5 MHz and 60% bandwidth, and piezoelectric transducers with a central frequency of 32 MHz and 60% bandwidth, respectively. Note that the effective sizes of the beads in water are 31.1 and 186.6 μm, respectively.

corresponding to Figure 3.2(a)-(f), respectively. For better comparisons, the line profile of the reconstructed image and the original absorption distribution at y = 0 μm was plotted in Figure 3.3. Again, Figure 3.3(a)-(f) was extracted from the 2-D images in Figure 3.2(a)-(f), respectively. The reconstructed image shown in Figure 3.3(b) is in good agreement with the bead profile, which preserves both the boundary of the large bead and the uniform absorption distribution in the inner part. The boundaries of large objects generate relatively high frequency signals. The slowly varying absorption profile within the objects has characteristic low frequency components. In other words, only a detector with wideband response to photoacoustic signals can restore both types of features. In Figure 3.3(a), the smoothing of the boundary and the reduced imaging size, ~ 22 μm full-width at half maximum (FWHM), is mainly due to the finite duration of the pulse laser and the water absorption, as described above. Figure 3.3(c) shows a very blurred image because the transducer catches only the very low frequency part of the spectrum from the 50 μm PS bead. The sharp boundaries were not captured in Figure 3.3(a), (d), and (e), while in Figure 3.3(f), only the boundary was detected but not the uniform absorption inside the bead.

3.4.2 Wideband photoacoustic tomography: experiments

The experimental setup is shown in Figure 3.4. A black PS bead was first fixed in a gel made by mixing water and 1% agarose (GPG/LE, American Bioanalytical, Natick, MA). Then the phantom was placed in deionized water. A 532 nm pulse laser (Surelite I-20 with ~ 6 ns pulse width, Continuum, Santa Clara, CA) was used to illuminate the

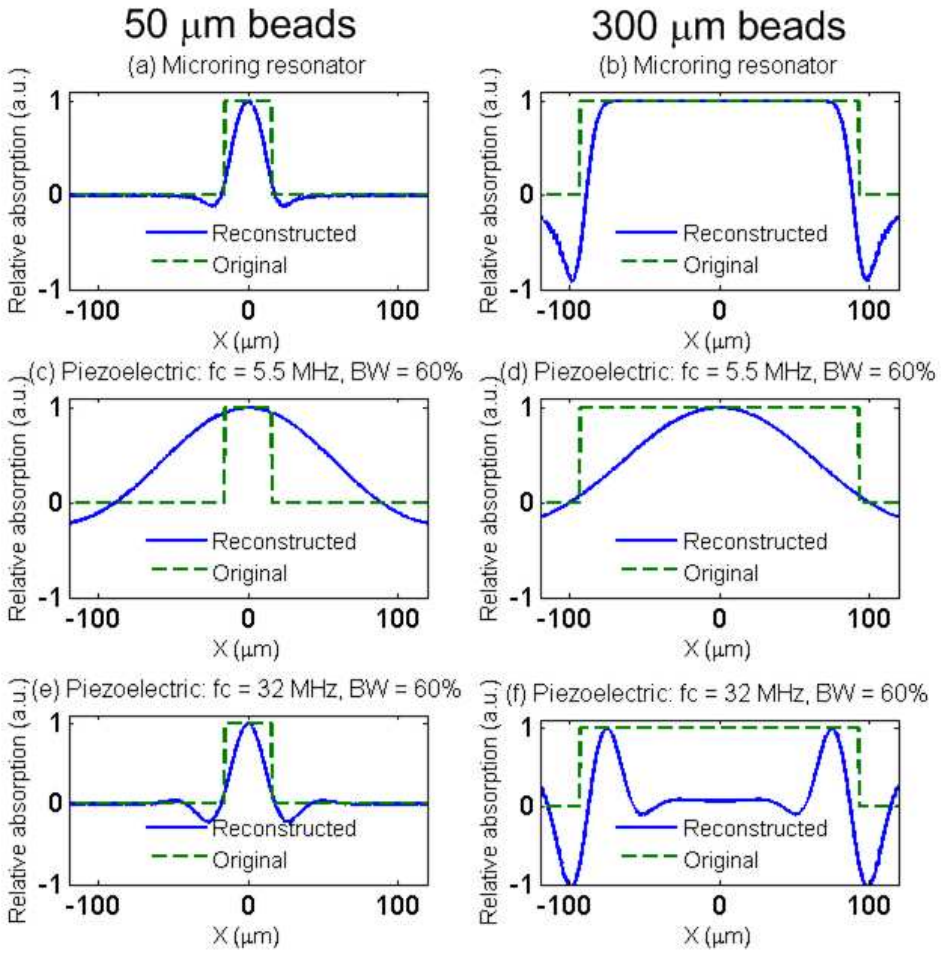

Figure 3.3 The line profile of reconstructed image at y = 0 μm. The line profile (a)-(f) corresponds to the 2-D images (a)-(f) in Figure 6, respectively. Note that the effective sizes of the beads in water are 31.1 and 186.6 μm, respectively.

bead. The laser light was delivered to the phantom through free space. The beam width was ~ 4.5 mm without any beam focusing. A circular rotation stage was used. The light source illuminating the bead was fixed in place while the detector rotated around the objects.

In photoacoustic tomography experiments, we measured the transmission spectrum of the microring device, as shown in the inset of Figure 3.4. From the spectrum,

the probing wavelength was thus chosen at 1558.42 nm. A 49 μm-diameter black PS bead was first fixed in a gel. Then the phantom was placed in deionized water at a distance of ~ 6.5 mm from the device. A 532 nm pulse laser was delivered to the bead from top at a fluence of 9.5 mJ/cm^2. During the experiment, the microring detector scanned around the sample at a radius of 6.5 mm from 0° to 360° with a step size of 5°. The photoacoustic signals were sampled for 5 μs at a sampling rate of 1 GHz.

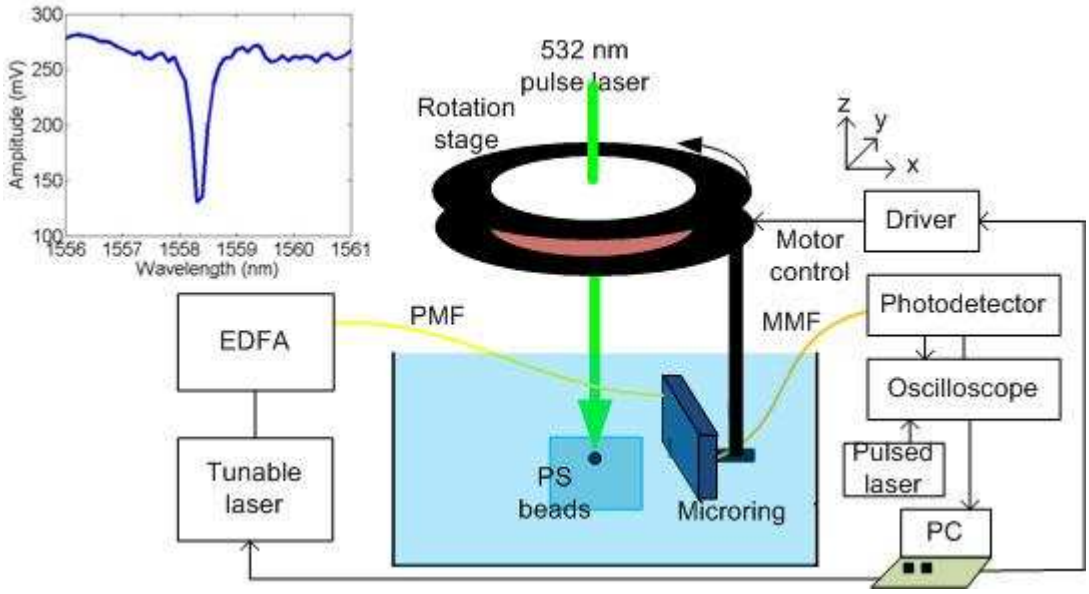

Figure 3.4 Experimental apparatus for photoacoustic tomography to image 49 μm and 301 μm diameter beads. The PS beads produce an acoustic wave, and the microring resonator is scanned in a circular measurement configuration. The gel containing the PS bead and the microring resonator were immersed in deionized water. The inset shows the transmission spectrum of microring resonator.

Figure 3.5(a) shows the reconstructed image from the experimental data and Figure 3.5(b) shows the detected photoacoustic signal at a particular angle and a simulated signal. The two signals agree well with each other. In principle, the signals detected from different angles should be similar since the object was positioned close to

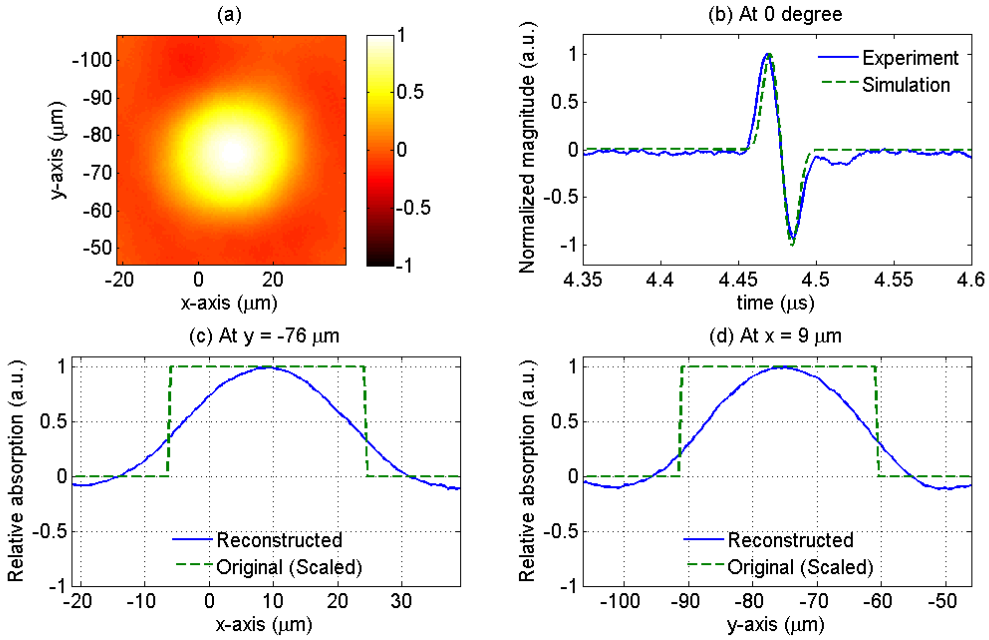

Figure 3.5 Photoacoustic tomography of a 49 μm bead. (a) Reconstructed image; (b) Measured and simulated acoustic signals at one particular angle; (c) The line profile of the reconstructed image at y = -76 μm; (d) The line profile of the reconstructed image at x = -9 μm. The center of bead's image is at about x = 9 μm and y = -76 μm.

the center of the detection circle. A smaller size detector will alleviate the aperture effect and thus is helpful to expand the imaging area. Figure 3.5(c) and (d) show the line profile of the reconstructed image across the center, at y = -76 μm and x = 9 μm, respectively.

As mentioned above, the scaled bead size was used to verify the reconstructed image. In real application, the speed of sound in most soft tissues is relatively constant (~ 1540 m/s), and thus the tomography can reconstruct the original sizes of absorbers. Although the smoothing of the boundary in Figure 3.5(c) and (d) was relatively obvious due to the loss in the high-frequency and the finite pulse duration, an N-shape signal was maintained because of the wideband response of the polymer microring resonator. The

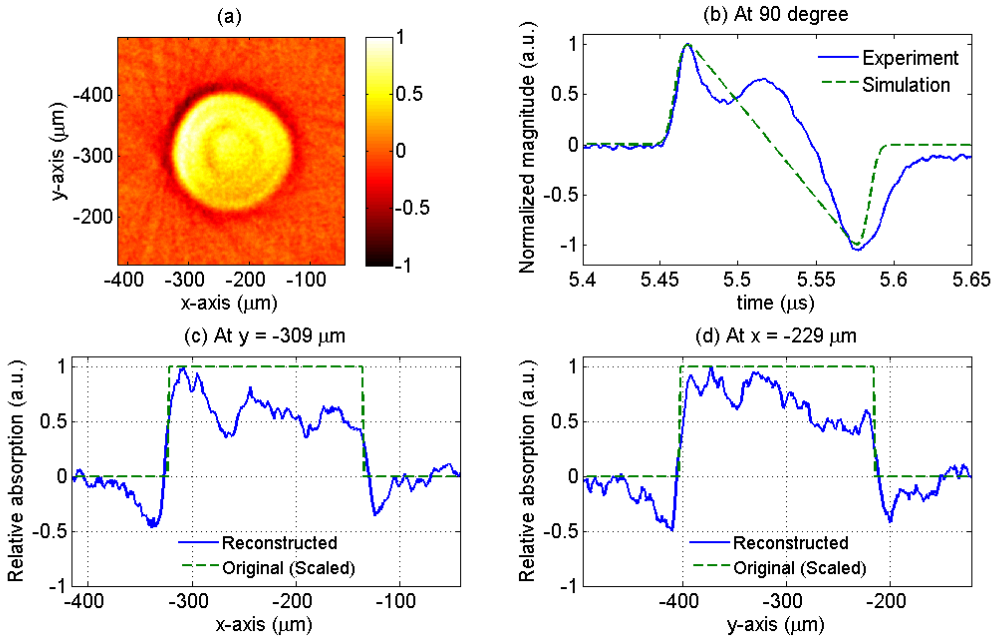

Figure 3.6 Photoacoustic tomography of a 301 μm bead. (a) Reconstructed image; (b) Measured and simulated acoustic signals at one particular angle; (c) The line profile of the reconstructed image at y = -309 μm; (d) The line profile of the reconstructed image at x = -229 μm. The center of bead's image is at about x = -229 μm and y = -309 μm.

reduced imaging size, ~ 25.5 μm FWHM, underestimates the scaled bead's size, 30.5 μm [= 49 × 0.622], as predicted by simulations.

For the case of 301 μm-diameter beads (BK300T, Microgenics Corp., Fremont, CA), the experimental setup and methods are similar except a lower fluence of 1.9 mJ/cm^2 was used because the black-dye bleaches more easily due to enhanced absorption in the larger beads. Figure 3.6 shows the reconstructed image and photoacoustic signals. The size of the reconstructed image fits the scaled size well, ~ 187 μm [= 301 × 0.622]. Unlike the 49 μm bead case, we were able to obtain an image size very close to the actual bead size because the laser pulse is sufficiently short for the large size bead and the main

temporal spectrum of 301 μm beads falls primarily in the low frequency range. The boundaries between the beads and the surrounding medium are imaged clearly.

3.4.3 Discussion

In the photoacoustic tomography of 301 μm PS beads presented in Section 3.3.2, it can be seen that the absorption distribution inside the beads is not as uniform as one would expect. This can be attributed to several factors. Firstly, since light travels 6 times longer distance in a 301 μm bead than that in a 49 μm bead, it can cause more non-uniform absorption between the top and bottom parts of the beads. Besides the non-uniform absorption in the vertical direction (i.e. along the light path), the peripheral part of the bead with less thickness is easier to have uniform absorption of light energy than the central part. That is, the non-uniform light absorption exists in the imaging plane and along the direction normal to the imaging plane. Assuming a spatially uniform laser light incident from –z to +z direction and an absorption coefficient of 50 cm^{-1} of the dye-doped beads, simulation results presented in Figure 3.7(a) and (b) show a more non-uniform absorption distribution in a 300 μm diameter bead compared to a 50 μm diameter bead. Secondly, since the refractive index of the PS beads is larger than that of water, light is focused to the central region of the bead, but not to a well-defined focal point due to the spherical aberration. This focusing effect might explain the brighter image in the center part of 301 μm diameter beads, as shown in Figure 3.6(a). Such effect will be much less serious in real applications because the refractive index of tissues is close to that of water [95-96] and the shape of tissue is more irregular. Thirdly, the requirement of the spatial

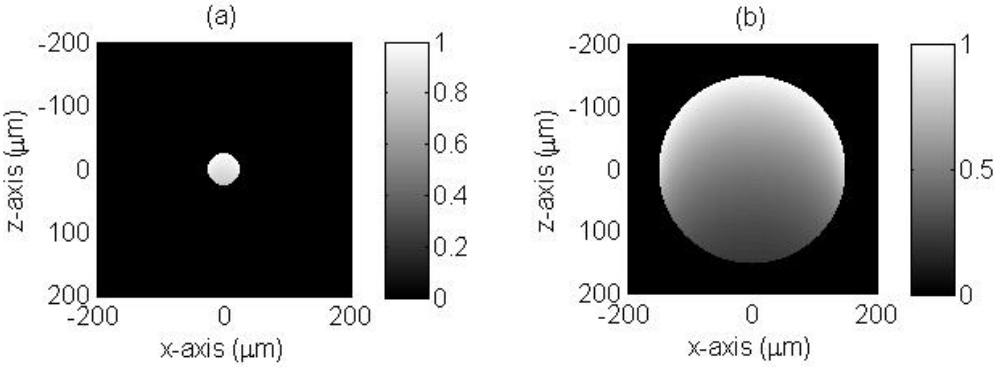

Figure 3.7 The simulated absorption distribution of (a) 50 and (b) 300 μm diameter beads. A spatially uniform light source and an absorption coefficient of 50 cm^{-1} of the dye-doped beads are assumed.

uniformity of pulse laser energy is more critical when the object size is larger. These factors may explain a distorted N-shape acoustic signal in Figure 3.6 (a). The exact reason is under investigation.

Finally, to evaluate the imaging resolution of polymer microring resonators, we compare a similar experiment of imaging hair fibers with a diameter of ~ 60 μm, as performed in [86] that used piezoelectric transducers. The zero-crossing widths of the positive main lobes of the reconstructed images are 270 μm, 120 μm, and 90 μm for the three transducers: 3.5 MHz, 10 MHz, and 20 MHz. These commercial transducers have nominal bandwidths of 50% to 80% of their central frequencies. The resolution of an image was defined in [86] as the width of the main lobe at zero-crossing point minus the width of the imaged hair. Therefore, the corresponding image resolutions were approximately 210 μm, 60 μm, and 30 μm for the above three transducers, respectively. In this work of using the microring detector to image the 49 μm PS bead, the zero-crossing width of the reconstructed imaging is approximately 43 μm. Due to the mismatch of sound speed in PS and in water, the effective bead size in water is 30.5 μm.

Using the same definition as in [86], the image resolution is 12.5 μm, which is much higher than those obtained by the above three piezoelectric transducers.

3.5 Photoacoustic tomography using low-noise small size microrings

We conduct PAT to show the distinctive advantages provided by small size microrings. Both simulation and experiments of PAT with different detector sizes are demonstrated.

3.5.1 Photoacoustic tomography: simulations

To demonstrate the advantages of the small size microrings, we studied PAT images from both numerical simulations and phantom experiments in a 2-D case for convenience although 3-D imaging is equally feasible. PS beads with sizes of 100 and 50 μm were considered in simulation. Due to the sound speed difference of PS beads, 2380 m/s, and the surrounding water, 1480 m/s, we considered the effective sizes of 62 and 31 μm in the simulation [20]. Two different sizes of beads were used to generate photoacoustic signals of different frequency ranges, and thus can evaluate the effect of frequency-dependent directivity of detectors. The beads were positioned at three different locations: from the center of scanning circle to off center positions at 4 mm and 8 mm, respectively, as shown in Figure 3.8. The scanning radius was 12 mm with a step size of 3°/step, and the scanning center was set as coordinates (0, 0) with three beads at

coordinates A (0,0), B (4,0), and C (8,0) mm. In order to have the same wide acceptance angle, smaller detector size is required for higher frequency signals. For comparisons, an aperture size 500 μm wideband hydrophone (http://www.acoustics.co.uk/products/hpm05-3) with a NEP of 200 Pa, similar to or worse than the NEPs of our microrings, was also simulated.

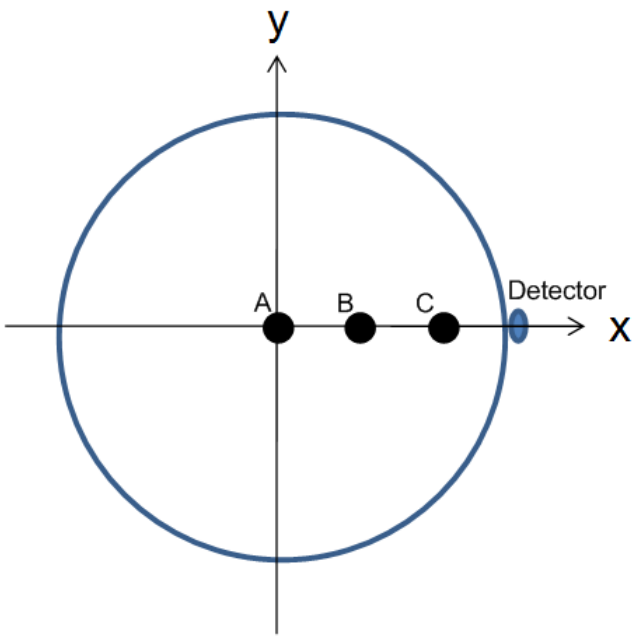

Figure 3.8 Diagram of beads positions and scanning geometry in PAT experiments.

The duration of 6-ns laser pulse, which will be used in experiments, is considered. In our case, $L(t)$ in Equation (3.5) is mainly due to water absorption, which has an attenuation coefficient of 2.2×10^{-4} dB/mm-MHz^2 [77]. $D(t)$ includes the frequency and angular response of the detectors. A DC-100 MHz bandwidth is assumed for wideband microrings and hydrophones. The frequency-dependent angular response of microrings and hydrophones can be understood by considering a ring and disk piston transducer,

respectively. The theoretical angular response or directivity d has been described [78]: $d(\theta) = J_0(ka\sin(\theta))$ and $d(\theta) = J_1(ka\sin(\theta))/(ka\sin(\theta))$ for ring and for disk, respectively, where $k = \omega_a/c$ is the wave number of the incident acoustic signal, a the average radius of the element, and θ the incident angle of the acoustic wave.

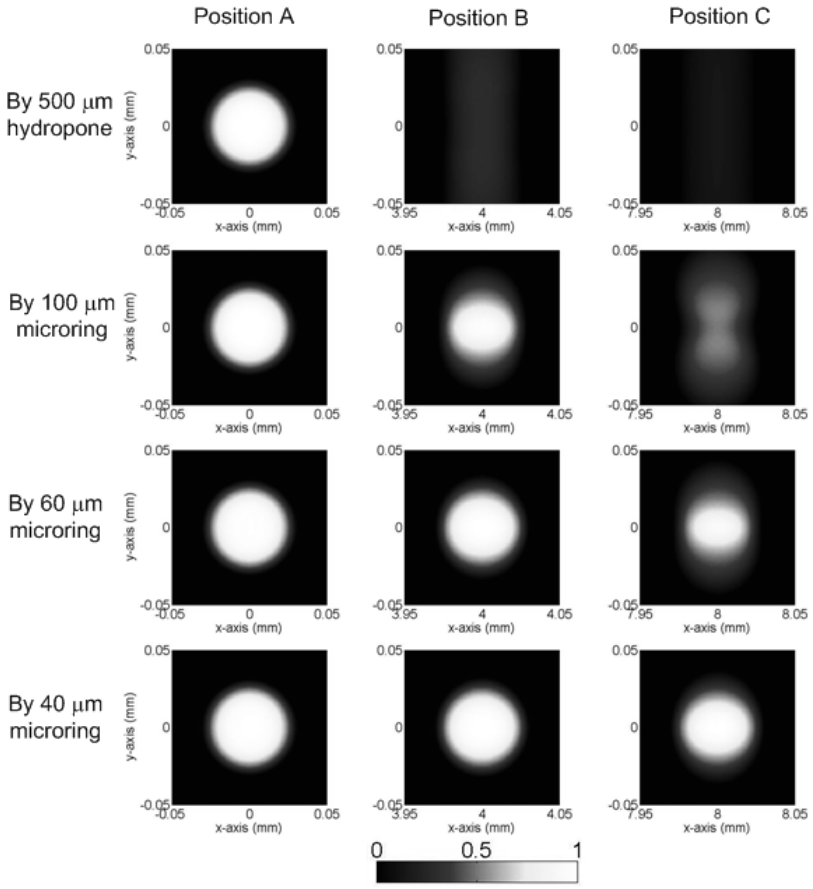

Figure 3.9 Simulated PAT images of 100 μm PS beads (effective size = 62 μm) using different types of detectors.

Figures 3.9 and 3.10 show the simulated PAT images of 100 and 50 μm size PS beads using 500 μm hydrophone and different sizes of microrings. In Figure 3.9, for the beads located at the center (i.e. position A) there is no difference in imaging contrast and

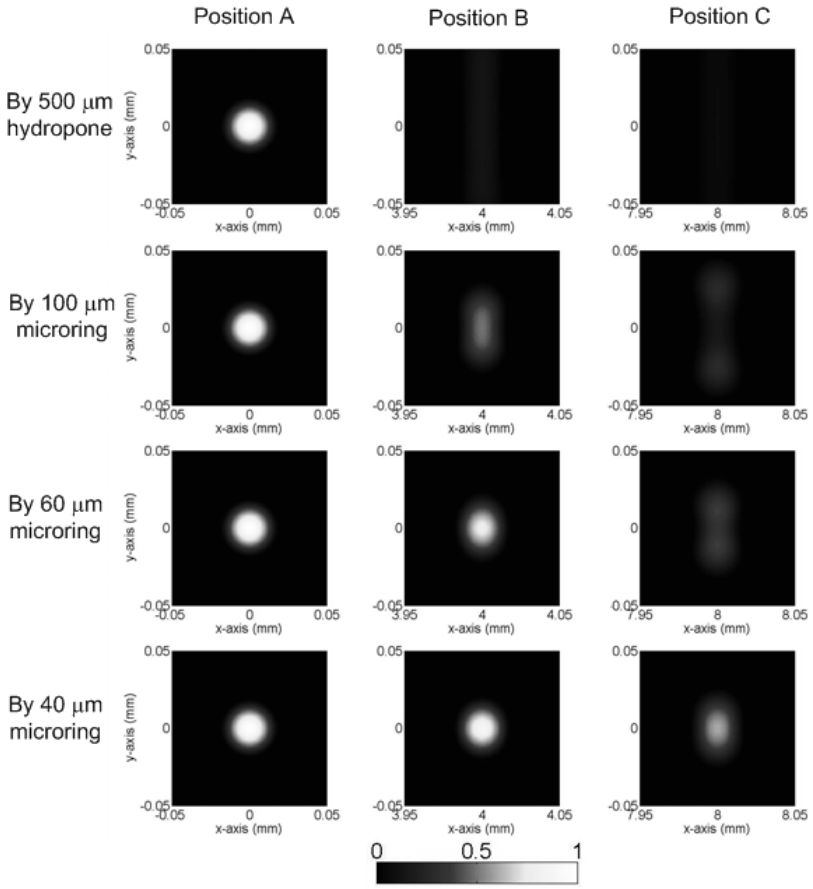

Figure 3.10 Simulated PAT images of 50 μm PS beads (effective size = 31 μm) using different types of detectors.

resolution because the angle of all the impinging photoacoustic waves to the detectors are 0°, which gives the best angular response of all four detectors. As the beads position is farther from the center, from position B to C, both image contrast and resolution deteriorate because of narrower angular response. The 500 μm hydrophone only produces a very blurred imaging in y direction along with very poor imaging contrast. This is primarily due to the large angular dependence of the detector response resulting in very small acceptance angle. Such undesirable effects can be effectively mitigated by using smaller size detectors, as can be seen in Figure 3.9 when the detector size is reduced from 100 μm to 40 μm. Especially with a 40 μm microring, the imaging quality in position B

and C is almost completely restored and nearly identical to that of the central bead. A noticeable blurring is only observed for the bead at the far end position C.

Next different bead sizes are evaluated for obtainable resolution. The PAT imaging of 50 μm beads are shown in Figure 3.10. Beads at position A have good imaging quality no matter what sizes of detectors are used, as explained above. However, the imaging quality of beads farther away from the center quickly deteriorates: the 50 μm bead becomes undetectable even at position B by using standard 500 μm size hydrophone. The situation improves by using smaller microring detectors, and a 40 μm size microring can produce acceptable image contrast for bead at location C. Comparing with 100 μm beads in Figure 3.9, the imaging quality of 50 μm beads suffers much more by using large size detectors. Take the images of 100 and 50 μm beads at position C by 60 μm microring for example, the 1-D PAT profile along y of 100 μm beads have better imaging contrast and less blurring than that of 50 μm beads (Figure 3.11). This can be understood because that the smaller beads generate higher-frequency photoacoustic signals, and thus a smaller detector is needed to obtain wide enough acceptance angles. If the spatial resolution is defined as the FWHM, the 40 μm microrings yielded a high resolution of 22 μm in x-direction and 30 μm in y-direction for beads at position C with more than 0.5 imaging contrast. As a reference, previously reported virtual point detectors can only produce resolution of hundreds of μm [90-91]. Thus, with a low-noise small size microring, the high resolution and good imaging contrast can be preserved even in regions far from the center. While in principle a large scanning radius could mitigate the aperture effects, a scanning circle as small as the objects, such as a mouse head, can be used to minimize the attenuation of photoacoustic C signals.

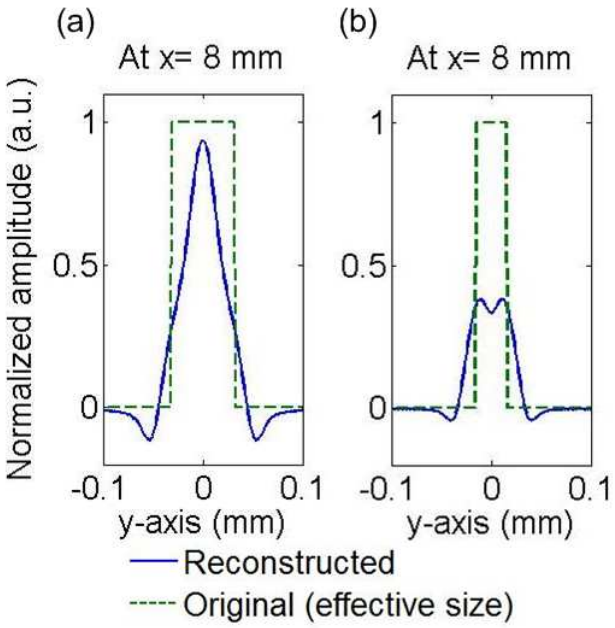

Figure 3.11 Simulated 1-D PAT profile along y of (a) 100 μm and (b) 50 μm PS beads at position C using 60 μm microring detectors.

3.5.2 Photoacoustic tomography: experiments

Small rings with high sensitivity are obtained from extensive work to optimize the fabrication process. Detailed discussions can be found in References [22,24]. The photoacoustic signals were collected by a digital oscilloscope (WaveSurfer 452, LeCroy, Chestnut Ridge, NY) with a sampling rate of 500 MHz. The PS beads were fixed in a gel made by mixing water and 1% agarose (GPG/LE, American Bioanalytical, Natick, MA) and placed in deionized water. A 532 nm pulsed laser (Surelite I-20, Continuum, Santa Clara, CA) with a 6 ns pulse duration was delivered from top to the beads. A circular scan around the objects was realized by using a rotation stage. During the experiment, the microring detector scanned around the sample at a radius of ~12 mm with a step size of 3°.

Figures 3.12 and 3.13 show the experimental PAT images of 100 and 50 μm beads, respectively, reconstructed from signals taken from the microring detectors. The beads were positioned close to, although not exactly at, the coordinates (0, 0), (4, 0), and (8, 0) mm. For the 100 μm beads around position A, the imaged size well fits the effective size, ~62 μm, as shown in Figure 3.12. Furthermore, all sizes of microrings produce good imaging contrast. Only a little image distortion can be seen in the case of using 100 μm microring, which may result from the fact that the bead was not well

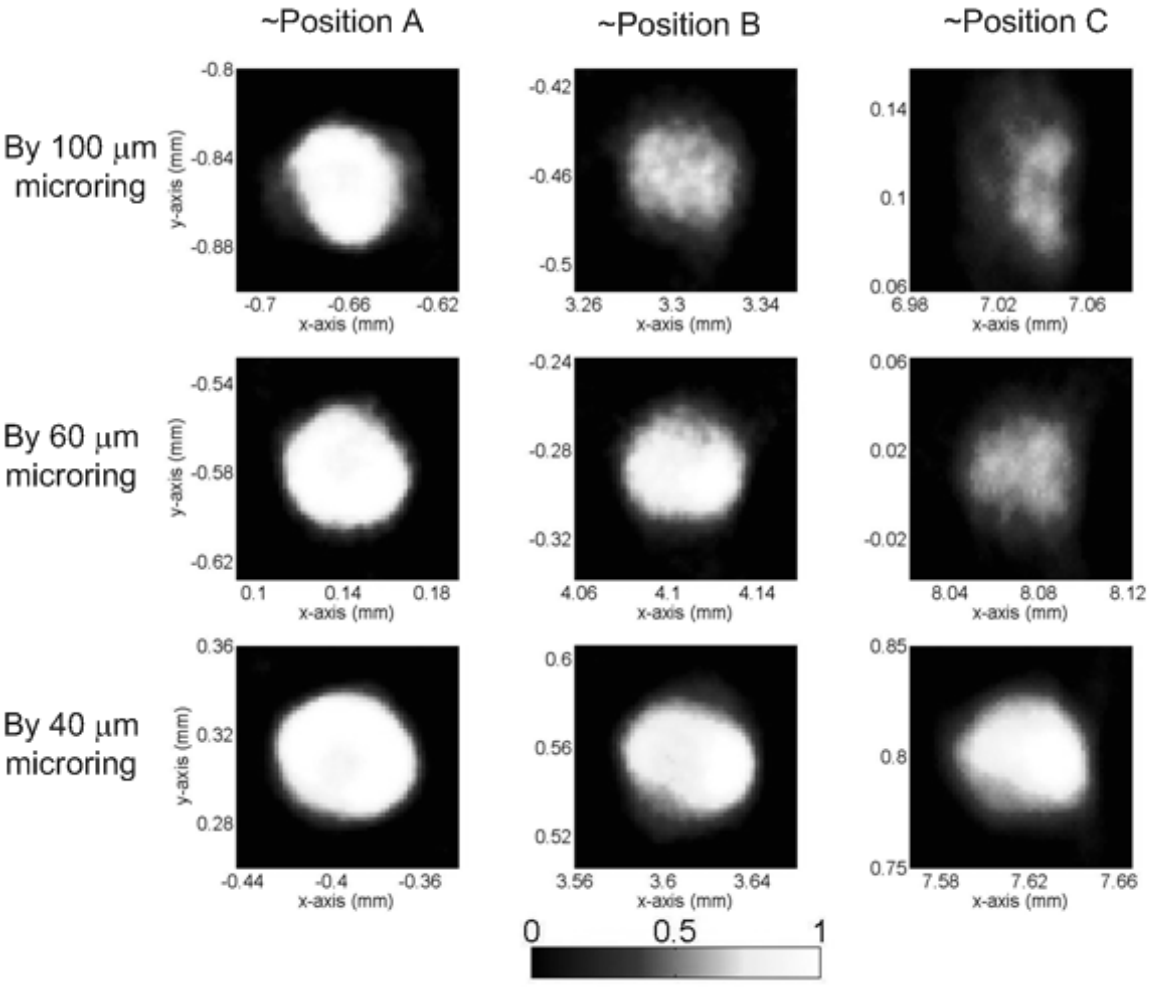

Figure 3.12 PAT images of 100 μm PS beads (effective size = 62 μm) using microrings.

positioned at the center and the poorer directivity of the detector with the largest size of all used in our experiment. Overall, the image quality worsens from position B to C, as expected from the simulation results. On the other hand, the image quality is significantly improved by using 40 μm microring in all cases, also consistent with the simulation. A little discrepancy for all images between Figure 3.9 and 3.12 could be due to the non-uniform laser absorption in the 100 μm beads [20]. For the 50 μm beads case, the experimental results in Figure 3.13 shows excellent agreement with the simulation results

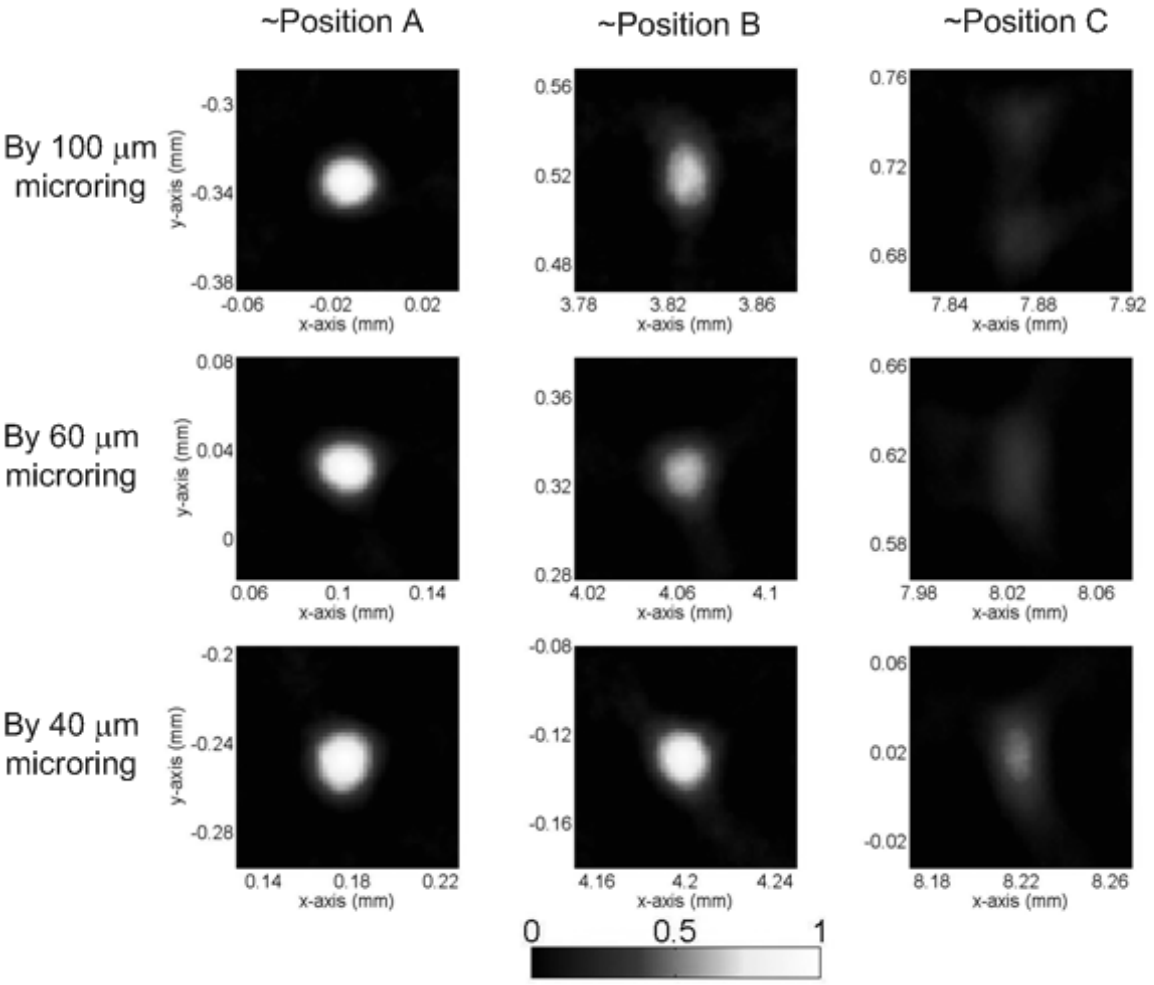

Figure 3.13 PAT images of 50 μm PS beads (effective size = 31 μm) using microrings.

in Figure 3.10, except for slightly lower imaging contrast in imaged beads around position B by 60 μm microring. These results serve as direct experimental proof that the small size microring detectors have much less aperture effects. For the beads around position C by 40 μm microring, a high resolution of 21 μm in x direction and 41 μm in y direction with imaging contrast of 0.5 was obtained, demonstrating the superior performance of the small size microring as compared with other detectors reported in the literatures. Development of even smaller microrings with high sensitivity would further improve the imaging quality at regions far from the center.

Chapter 4 Photoacoustic microscopy

4.1 Introduction

High-resolution microscopy in *in vivo* biomedical imaging enhances the understanding of various biological functions. For example, high-resolution brain imaging facilitates the studies of cognitive phenomena and neurological diseases. However, current pure optical microscopy has difficulties in *in vivo* imaging due to strong optical scattering and absorption of tissues, degrading the imaging resolution and signal-to-noise ratio (SNR). Photoacoustic microscopy (PAM) suggests a potential solution.

Several schemes of photoacoustic microscopy have been explored. In terms of resolution, photoacoustic microscopy can be categorized into 2 types: acoustic-resolution photoacoustic microscopy and optical-resolution photoacoustic microscopy. The first type is also called dark-field confocal photoacoustic microscopy [97-101]. Figure 4.1 shows the photoacoustic microscopy system [97]. An optical fiber is used to deliver the excitation laser light, which is monitored by a photodiode to solve the issue of energy fluctuation. To avoid stronger photoacoustic signals generated from surface than those from deeper targets to image, a conical lens is used to form a toroidal beam. Thus, annular illumination with a dark center, (i.e., dark field) is formed. The laser is then weakly focused on the target and an ultrasonic transducer focuses coaxially on the same

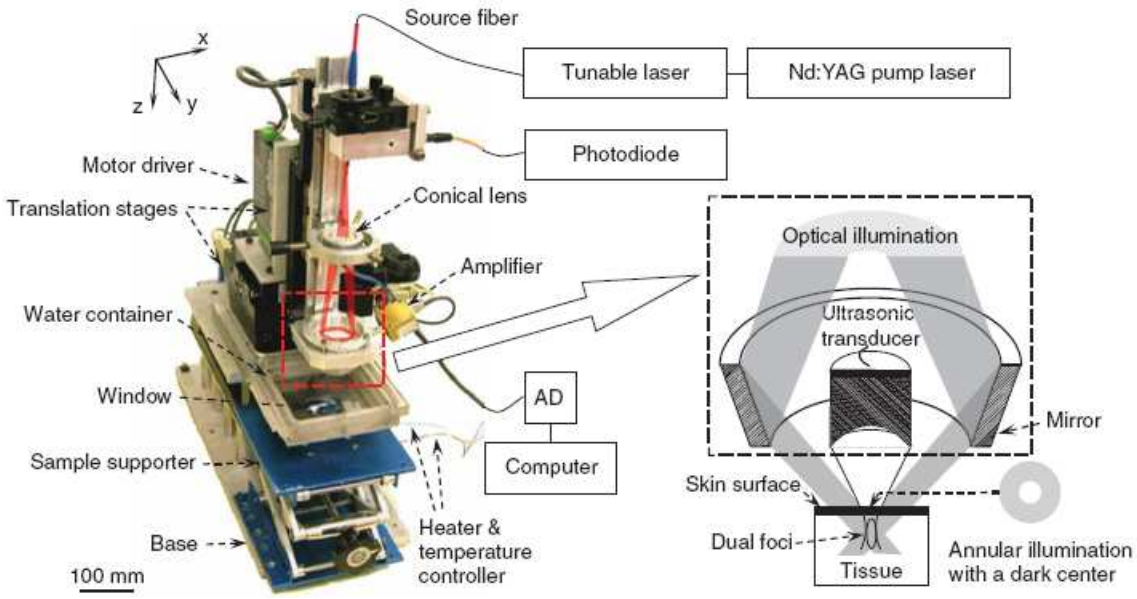

Figure 4.1 Dark-field confocal photoacoustic microscopy system [97].

region, giving a scheme of confocal excitation and detection. The time-of-flight photoacoustic signal is recorded by the ultrasonic transducer. The signal is converted into depth information, also called A-line, by assuming the speed of sound as ~1.54 mm/μs. Then, 1D depth image is consequently obtained. To produce two-dimensional (2-D) or three-dimensional (3-D) images, linear or raster scanning can be used, respectively. A high-frequency (>50 MHz) ultrasonic transducer with broad bandwidth is usually used. With such arrangement, both the lateral and axial resolutions are determined by acoustic signals. The numerical aperture and center frequency of the ultrasonic transducer determine the focal diameter, giving the lateral resolution, ~50 μm. The axial resolution, decided by the ultrasonic bandwidth, is ~15 μm. Ultrasonic attenuation in tissue determines the maximum imaging depth, greater than 3 mm [97-98]. As a result, dark-field confocal system can image optical absorption contrast at depths beyond the optical

mean free path (~1 mm in human skin), and the ratio of penetration depth to resolution is greater than 100 [97-98]. Note that the ratio is scalable by changing the specification of ultrasonic detector. For example, a 5 MHz ultrasonic transducer can produce a penetration depth to 30 mm with resolutions of 560 and 144 μm in the lateral and axial directions, respectively [99].

The acoustic resolution is not able to resolve capillaries, the smallest blood vessels. To solve the issue, the optical-resolution photoacoustic microscopy, capable of imaging single capillaries, is proposed [102]. The light is focused through an objective lens with a numerical aperture of 0.1, resulting in a high lateral resolution, ~5 mm, decided by the optical focal diameter. In work [102], a beam combiner is used to merge light delivery and ultrasonic detection. The submicrometer can potentially be achieved by increasing the numerical aperture of optical lens although the soft-depth limit should be considered for optical focusing [103]. A penetration depth of 0.7 mm has been demonstrated and the axial resolution is estimated to be 15 μm, as defined by the transducer bandwidth of 100 MHz [102]. While the lateral resolution is improved by the optical focusing, the axial resolution is still limited by the bandwidth of the ultrasonic detector, yielding a highly asymmetric voxel. High axial resolution and a more symmetric voxel would be desired for 3-D high resolution imaging. The axial resolution is linearly dependent on the detector bandwidth. For example, an axial resolution of 1.5 μm would require a 1 GHz bandwidth detector. To use such high acoustic frequencies, the strong acoustic attenuation, degrading the imaging depth, should be considered. A 300 MHz acoustic wave is attenuated at a rate of ~20 dB/mm in water and ~80 dB/mm in tissue [102]. Thus, besides bandwidth, the ultra-high sensitivity is required to have applicable

imaging depth.

The optical ultrasonic detector, the polymer microring resonator, could potentially improve the axial resolution to several micrometers because it has potential to achieve GHz bandwidth. The approach makes a more symmetric voxel for photoacoustic microscopy. The noise level of microring ultrasonic detectors can be reduced by increasing the cavity Q factor. Experimental results have shown an ultra-high Q factor of 3×10^5 and a low noise-equivalent pressure of ~20 Pa over a 75 MHz bandwidth [24]. In fact, it is possible to achieve even lower noise with improved fabrication and/or design. The high sensitivity and high resolution in both lateral and axial enables single red blood cell detection, which can also be applied to some non-imaging sensing, such as flow cytometry. Next Chapter will show the flow speed measurement by photoacoustic methods.

4.2 Photoacoustic microscopy using microrings

Polymer microring resonators have very wideband response and can potential achieve GHz bandwidth. With the hope that microrings can provide high axial resolution in photoacoustic microscopy, enabling a more symmetric voxel, the pure optical photoacoustic microscopy (POPAM) is proposed and demonstrated. In POPAM, a thin film optical resonator is used to replace the piezoelectric acoustic receivers. The inherent broad band response of the optical thin film structure to acoustic waves, combined with rastering of a focused optical excitation beam can produce both axial resolution and lateral resolution comparable to that achieved in optical microscopy. The high resolution,

immunity to electromagnetic interference and good biocompatibility of POPAM open an opportunity to molecular imaging with less invasive and more convenient methodology.

POPAM, not only a novel receiver for PAM, but it also paves the way for exploration of imaging the contrast of optical absorbance on the micron and submicron scale. Even super resolution, breaking the limitations of diffraction, is possible in the future. To our knowledge, no work on POPAM has been published so far, though resonant optical structures such as etalons, fiber gratings and dielectric multilayer interference filters have been studied as ultrasound sensing elements for photoacoustic measurement or tomography [16, 104]. The photoacoustic signals are much weaker and involve much higher frequency components for micro- or submicro-scale objects, such as capillaries or components of individual red blood cells in the case of microscopy compared with the signals from large vasculatures on macro-scale for tomography. Achieving some of the potential of POPAM has been a challenge.

In this work, our proof-of-concept studies aim to construct a POPAM prototype and demonstrate its superior resolution capabilities. The preliminary results for imaging mouse bladder ex vivo and mouse ear in vivo suggest excellent performance of POPAM over conventional PAM.

4.2.1 Methods and results

The left panel in Figure 4.2 presents the schematic of an POPAM setup based on the highly sensitive broad bandwidth microring resonator. The resonator has ring-shaped form coupled with a straight waveguide serving as optical input and output. Such microring detectors have been shown to have an almost flat band response up to ~100

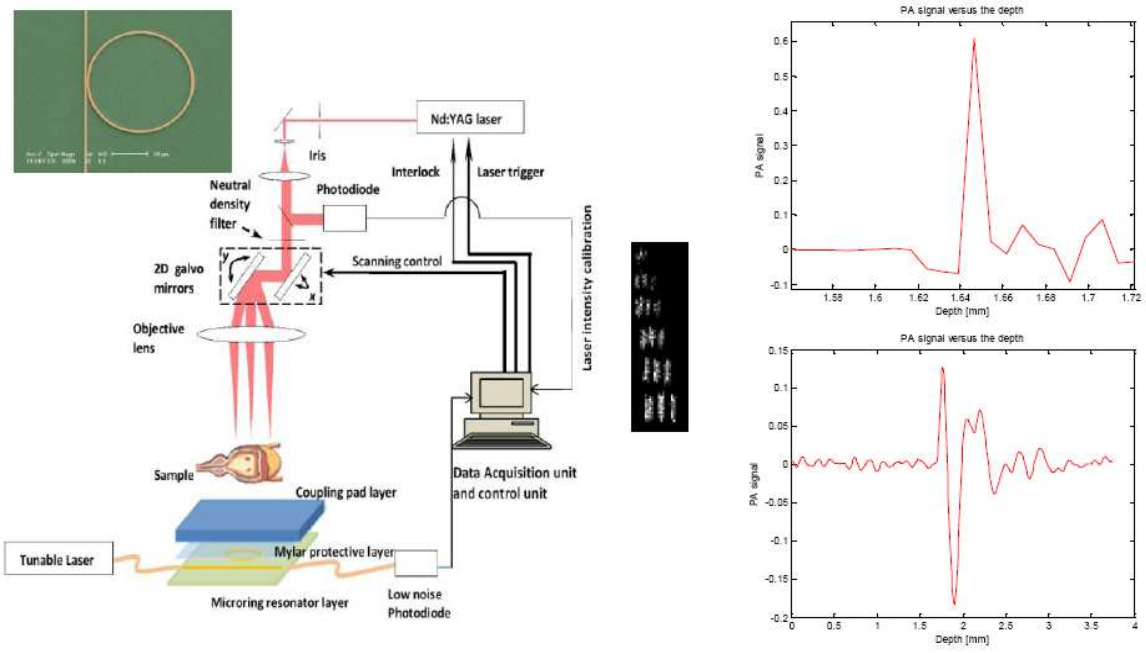

Figure 4.2 (left panel) schematic of a preliminary POPAM system based on a microring resonator. (middle panel) maximum amplitude projection (MAP) image of the USAF resolution template group 7. (right panels) A-line signals along the Z axis of the images of the USAF resolution template with POPAM (right upper panel) and conventional PAM with Onda transducer (right lower panel). The inset at upper left shows a scanning electron micrograph of a polystyrene microring with 30 μm radius used in this experiment.

MHz [19, 105]. The microring resonator fabricated on a silicon chip was covered by a Mylar protective layer to screen out the exciting laser beam from a Nd:YAG laser (Spot-10-200-532, Elforlight Ltd, UK). The Nd:YAG laser working at 532nm wavelength has a pulse duration of 2 ns and a repetition rate (PRR) of 1KHz. The laser light was spatially filtered by an iris and then expanded to a parallel beam which was rastered over the tissue object by 2-D Galvanometers. The intensity and the stability of the laser beam was monitored and calibrated by a photodiode (DET10A, Thorlabs, NJ). An achromatic lens with a focal length of 50 mm was used as the objective lens. On the Mylar protective layer, one coupling pad layer was used to optimize the coupling of the photoacoustic

signal from the sample into the microring resonator detector. A tunable laser (TLB-6312, New Focus, CA) provided the light source for the microring resonator at a wavelength tuned to the maximal slope of the resonance peak of the microring's transmission spectrum. A low noise photodiode (1801-FC, New Focus, CA) was used to record the change of the intensity of the light through the microring resonator which reflects the waveform of the photoacoustic signal. The photodetector has a DC output gain of 1 V/mA and AC output gain of 40 V/mA with nominal -6dB electrical bandwidth of 25kHz-125MHz. Using the DC output, the microring's transmission spectrum can be measured. Throughout the experiment, a commercial calibrated Onda transducer (HNC-1500, Onda, CA) with -10dB bandwidth of 300 kHz-20 MHz was utilized to realize conventional PAM as a control to evaluate the performance of the POPAM. The PAM with Onda transducer shared the same optical focusing and scanning components with POPAM. The Onda transducer operated on a reflection mode at a same distance from the target as the microring resonator working on a transmission mode.

Polymer microring devices were fabricated on a 4-μm-thick SiO_2 on a Si substrate using nanoimprinting technique [73]. With an improved technique in the mold fabrication and the design of operating wavelength around 780 nm where the absorption loss of polymer and surrounding water cladding is minimized, an ultra-high Q factor of 3.5×10^5 was achieved. The microrings used in this study have a size of 60 μm in diameter and the polymer waveguides have a cross section of 1.4×1.4 μm^2. A single-mode and a multi-mode optical fiber were aligned with the input and output of the straight waveguide, respectively, and then fixed using UV curable epoxy. Polymer microring device is favorable in POPAM because of its ultra-low noise and broad bandwidth [19, 22, 24]. A

much lower noise-equivalent pressure (NEP) compared with other types of optical resonant structures [104] has been demonstrated and further improvement of NEP is possible by designing much higher-Q device and/or by coupling more power into waveguides. From optical point of view, the detector's response time will be limited by the cavity's photon lifetime which is the time required for energy to decay to e^{-1} its original value and is given by $\tau = Q/\omega$ [106]. Inverse of the response time will give the cut-off frequency. So our current device's frequency response can be up to 6.7 GHz. From acoustic point of view, a maximum modulation frequency of 570 MHz can be estimated considering the 1.4-μm-thick PS waveguide and the acoustic impedance of the cladding, polymer, and the substrate [32]. If assuming strong acoustic reflections from the rigid substrate and negligible reflections from the cladding-polymer boundary, an approximated formula gives a quick estimation on the bandwidth limit:

$$| P_l(k) | = \frac{2 | \sin(kl) |}{kl} , \tag{4.1}$$

where P is the mean distribution of stress across the thickness l of the sensing film due to an normally incident plane acoustic wave with wave number k. The POPAM with microrings has the potential to achieve higher axial resolution if more broadband signals can be detected, which requires a photodetector with higher frequency response than used in the current experiment.

The lateral resolution of the POPAM was measured by imaging an USAF resolution template (T-20-P-TM, Applied Image Inc, NY). The middle panel in Figure 4.2 shows the maximum amplitude projection (MAP) image of the resolution template, where the 6 bar elements of the group 7 can be resolved with the gaps up to 2.19 μm with

modulation transfer function (MTF) value of 34%. Fitting the MTF to 50% yields a lateral resolution of 2.5 μm. The PAM with Onda transducer shows the same lateral resolution because they shares the same optical focusing and scanning architecture which determines the lateral resolution of the system. In tissue imaging, the lateral resolution will deteriorate mildly due to the optical scattering. However, when the sample is optically thin (i.e. within one mean free path), the deterioration of the lateral resolution is insignificant [102, 107]. To quantify the axial resolution, typical A-line signals extracted from the images of the USAF resolution template were used as approximations of axial point-spread-functions (PSFs). The right upper panel in Figure 4.2 depicts the axial PSF of POPAM; while the right lower panel in Figure 4.2 depicts the axial PSF of conventional PAM with Onda transducer. According to Rayleigh criterion, the PSFs show that this initial experiment of POPAM based on the microring resonator provided an axial resolution of 8 μm, close to the lateral optical resolution achieved; while PAM based on the Onda transducer gave a much larger axial resolution of 105 μm.

The bladder excised from CD1 mouse (CD1, Charles River, MA) was imaged ex vivo. The MAPs (Figure 4.3) of the images of the vasculature of the mouse bladder acquired with POPAM (upper row) and conventional PAM with Onda transducer (lower row) show the same views in the sample, since the POPAM and PAM shared the same optical scanning and the sample was not moved between scans. MAPS on the XY planes acquired with POPAM and PAM render a consistent structure of the bladder vasculature with same resolutions. The difference of the contrast distributions between them is due to the different positions of the microring resonator and onda transducer, one working in

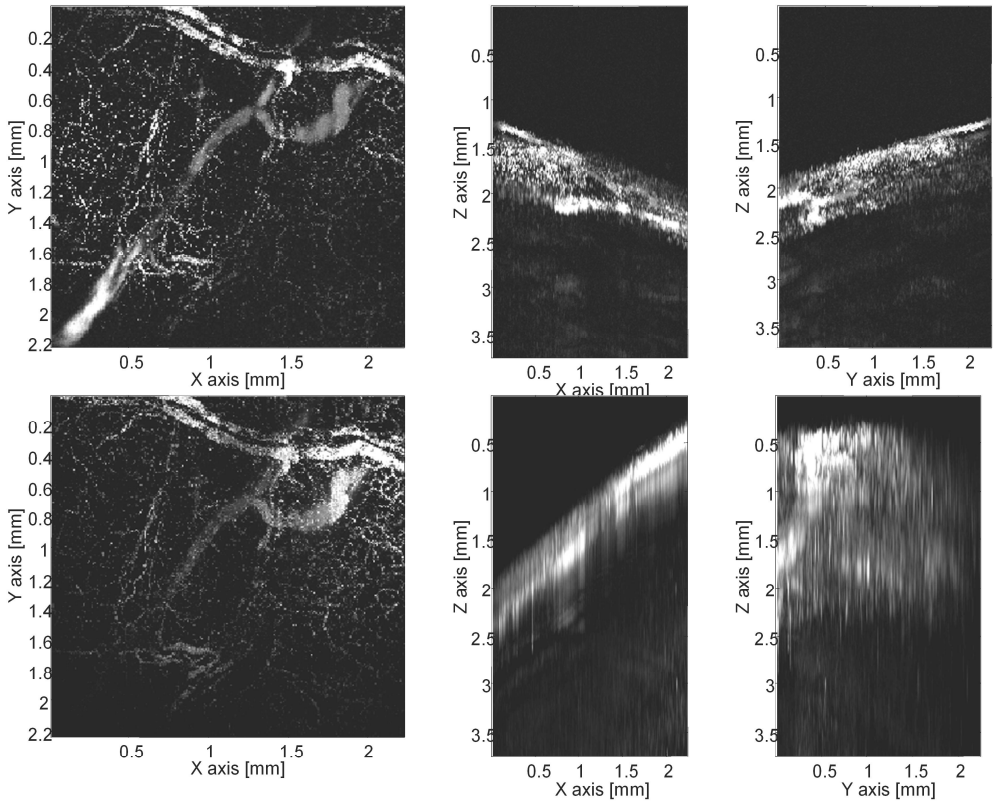

Figure 4.3 MAPs on XY,XZ, YZ planes of the ex vivo images of the vasculature in a mouse bladder wall acquired with POPAM (upper row) using microring and conventional PAM using Onda transducer (lower row).

transmission mode and another working in reflection mode. MAPS on the XZ and YZ planes acquired with PAM indicated a tail-trail from microscale vessels along the axial direction, initially thought to be due to the limited bandwidth of the Onda transducer. MAPS on the XZ and YZ plane acquired with POPAM indicated no tail-trail effect. The microscale capillary net with apparently large vasculature hiding in it can be clearly rendered. All the images in Figure 4.3 were acquired without averaging and proving maximum contrast to noise ratios of 26 dB for POPAM and 29 dB for PAM. The commercial Onda transducer has a high sensitivity providing noise equivalent detectable

pressure (NEDP) value of 19 Pa. The results of POPAM give an estimation of the sensitivity of microring resonator of NEDP value of 29 Pa, comparable with Onda transducer, much higher than other optical resonant structures available for acoustic measurement with NEDP on the order of magnitude of hundreds of Pascal.

The high sensitivity of microring resonator provides the POPAM the potential ability to detect the weak signal even from individual red blood cells. To verify this, we prepared a CD1 mouse bladder which was stored at 5°C for 48 hours after excision before imaging. The left upper panel in Figure 4.4 shows its photo and the left lower panel in Figure 4.4 shows its MAP image on XY plane with POPAM, indicating that individual blood cells can be discerned clearly by POPAM with a curvilinear alignment along a capillary. We have also verified the feasibility of POPAM for in vivo imaging of vasculature through the experiment on the ear of CD1 mouse with body weight 30g. The animal experiment has been approved by the UCUCA of the University of Michigan. Before imaging, 0.03 ml Ketaset with ketamine 100 mg/ml was injected to anesthetize the mouse and hairs on the ear were removed using hair-removing lotion. The photo and MAP image of mouse ear are shown in the right upper panel and right lower panel in Figure 4.4, respectively. The branching of vessels at different deep layers can be clearly observed. Some smallest vessels have diameters of ~5 μm and are on the capillary level. The interesting thing is that most of single capillaries imaged in the in vivo mouse ear present the continuous tubular structure different with the discrete distribution of individual red blood cells imaged in the ex vivo mouse bladder. It is probably due to the flowing of blood cells and high concentration of blood cells in the microvasculature in the case of in vivo imaging.

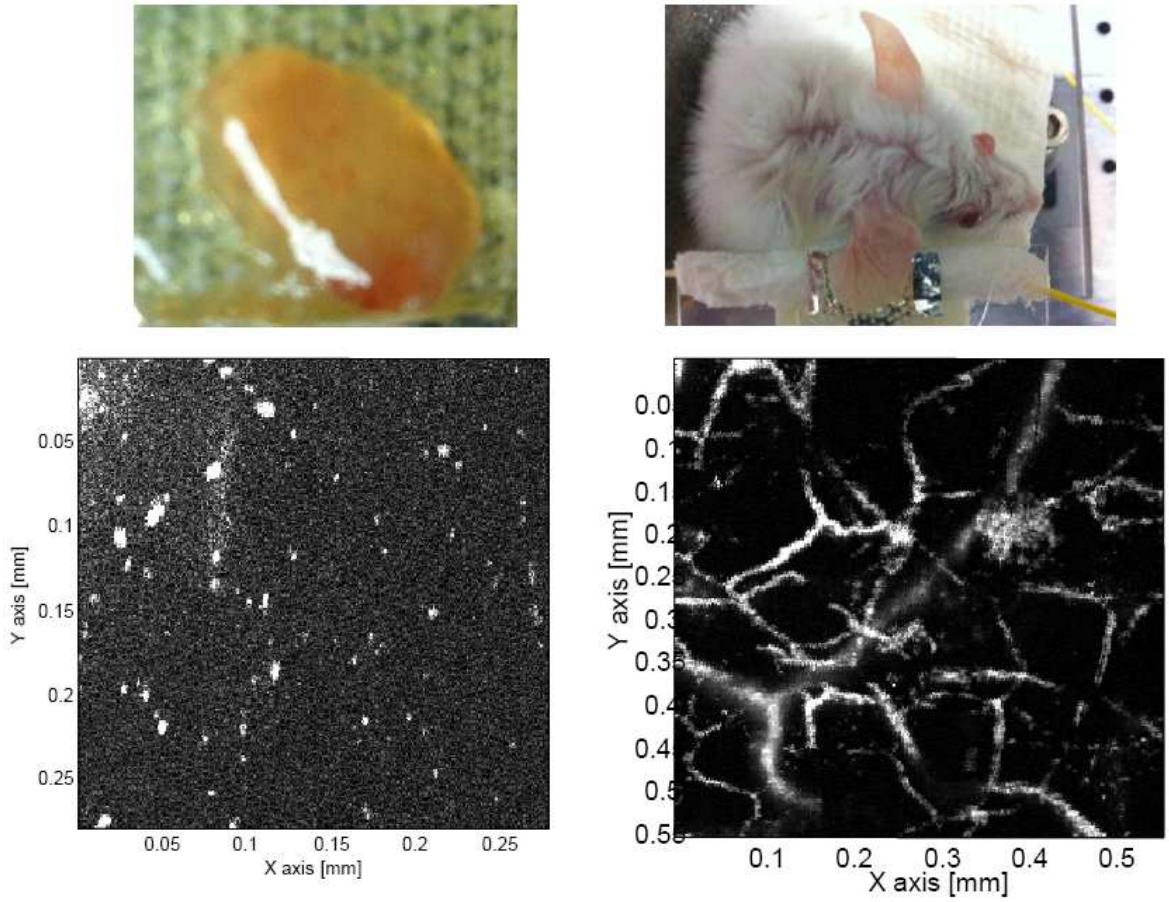

Figure 4.4 Photos of mouse bladder ex vivo (left upper panel) and mouse ear in vivo (right upper panel). MAPs on XY planes from POPAM imaging mouse bladder ex vivo (left lower panel) and POPAM imaging mouse ear in vivo (right lower panel).

4.2.2 Discussion and conclusion

Different from the PAM with a low resolution along the axial direction that is limited by the bandwidth of the conventional PZT detector, new POPAM was validated for the first time in this work for its excellent axial resolution by using the super broad bandwidth optical microring resonator. The microring resonator was designed with high Q value providing high sensitivity with a NEDP value of 29 Pa. The sensitivity could be

improved by further reducing sidewall roughness of the microring to achieve much higher Q value and with higher laser input power. The 3-D structure of microvasculatures, capillary nets and even individual red blood cells, has been discerned successfully in the proof-of-concept experiments on mouse bladders and ears. The current POPAM system facilitates a lateral resolution of 2.5 μm and an axial resolution of 8 μm. Taking into account the objective, lens we adopted for the POPAM has the numerical aperture (NA) of 0.51, its lateral resolution could be improved by changing the objective lens with larger NA. The achieved axial resolution of the current POPAM is still far from the theoretical potential of the microring resonator. With the increased bandwidth of the microring detector, the bandwidth of the low-noise photodiode detecting the optical signal from microring resonator will also need to be increased in order to obtain the better axial resolution.

POPAM can provide 3-D resolution comparable to optical microscopy but completely different contrast information sensitive to the vasculature, oxygen concentration distribution, etc. The miniaturized size of microring detector and the biocompatibility of pure optical photoacoustic microscopy open an opportunity to noninvasive endoscopic imaging of a variety of diseases. POPAM, as a compliment to existing modalities, may also contribute to in vivo molecular imaging by staging and characterizing angiogenesis of the cancer as well as monitoring cancer therapy. One of the potential applications is for bladder cancer which is the fourth most common cancer and the ninth most common cause of cancer death among men. In Figure 4.3, the preliminary results on mouse bladder have demonstrated the feasibility of POPAM to identify the vasculature structure of the bladder up to a depth of 0.7 mm at the accuracy

of microscale. The microring resonator has a size of 60 microns in diameter and is already fiber-connected. The small size of the microring detector and its fiber optical based design could significantly benefit endoscopic imaging of bladder cancer.

In addition to facilitating new imaging capabilities, POPAM could also guide and optimize the treatment of bladder cancer, for instance, with potential integrated optical angiogenesis therapy. Should this technique be validated, it will show very broad application in diagnosis and image guided treatment of a variety of other diseases, such as breathing disorders, chronic diarrhea, incontinence, internal bleeding, irritable bowel syndrome, stomach ulcers and urinary tract infections.

4.3 Design of co-axial reflection mode photoacoustic microscopy

The current setup of POPAM is in transmission mode. In fact, reflection mode is preferred because it is applicable to more anatomical sites than orthogonal or transmission mode. Thus, microrings fabricated on a transparent substrate are developed. Besides, the ring-shaped microrings can provide lateral resolution by utilizing the angle-dependent sensitivity. Figure 4.5 shows the schematic of co-axial reflection mode PAM. With a proper design of microring size, it is possible to have the high lateral resolution of several micrometers and has potential to achieve sub-micrometer scale. In this case, the optical focusing is not necessary although a weakly focused beam can be used to provide better sensitivity. For optical-resolution PAM [102], the laser should be strongly focused to obtain very high lateral resolution, which may sacrifice the imaging depth in biological

tissues due to soft-depth limit [103]. The co-axial reflection mode PAM using microrings may have potential to provide ultrahigh lateral and axial resolutions at moderate imaging depths for biomedical imaging.

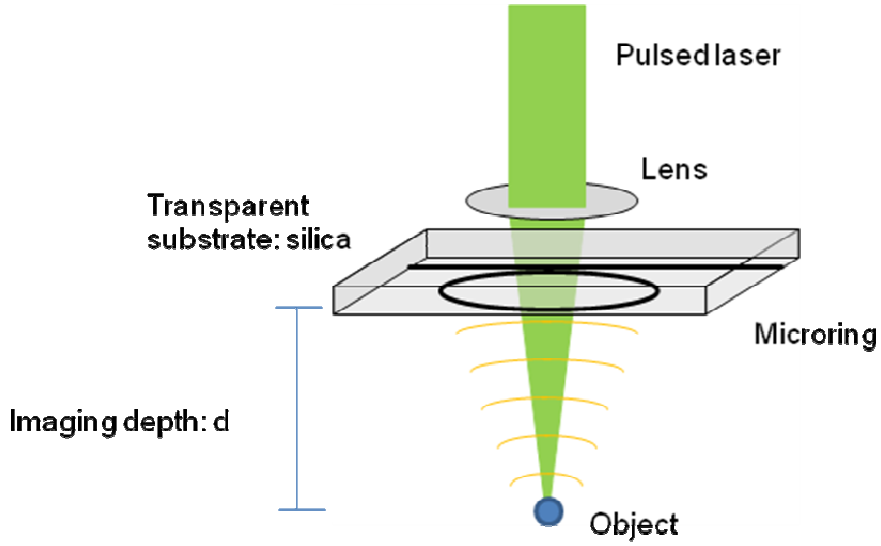

Figure 4.5 Ultasound arrived microring in phase, which enables the co-axial scheme of pulsed laser and ultrasound.

4.3.1 Fabrication of microrings on a transparent substrate

Previously, we fabricated the microring resonator on the substrate of silicon dioxide on silicon by nanoimprint technique [73]. To have the photoacoustic microscopy operated on a reflection mode, the microring resonator should be fabricated on a transparent substrate. Fused silica is used because its refractive index is similar to that of silicon dioxide. To access the input and output of optical bus waveguides of microrings by butt-coupling methods, we need to have good waveguide edges. However,

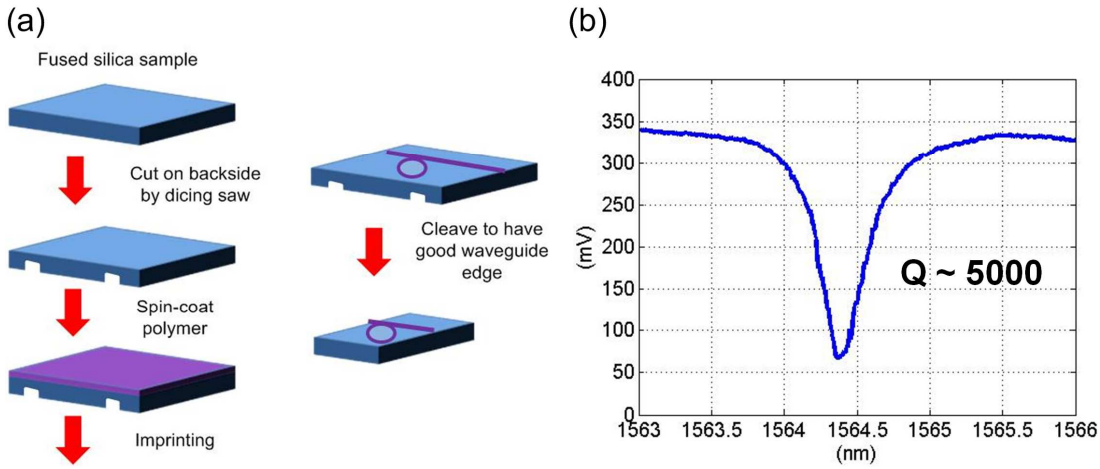

Figure 4.6 (a) Fabrication method of microring on fused silica (b) Measured transmission spectrum of microring on fused silica.

conventional cleaving used in silicon is very difficult to apply in fused silica. Thus, a different process for easy cleaving of microring on fused silica is developed. Figure 4.6(a) shows the schematic of the process flow. We first prepared a piece of fused silica with size slightly larger than that of the mold. Next, we used the dicing saw machine to produce two trenches on the backside of fused silica along the direction perpendicular to the bus waveguide which will be fabricated on the front side of fused silica later. We spin coated the polystyrene (PS) polymer. In order to have high quality factor of microring cavity, PS was chosen because of its high refractive index. For imprinting, the mold was aligned with the fused silica to have the microring between the two cut trenches and then a similar procedure of imprinting on silicon substrate was applied to produce the microring patterns. Finally, the sample was cleaved along the two trenches which are relatively fragile. The transmission spectrum of microring on fused silica measured in water surroundings is shown in Figure 4.6(b). The quality factor is around 5000, similar to that of PS microring imprinted by the same mold on silicon substrate

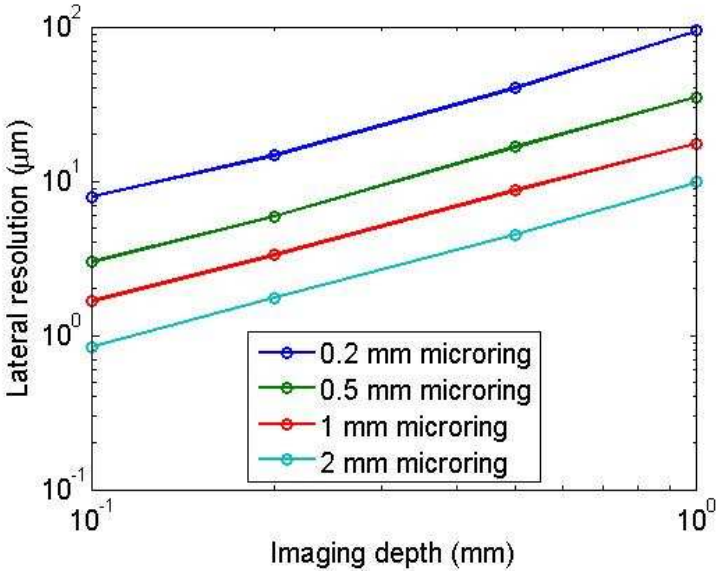

Figure 4.7 Simulations of lateral resolution provided by microring resonators.

[19]. This test shows the feasibility of microrings on a transparent substrate. In the future, we plan to try the fabrication using the mold which can produce ultra-high Q microring resonators and integrate the high-sensitivity microring with photoacoustic microscopy system to realize reflection mode PAM.

4.3.2 Estimation of lateral resolution

To evaluate the lateral resolutions provided by angle-dependent sensitivity of microrings, the simulation is performed. Here, we considered a 2-ns pulsed laser and 120 MHz bandwidth of the detection system, including the response of microrings and the bandwidth of photodetector. Water attenuation of 2.2×10^{-4} dB/mm-MHz^2 is also taken into consideration. Figure 4.7 shows the simulation results of lateral resolution at different imaging depths. Different sizes of microrings are considered. With a 2 mm microring resonator, the lateral resolution less than 10 μm can be achieved at depth of 1

mm; the submicrometer resolution is potentially possible at depth ~100 μm.

Chapter 5 Photoacoustic endoscopy

5.1 Introduction

Photoacoustic imaging is a noninvasive imaging method, which utilizes excitation from a pulsed laser energy source. Photoacoustic imaging has attracted considerable attention in recent years. Biomedical applications such as *in vivo* brain imaging and breast cancer diagnosis have been demonstrated [60, 87]. It is a promising modality for the study of functional and structural organization of biological tissue. However, to image internal organs, such as the wall of the stomach and esophagus, the imaging resolution can be degraded due to large depth. In fact, the photoacoustic endoscopy can be applied to circumvent the above issue by imaging from the inside of internal organs. Such imaging scheme enables exceptional imaging depth for target organs, providing great clinical values. For this reason, it is necessary to develop a probe for photoacoustic endoscopy imaging modality.

Endoscopic photoacoustic imaging has been developed and applied in recent years. The built probes have been used to image the inflammation in the atherosclerosis plaque [108], a rat abdominal surface [109], and colorectal cancer tissue [110]. In all these works, piezoelectric transducers were used. Wideband response of the detector is essential for high-resolution photoacoustic endoscopy. High sensitivity is required for *in*

vivo study. Small sizes of the probe will facilitate the clinical applications. However, the realization of such ideal probe using piezoelectric technology is limited due to finite bandwidth and degraded noise-equivalent pressure (NEP) in small transducer size. One way to avoid these issues is to use optical method for ultrasound detection.

Polymer microring resonators as a sensitive ultrasound sensor have been studied and utilized for some applications recently [16-24]. The advantages include immunity against electromagnetic interference, high acoustic bandwidth, potential for miniaturization [111], and sensitivity primarily dependent on the slope of optical spectrum rather than detector size. In this work, we have newly designed and fabricated a miniaturized imaging probe, including light excitation source and ultrasound detectors based on polymer microring resonators, for photoacoustic endoscopy applications. In the following section, we will describe the probe design and implementation. The resolution will be calibrated by performing B-scan images of a small carbon fiber. The technical discussion will also be given.

5.2 An integrated photoacoustic endoscopy probe

Figure 5.1(a) shows a schematic of our photoacoustic endoscopy probe, where an optical fiber for laser pulses delivery, a photoacoustic signal detector (polymer microring resonators with input/output fibers connected), and a light-guiding prism are integrated. External laser pulses delivered by an optical fiber are turned 90 degree after total internal reflection by an optical prism, and then emitted through the transparent fused silica substrate of the polymer microring resonator. The sent pulsed laser spots are positioned

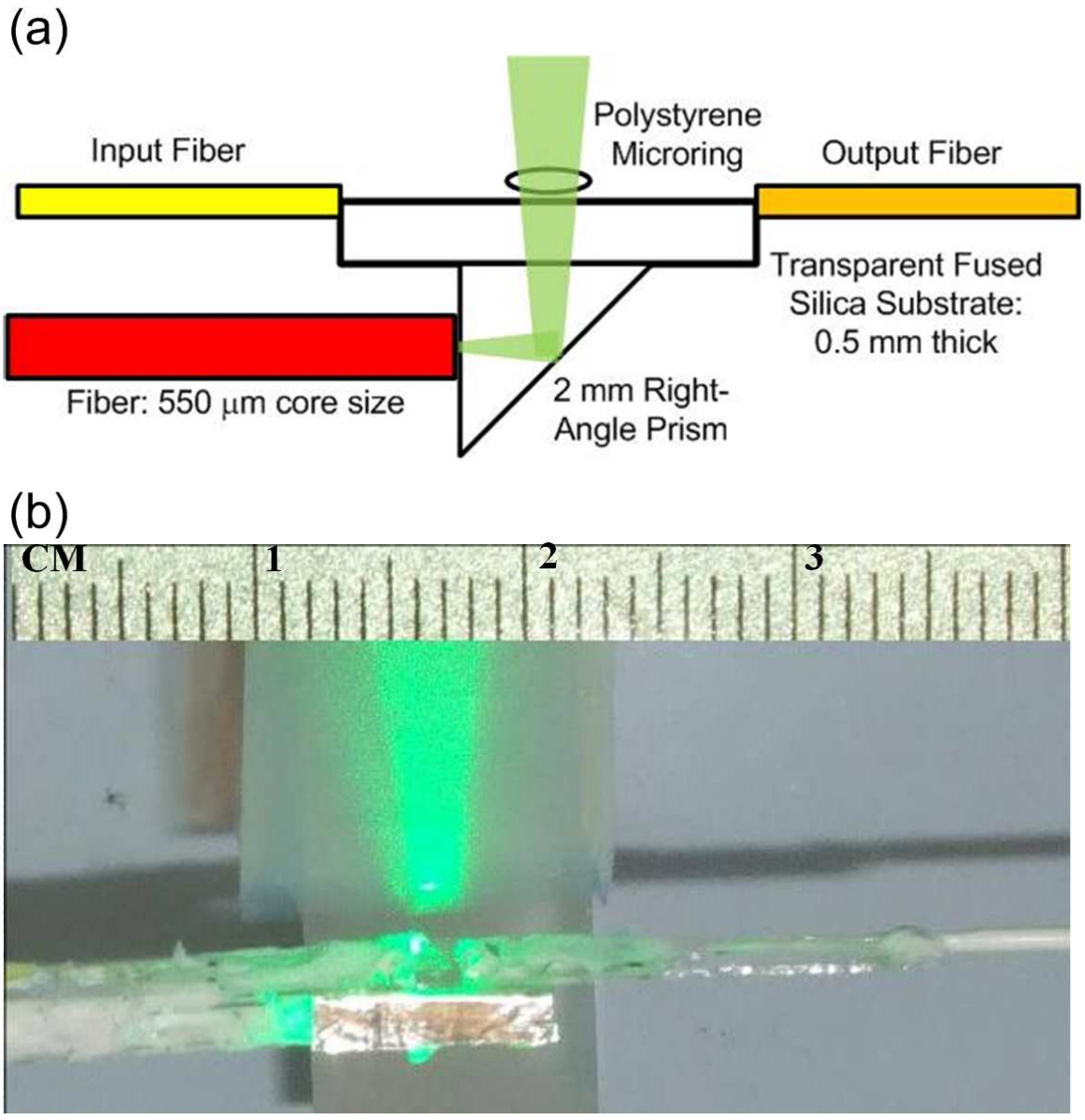

Figure 5.1 (a) Schematic of the photoacoustic endoscopy probe. (b) Picture of the fabricated probe with ~ 5 mm in diameter.

around the central part of microring. Finally, the laser pulses are absorbed by the target and generate photoacoustic waves by thermal expansion. The produced photoacoustic signals are detected by the polymer microring resonators on a reflection mode. The

spatial peak of laser pulses is roughly above the center of the microring. Hence, the microring can have the best response because the incoming photoacoustic waves impinge on the microring in phase. It is important to have the laser peak with the center of microring coaxially, especially for high-frequency signals in the high-resolution photoacoustic endoscopy.

Figure 5.1(b) presents the pictures of the assembled endoscopic probe, including an optical fiber and the microring resonator with connection of its input/output fibers. The probe has a maximal thickness of 5 mm, mainly from the diced piece size of fused silica. The rigid part has a total length of 35 mm and the flexible part is composed of optical fibers, including input/output fibers of microrings and the optical fiber for the laser pulses delivery. In section 4.3, we have introduced the fabrication process of microring resonators on transparent substrate. The microring device on fused silica used here mainly follows that process.

5.3 Calibration of photoacoustic endoscopy probe

The experimental setup shown in Figure 5.2 was used to calibrate the performance of the probe. A continuous-wave tunable laser source (HP 8168F, Agilent Technologies, Santa Clara, CA) was connected to the input fiber, and the output fiber was connected to a photodetector (1811-FC, New Focus, San Jose, CA), which has an electrical bandwidth of 25 kHz-125 MHz. The output of the photodetector was recorded by a digital oscilloscope (WaveSurfer 452, LeCroy, Chestnut Ridge, NY) with a

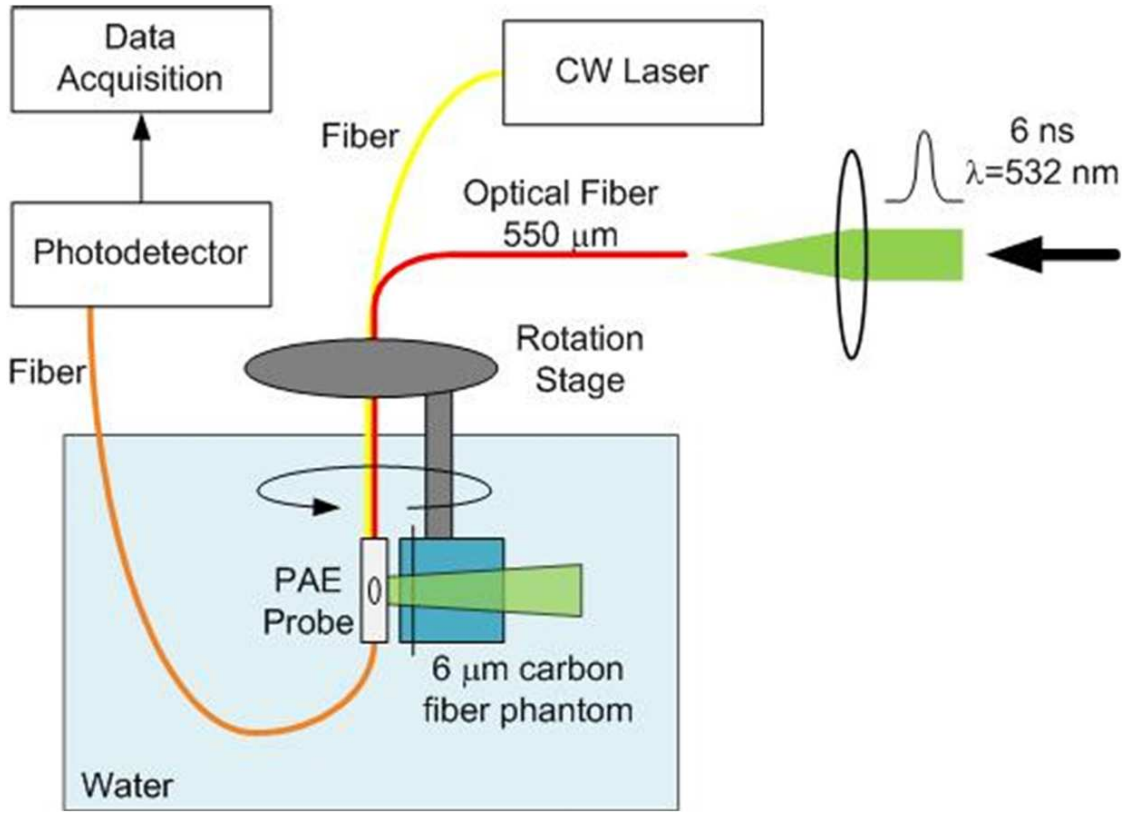

Figure 5.2 Experimental setup for the probe calibration.

sampling rate of 1 GHz. A 532 nm pulsed laser (Surelite I-20, Continuum, Santa Clara, CA) with a 6 ns pulse duration was focused by a lens and then coupled into an optical fiber with a core size of 550 μm. To demonstrate the high-resolution, a small phantom of 6 μm carbon fiber was fixed in a gel made by mixing water and 1% agarose (GPG/LE, American Bioanalytical, Natick, MA) and placed in deionized water. A circular scan around the integrated probe was realized by using a rotation stage. The integrated probe was positioned close to the rotation center. During the experiment, the objects scanned around the endoscopic probe at a radius of 6 mm with a step size of 0.5°.

The carbon fiber can be treated as a line target because the diameter of carbon fiber is shorter than the central acoustic wavelength of the microring detector system. The maximal detected time-domain photoacoustic signal of carbon fiber, usually when the phantom is right above the microring, is shown in Figure 5.3(a). From the time-domain signal, we estimate the carbon fiber is 2.7 mm from the probe edge. Figure 5.3(b) shows the spectrum of the signal in Figure 5.3(a). Very wideband signals of 13-64 MHz at -6dB was obtained and signals from DC to 120 MHz are still more than -20 dB. The signal-to-noise ratio (SNR), defined as the peak signal amplitude to the noise fluctuation (standard deviation), of the detected A-line signal was 22 dB after 32 times signals were averaged.

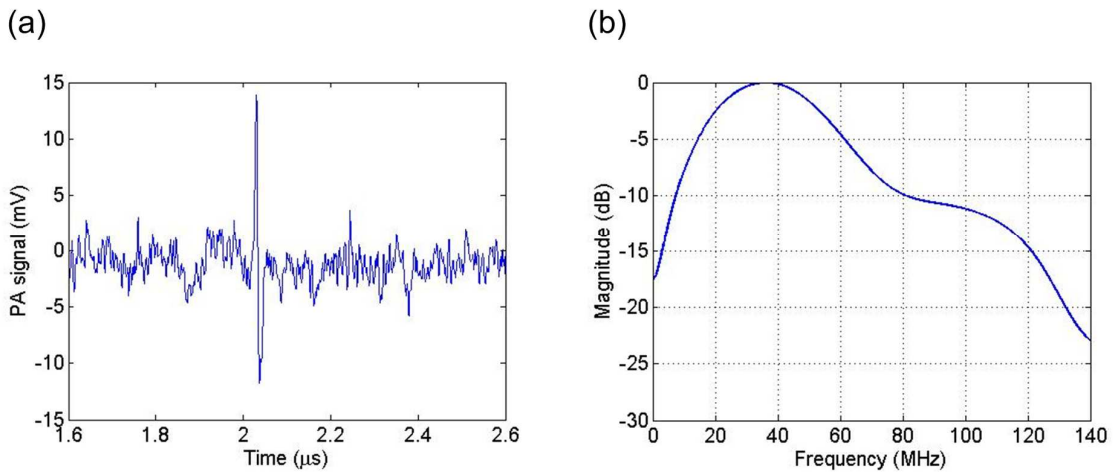

Figure 5.3 (a) Photoacoustic A-line of the carbon fiber. No filter was applied. SNR = 22 dB after 32 times signals were averaged. (b) Frequency spectrum of the signal in (a).

Hilbert transform (envelope) was applied to all detected A-line photoacoustic signals, which is typically used in B-scan ultrasound and photoacoustic imaging. From the envelope, we determined the radial resolution based on the -6 dB width from the

maximal A-line signal. The calibrated radial resolution was up to 21 μm, resulted from the wideband response of microring detectors. Figure 5.4(a) shows the transverse, or angular, point spread function (PSF) of the carbon fiber. The angular resolution is 7°. Considering a radius of 6 mm, the calibrated transverse resolution is around 750 μm. The photoacoustic B-scan images of the carbon fiber are plotted in Cartesian and polar coordinate formats in Figure 5.4(b) and (c), respectively.

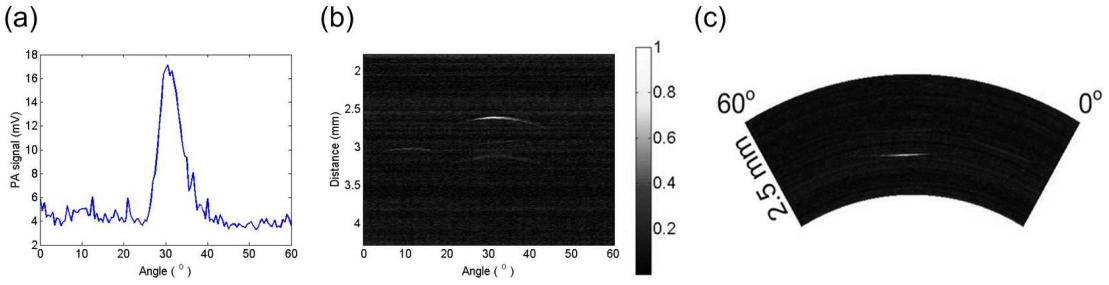

Figure 5.4 (a) Transverse point spread function for the carbon fiber (b) Photoacoustic image of a carbon fiber: Cartesian coordinate representation. (c) Polar-coordinate representation of image.

5.4 Discussion and conclusion

We compared the characteristics of our probe with those of other endoscopic probes fabricated by piezoelectric detectors, shown in Table 5.1. Our 5 mm probe size is similar to that in [109]. The fused silica piece can be diced smaller. A thin fused silica substrate can also be chosen. Small prisms or angle cleaved fibers can be used. Combined all these changes, the probe less than 2 mm is technically possible. Moreover, our probe

	Device size	Transverse resolution	Radial resolution
[108]	0.83 mm (light source is not integrated)	5.5 degree (~480 μm for 5 mm radius)	38 μm
[109]	4.2 mm	230 μm	52 μm
[110]	10 mm	2400 μm	320 μm
This work	5 mm	750 μm	21 μm

Table 5.1 Sizes and resolutions of endoscopic photoacoustic probes

has good radial resolution up to 21 μm, which is much better than the others. Currently, the poor transverse resolution of 750 μm is mainly due to the large laser spot. It can be improved using fibers with small core sizes. To facilitate the photoacoustic endoscopy probe for clinical applications and animal experiments, the input and output should be designed at the same side, which can be realized by changing the bus waveguide routing in mold fabrication. Our current device is able to perform B-scan images by rotating the phantoms, which can be applied in some *ex vivo* study. By designing the microring resonator with detection direction along the probe's longitudinal direction, a micro motor with a prism mirror can be used to guide pulsed laser and photoacoustic signals [109], enabling the capability to perform B-scan imaging *in situ* or *in vivo*.

We developed an endoscopic photoacoustic probe with the integration of an optical fiber and the microring ultrasonic detector. The B-scan photoacoustic endoscopy has been performed. The fabricated probe can achieve high radial resolution of 21 μm.

By changing the fiber with small core size, the transverse resolution can be improved. The probe based on microring resonators has potential for high-resolution photoacoustic endoscopy with a small size (less than 2 mm). With the design of microring detection direction along the fiber direction, we can further engineer the probe for *in vivo* applications. In the future, it will be of great interest to fabricate the probe based on microring to achieve high resolution in both radial and transverse direction, small device size without sacrificing sensitivity, and the capability to perform circular scan.

Chapter 6 Photoacoustic correlation spectroscopy

6.1 Introduction

Fluorescence correlation spectroscopy (FCS) is a powerful technique widely used in analytical chemistry and biological research [112]. In FCS, fluctuation of fluorescence intensity of a small number of fluorescent molecules is analyzed using temporal correlation. FCS has found a wide range of applications [113-114]. We propose a technology, photoacoustic correlation spectroscopy (PACS), by extending the fluorescence detection in FCS to the acoustic signal domain. The PACS is based on pulsed laser excitation. Autocorrelation is performed using measured photoacoustic (PA) signals, and the term "spectroscopy" refers to time-spectrum rather than in common usage as a frequency spectrum. PACS is different from other techniques using PA effects in correlation measurements, such as photoacoustic spectroscopy (PAS) [115] and correlation photoacoustic spectroscopy (CPAS) [116]. PAS was to analyze the absorbing chemical groups of samples from the measured IR spectrum. CPAS measures the cross correlation between excitation source and detected acoustic response. CPAS was mainly used to study static properties such as depth-profiling and thermal imaging. In contrast, the specific purpose of the PACS technique is to study functional dynamics of PA species.

The smallest of a body's blood vessels are capillaries, serving the exchange of

water, oxygen, carbon dioxide, and nutrients between blood cells and surrounding tissues. The flow speeds of red blood cells (RBCs) through capillary networks are affected by various factors such as metabolic demand and heart rate [117-118]. Analysis of capillary flow benefits disease diagnosis and treatment. For example, study of the alteration of retinal capillary flow velocity may help to identify patients at high risk for cerebrovascular diseases [119].

Current blood velocimeters such as Doppler-related techniques and optical/ultrasound particle image velocimetry employ the scattering properties of tracer particles to provide imaging contrast [120]. This dependence on scattering by tracers may limit the sensitivity, resolution, and detection depth due to a high optical scattering coefficient in tissue and much stronger ultrasonic reflection from tissue boundaries than ultrasonic scattering from tracer particles. Take Doppler techniques for example. Doppler ultrasound method is not easy to detect the flow speed less than 1 mm/s [121]. Doppler optical coherence tomography has difficulties in flow measurement at depth greater than 1 mm [122]. The above methods have limitations in measuring flow speeds in capillaries at sufficient depths, up to ~5 mm. One way to overcome these limitations is using PA signals from the RBCs excited by a pulsed laser, which circumvents the diffusive light scattering in tissues [123]. Recently, PA blood flow speed measurements have received growing attention [123–126].

In this work, we first conduct a phantom experiment on flow measurement to demonstrate the feasibility of PACS technique. The PACS flowmetry for assessment of microvascular blood flow has several advantages. (1) It provides a label-free measurement because the high optical contrast between RBCs and the surrounding tissues

[127]. (2) Low scattering of sound signals enables high imaging depth. (3) Wide range flow speeds can be measured by properly designed temporal resolution and probe beam size. (4) Photoacoustic microscopy (PAM) scheme can be used to provide high spatial resolution [102], providing the ability to measure blood flow speeds in capillaries. The PACS technique for *in vivo* blood flow speed measurement in capillaries in a chick embryo model is also demonstrated.

6.2 Theory of PACS

Light-absorbing beads generate PA waves when they absorb laser energy and undergo an instantaneous thermal expansion. In PACS, we name the counterpart of fluorescence intensity in FCS as PACS strength. It can be expressed as

$$P(t) \equiv \int I(r)n(r,t)d^3r\,, \tag{6.1}$$

where $I(r)$ is the normalized spatial fluence distribution of the laser beam, and $n(r,t)$ is the bead concentration at position r and time t. The laser beam used in our PACS setup defines the probe volume. When the beads move in and out of the volume, the number of beads present in this volume, denoted as $n_{in}(t)$, fluctuates. Because PA pressure amplitude is not directly proportional to PACS strength $P(t)$, the information of $P(t)$ needs to be extracted by proper signal processing from the measured PA signals. In our flow measurement configuration, a one-dimensional (1-D) step excitation profile was used. Thus, $I(x) = 1$ at $|x| \leq w/2$ and $I(x) = 0$ otherwise, where w is a width of the probe laser beam. The temporal autocorrelation of $P(t)$ provides information about the average duration and strength of the fluctuations [128]. Specifically, the decay profile of the

autocorrelation function (ACF) $G(\tau)$ reveals the beads' dwell time in the probe volume. The magnitude of $G(0)$ is related to the number density of the beads in the probe region. The normalized ACF can be calculated as

$$G(\tau) = < \delta P(t)\delta P(t+\tau) > / < P(t) >^2, \tag{6.2}$$

where $\delta P(t) = P(t) - <P(t)>$ is the fluctuation of $P(t)$ and $< >$ denotes ensemble average.

6.3 Low-speed flow measurement

We choose a flow experiment because it is easy to obtain a range of dwell time. Analysis of flow for a step laser profile has been studied [129]. With a flow speed V of the beads, the ACF takes the following form:

$$G(\tau)/G(0) = \begin{cases} 1-\tau/\tau_0, & \text{for } \tau \le \tau_0 \\ 0, & \text{for } \tau > \tau_0 \end{cases}, \tag{6.3}$$

where $\tau_0 = w/V$. Here, the diffusion of the beads due to Brownian motion is neglected, which is a reasonable assumption considering the long diffusion time, $\frac{w^2}{16} \cdot \frac{6\pi\eta a}{k_B T} \approx 8 \times 10^6$ sec [130-131], where the Boltzmann constant $k_B = 1.38 \times 10^{-23}$ J/K, the temperature T = 300 K, the viscosity coefficient $\eta = 10^{-3}$ Pa·s, the bead radius $a = 24.5$ μm, and probe beam size $w = 1.1$ mm.

The experimental setup is shown in Figure 6.1. A 532 nm pulsed laser (Surelite I-20, Continuum, Santa Clara, CA) generating 6-ns pulses with a 20 Hz repetition rate was used as the probing light source. The laser beam (fluence ~70 mJ/cm^2) illuminated the flow sample (49 μm diameter black polystyrene (PS) beads in water) with a beam width

of 1.1 mm. A microring resonator was used to detect the PA signals. Assuming the probe volume is around the origin, the detector was positioned in the x-z plane, (x,0,z), as shown in Figure 6.1. The photodetector output was fed to an oscilloscope (WaveSurfer 432, LeCroy, Chestnut Ridge, NY). Beads were flowing in a tubing (inner diameter: 0.8 mm) driven by a syringe pump. Flow rates were calibrated from 200 to 14 μm/s using a microscope.

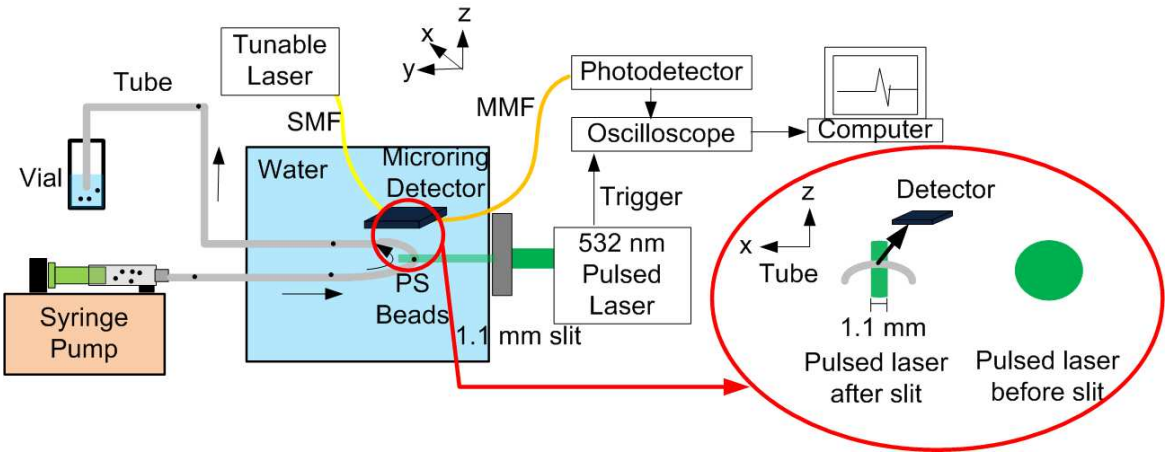

Figure 6.1 Experimental setup for PACS flow measurement. SMF, MMF, and PS stand for single-mode fiber, multi-mode fiber, and polystyrene beads, respectively. Beads flow in the x-direction. The PA signals were detected by using a microring resonator positioned in the x-z plane. The shape of the pulsed laser before and after a slit is illustrated.

Figure 6.2(a)-(c) shows the measured PA signals from the PS beads at a calibrated flow speed of 33 μm/s. Figure 6.2(a) and (b) show the temporal PA waveform taken at a particular elapsed time before and after applying a low-pass filter (cutoff frequency: 50 MHz). The complete PA signals collected are shown in Figure 6.2(c). As time elapses, temporal PA signals appear from 5.75 to 5.95 μs. Thus, we can determine that the 1-D

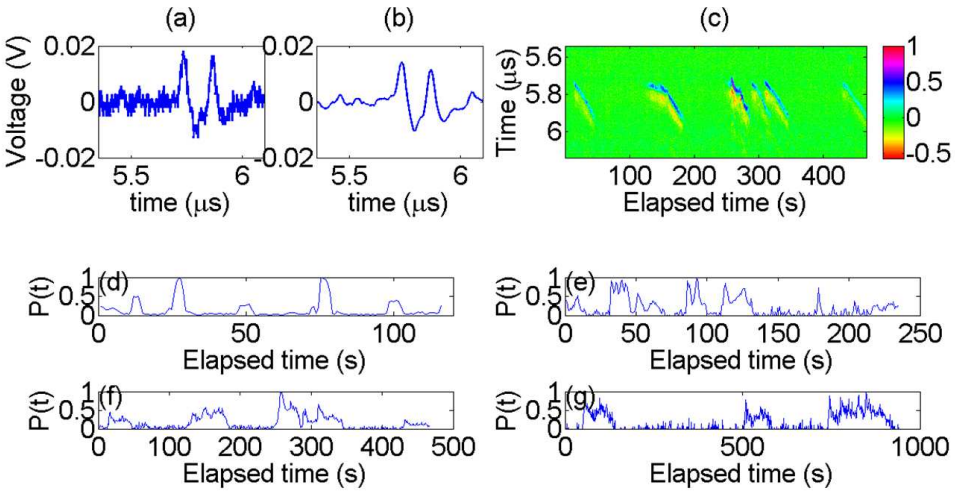

Figure 6.2 (a) Detected raw PA signals at a calibrated flow speed of 33 μm/s and at elapsed time = 309.1 s. (b) Signals after filtering. (c) Detected PA signals as a function of elapsed time, measured at the calibrated speed of 33 μm/s. The average distance from the beads to the detector was ~8.5 mm. (d)-(g) PACS strength fluctuation as a function of elapsed time. PACS strengths in (d)-(g) correspond to calibrated speeds of 200, 90, 33, and 14 μm/s, respectively.

flow direction is away from the detector. For measuring three-dimensional (3-D) flow vectors, line scan FCS [132] can be applied to PACS. Figure 6.2(d)-(g) show the PACS strength $P(t)$ for four calibrated speeds. It was extracted using collected temporal PA data to within a constant scaling factor by taking the root-mean-square value of the measured PA signals, which is suitable for a low-concentration solution. Due to a finite time duration needed for each data transmission from the oscilloscope to a computer, the available temporal resolution of our current PACS system is 0.8 sec, meaning one sample of $P(t)$ per 0.8 sec. Noise in $P(t)$ estimate was offset to zero for more accurate estimation of $G(0)$ [130]. Figure 6.2(d)-(g) show that the beads dwell time becomes longer as the speed decreases. Different noise level in $P(t)$ is due to different devices' sensitivity. The

signal-to-noise ratio (SNR) of the filtered PA signals in the four cases was estimated as 35, 26, 29, and 22 dB.

The PACS curves are shown in Figure 6.3(a). The dotted points are autocorrelation curves calculated from Equation (6.2). The solid curves are the fits using Equation (6.3). The dwell times, τ_0, obtained from PACS curves were 4.42−74.1 s. The measured flow speeds calculated from the relation $V = w/\tau_0$ were 249−14.9 μm/s. In Figure 6.3(b), the dotted points are the speeds by PACS measurement and the solid line represents results from direct measurement, which shows excellent agreement between the two. Discrepancy in the case of faster flow speed might be due to limited fitting points.

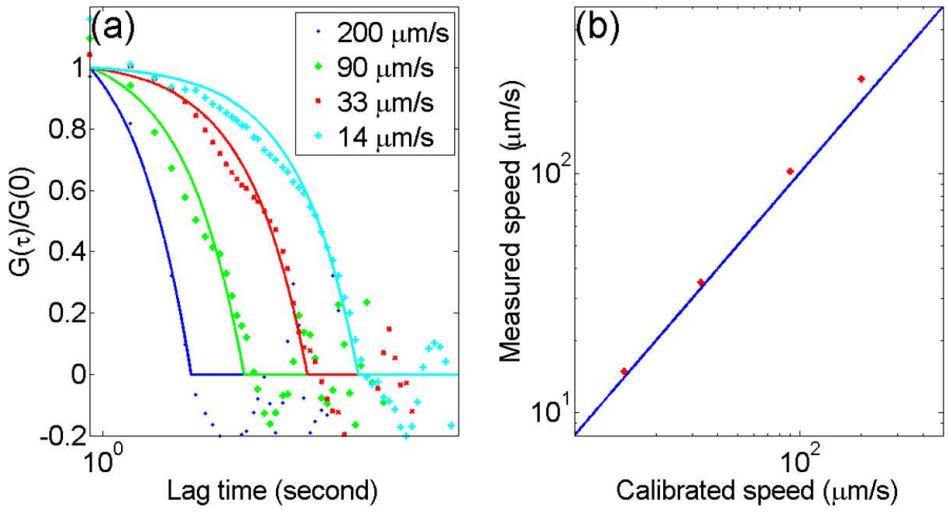

Figure 6.3 (a) PACS curves of designed flow speeds of 200, 90, 33, and 14 μm/s. The solid curves are the corresponding fits. (b) The measured flow speeds by the PACS technique, shown in stars, versus the calibrated flow speeds. The solid line represents the results from direct measurement.

The extracted average bead number $\langle n_{in} \rangle$ were 0.53. Accordingly, the concentration can be estimated as 0.96 mm^{-3} [= $0.53/(1.1\times\pi\times(0.8/2)^2)$], which is a little different from the designed concentration, ~0.69 mm^{-3}. The former could have been overestimated because the nonuniform spatial fluence distribution of laser can result in a less-than-1 volume contrast [130, 133], and thus an underestimated probe volume. Longer measurement time and lower noise are helpful to determine the concentration more accurately. To measure a higher concentration in PACS, either a better detection scheme to distinguish $n_{in}(t) >> 1$ or a small probe volume can be used. In the former case, a detector array enables imaging capability. In the latter case, the temporal resolution of a PACS system should also be improved according to the relation $\tau_0 = w/V$. Otherwise, the maximum measurable flow speed would be limited. As V increases, the flow time τ_0 decreases and eventually approaches the limit of system's temporal resolution. A small probe volume also expands the minimum measurable V, which has no theoretical limitation in PACS flowmetry, by preventing prohibitively long time for measurement. Combining the two methods, PACS techniques can be further engineered for clinical applications.

To show the potential of PACS to study microcirculation at significant depth, we analyze a case of photoacoustic detection of a RBC. Assuming the effective noise-equivalent pressure (NEP) of a microring detector array is 2 Pa over 1-80 MHz and a 7 μm RBC, the imaging depth is estimated as 4.6 mm by using an analysis similar to that in [19] with parameters: μ_{eff}^{blood} = 50 cm^{-1}, μ_{eff}^{tissue} = 1 cm^{-1}, J_0 = 20 mJ/cm^2, and A = 20 dB/cm. In comparison, FCS for blood flow is limited by the optical transport mean free

path, ~1 mm in human skin. The spatial resolution of the probe volume can be several micrometers [102]. So it is feasible to use PACS technique to study randomly oriented networks of small microvessels. Our analysis shows that PACS has potential to study microcirculation with low flow speed in small capillaries. The high sensitivity and wideband properties of the microring detectors [19-24] enable deep imaging depth and high spatial resolution.

6.4 In vivo flow speed measurement

PACS uses the endogenous light-absorbing tracer particles, RBCs, which can absorb light 100 times more than the background if no other absorbers are within the excitation volume. In the previous work, a pulsed laser without focusing was used, which limited the spatial resolution and sensitivity. Besides, the range of measurable flow speeds was restricted due to low pulse repetition rate. In the current work, we use laser-scanning PAM [107, 134] to meet the demanding requirements for speed measurement in capillaries, which, for the first time, facilitated study on biological samples *in vivo*.

In the laser-scanning optical-resolution PAM system, the ultrasonic detector was kept stationary while the laser was raster scanned by an *x*-*y* galvanometer scanner. We used a Nd:YAG laser (Spot-10-200-532, Elforlight Ltd, UK) working at 532 nm wavelength with a pulse duration of 2 ns. A highly sensitive custom-built needle hydrophone with a center frequency of 35 MHz and a –6 dB bandwidth of 100% was used for ultrasonic detection and was aligned to the scanned region of laser light. For

flow speed measurement, the laser light was positioned and stayed at a designated point on a capillary by controlling the galvanometer fixed at a corresponding angle.

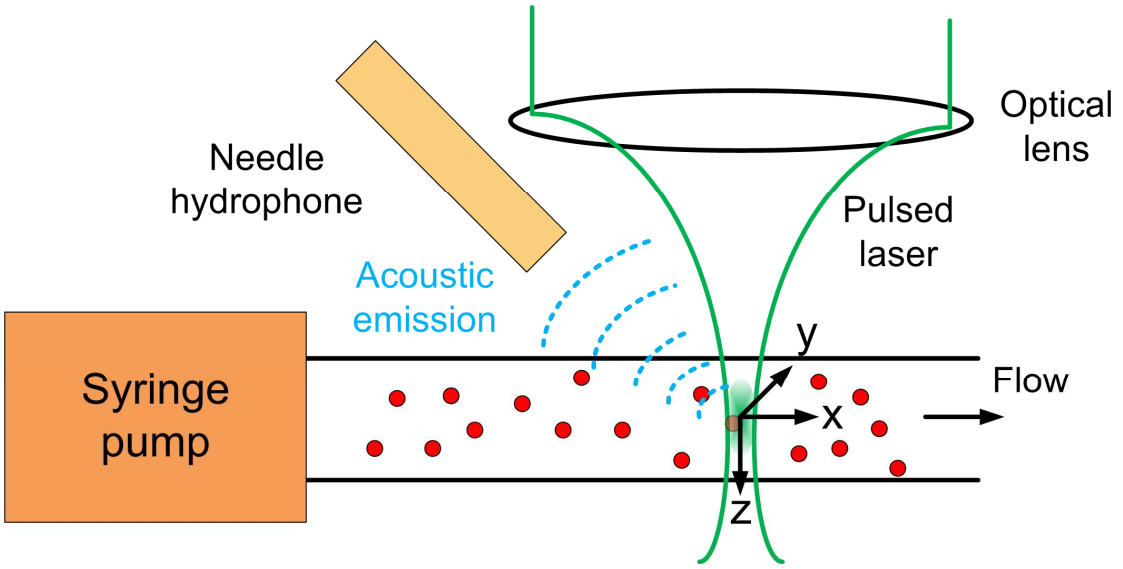

Figure 6.4 Schematic of PACS flow speed measurement using PAM system.

Since a focused laser beam was used, we did a phantom experiment to calibrate the probe beam size. Let's review the PACS theory and introduce the formula which is suitable for the case of a focused laser beam. In PACS, PACS strength, $P(t)$, is used, which is defined in Equation (6.1). As shown in Figure 6.4, when the light-absorbing particles pass through the illuminated volume, PA signals are generated. Because the PA signal A-line is not exactly the same as $P(t)$, the information of $P(t)$ should be extracted from the measured PA signals. Because of the small probe volume from the tight optical focus in the PAM system, the average particle number in the probe volume, N, is small, equal or less than 1. It is appropriate as a simple start, therefore, to use the peak-to-peak PA signal amplitude as $P(t)$, avoiding integration of noise. The calculation of the normalized ACF, $G(\tau)$, from the $P(t)$ fluctuation has been described in Equation (6.2).

The decay profile of the $G(\tau)$ reveals the particles' dwell time in the probe volume and the magnitude of $G(0)$ is related to the number density of the beads in the probe region [128].

Considering that the focused laser light has a Gaussian distribution in all directions: $I(x,y,z) = I_0 \exp(-2x^2/r_0^2 - 2y^2/r_0^2 - 2z^2/z_0^2)$, where I_0 is the peak intensity, $x(y)$ and z are radial and axial position of the laser beam, and r_0 and z_0 are the radial and axial radii. The Gaussian form in deriving the ACF in flow speed measurement has been studied in FCS [135]. The PACS concept follows from FCS and thus we can simply apply the formula in PACS velocimeter. At the flow speed V_f of tracer particles, the ACF can be expressed as

$$G(\tau) = 1/N \times \exp-\left(\tau/\tau_f\right)^2, \tag{6.4}$$

where $\tau_f = r_0/V_f$ and $N = 1/G(0)$.

The PACS probe volume using the PAM setup was calibrated by a phantom experiment with known flow speeds, designed from 0.51 to 3.64 mm/s, and particles concentration of $\phi = 0.2\%$. The suspended red dyed polybeads (mean diameter: 6.0 μm; Polysciences, Inc.) dispersed in distilled water were used. Beads were flowing, driven by a syringe pump, in a tubing (Inner Diameter: 250 μm, TSP250350, Polymicro Technologies, Phoenix, AZ). We first studied the dependence of the autocorrelation decay curves on the flow speeds. Figure 6.5(a) plots the flow time, τ_f, calculated from the fitted autocorrelation curves, versus the designed flow speeds. The flow time becomes shorter as the speed increases. As for extracting τ_f, we acquired the sequential A-line PA

signals (repetition rate 2048 Hz for 2 seconds) and the fluctuation of $P(t)$. One example at V_f = 1.9 mm/s is plotted in Figure 6.5(b). Then, the ACFs were calculated and fitted using Equation (6.1), as shown in Figure 6.5(c). To analyze our data properly, the mean and standard deviation of τ_f are obtained from at least 4 reliable measurements (the

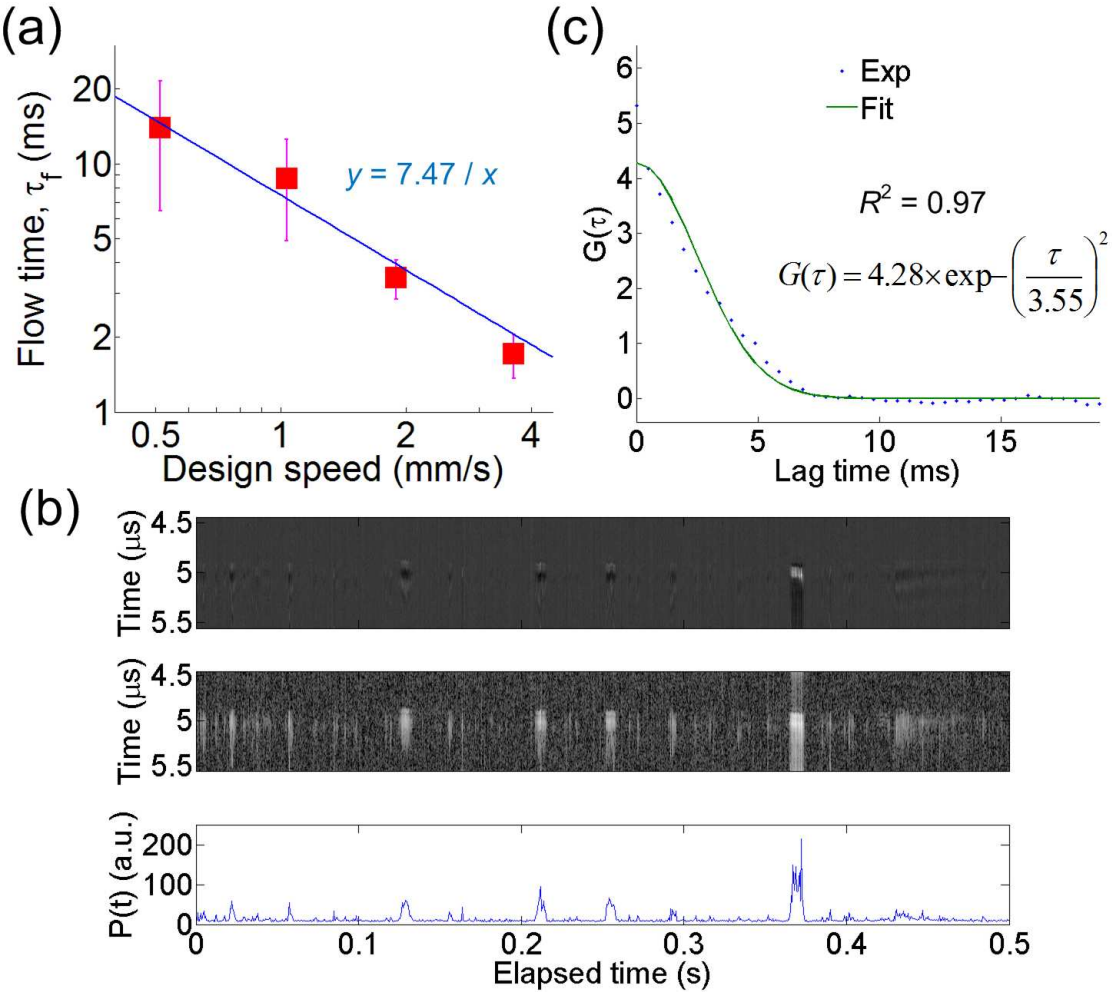

Figure 6.5 The dependence of the flow time on the design flow speed. The square symbols and the error bars represent the mean flow time and the standard deviations, respectively. The solid line is the curve fitting. (b) The A-line signals (Top), its Hilbert transform displayed over a 50-dB dynamic range for better contrast (Middle), and the $P(t)$ (Bottom). Only the first 0.5 sec is plotted. (c) Calculated and fitted autocorrelation curves in dotted and solid lines, respectively.

coefficient of determination R^2 in the fitting being larger than 0.9) at each flow speed. It is assumed that the small R^2 may result from the fact that both one and more-than-one beads are passing through the probe volume during one measurement, which may cause erroneous estimation of τ_f. Large variations in τ_f at slower speeds might be due to less chance for beads passing through the probe volume in each measurement compared to that in the high speed case.

To obtain the probe radial beam radius, Figure 6.5(a) is fitted using $\tau_f = r_0/V_f$. The extracted r_0 is 7.47 μm. For axial beam radius, the average value and standard deviation of $G(0)$ from all valid measurements is 7.18±1.87, and thus $N = 0.14$. Note that in ACF calculation, the noise in the $P(t)$ estimate was offset to zero for more accurate estimation of $G(0)$ [130]. The noise in $P(t)$ after zero-baseline processing results in underestimation of τ_f and N, which can be alleviated by improving signal-to-noise ratio. With known sample concentration ϕ, calculated N, and calibrated r_0, the z_0 can be estimated as 33.7 μm using $\phi = (N \times V_{\text{bead}})/V_{\text{probe}}$, where V_{bead} is the volume of one bead and the probe volume $V_{\text{probe}} = 4/3 \times \pi r_0^2 z_0$. Compared to a Gaussian beam calculation, the z_0 is smaller, which could be due to a limited directivity of the hydrophone. In the flow measurement, the Brownian motion can be neglected because flow time τ_f is much shorter than the diffusion time due to Brownian motion, ~several minutes, obtained by a similar analysis in section 6.3.

An *in vivo* experiment was performed on an 8-day-old chick embryo, as shown in Figure 6.6(a). The 8-day- old check embryo was used for its mature capillaries [136]. An *ex-ovo* chick embryo culture method [137] was used for easy experiments. To maintain

the life of chick embryo, an infrared lamp was used as a heating resource during the experiment. The membrane around the center of the embryo was first imaged by the PAM system. From the acquired PA image, the positions of capillaries can be recognized.

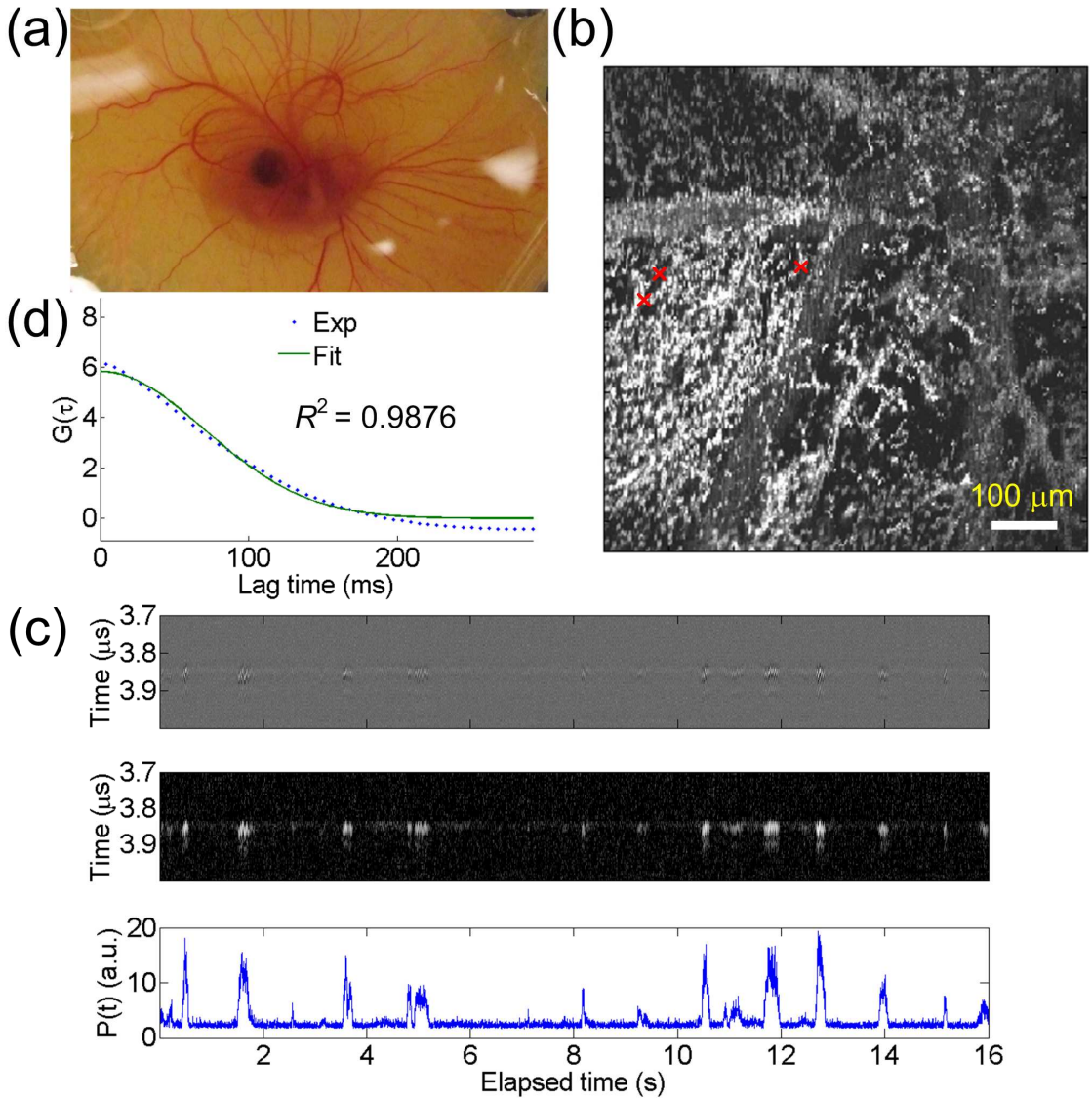

Figure 6.6 Photograph of an 8-day-old chick embryo. (b) The maximum amplitude projection image on x-y plane of the chick embryo. Red crosses: three different positions for flow speed evaluation. (c) The A-line signals (Top), its Hilbert transform displayed over a 25-dB dynamic range (Middle), and the $P(t)$ (Bottom). (d) Calculated and fitted autocorrelation curves in dotted and solid lines, respectively. The fitted τ_f = 99 ms.

Then, the scanner was positioned so that the probe beam stayed on targeted capillaries for PACS flow speed measurements. The 8192 sequential A scans were obtained at a repetition rate of 512 Hz for 16 seconds. For the statistical analysis, six reliable measurements were used. The data was acquired 40~80 min after the embryo was removed from the incubator. Since RBCs must deform to enter the capillaries, the RBCs length in the capillaries was considered as 16 μm [138] and thus an effective radial beam radius of 10.5 [= $(7.47^2–(6/2)^2+(16/2)^2)^{0.5}$] μm [139] was used for speed calculation. The PACS measured flow time is 53±28 ms. Thus, the calculated flow speed using the effective beam radius is 199 μm/s [~= (10.5 μm) / (53 ms)], which is close to those reported in the literatures [136, 138]. The results confirmed that the PACS velocimeter is plausible. Note that without the assumption of RBCs deformation, the calculated speed is 141 μm/s, which is slightly slower but is still reasonable considering the widely ranged flow speeds in capillaries [140]. Verification of RBCs deformation is under investigation.

To evaluate the variations of capillary blood flow speeds at different capillary positions, the same embryo was used for measurements. Similarly, we first took the PA image. The maximum amplitude projection image was shown in Figure 6.6(b). Three different positions, marked by crosses in Figure 6.6(b), were chosen for evaluation. One measured sequential A-line PA signal and its $P(t)$ was shown in Figure 6.6(c). The ACFs were shown in Figure 6.6(d). The measured flow times are 177±70, 188±37, and 136±53 ms, which are averages from at least four valid measurements for each point. The corresponding flow speeds are 59, 56, and 77 μm/s. Results show that the variation of

flow speeds in different capillaries is not obvious. Mildly reduced speeds may be due to the fact that the data was taken ~150 min after removal of the embryo from the incubator, mainly because of the time used for realignment of optical focus for different imaging area. The temperature control by the infrared lamp may not be uniform. Thus, as time elapsed, flow speeds could decrease due to changes of physiologic parameters such as blood pressure.

6.5 Summary

In summary, a photoacoustic correlation technique for low-speed flow measurement has been developed. We have demonstrated that the PACS technique can accurately measure the bead flow speed as slow as 14.9 μm/s. The technique has abilities to discriminate flow direction and to measure the concentration of solution. PACS for *in vivo* flow measurement of capillaries in an 8-day-old chick embryo has also been demonstrated. We calibrated the probe beam size in the PAM system by a blood-mimicking fluid. PACS is suitable for measuring the capillaries blood speed, which might be unattainable by other PA flow speed measurement methods. Combing with the unique ability of laser-scanning PAM in 3-D mapping of microvasculature, PACS provides a promising tool to monitor the disease process. We are also interested in exploring other applications by PACS.

Chapter 7 Photoacoustic detection of terahertz

7.1 Introduction

Terahertz (THz) electromagnetic (EM) waves, the frequency interval from 0.1 to 10 THz, is a scientifically rich frequency band since THz waves have unique value for imaging, chemical identification, and characterization of electronic and vibrational properties of materials. The low photon energies of THz radiation, e.g.: 4 meV @ 1 THz, is biologically safe, making it attractive for biomedicine application. The advances in THz technology rely on THz sources and detectors. Small and easy to operate THz sources and detectors can make THz technology more accessible in real-life applications.

Some existing schemes for sensitive generation and detection are mostly lab based. Much effort has been devoted for developing miniaturized THz sources, such as quantum cascade lasers [141] and photomixers [142], but less effort has been dedicated to THz detectors. Si-bolometers provide high sensitivity but the convenience is highly restricted by the low temperature requirement. Commercially available pyroelectric detectors are commonly used for THz sensing. However, a low-frequency modulation is required, limiting real-time THz detection. Some other detectors originally developed for other spectral bands are often used for THz detection but suffer from much less efficient detection of THz radiation.

Photoacoustic (PA) imaging has been extensively implemented in biomedicine with image contrast provided by optical absorbers, such as hemoglobin and melanoma [2-3]. Since several materials such as water can absorb THz waves, the PA method can serve as a new approach to THz detection. In this work, we explore the potential of the PA approach for detecting THz radiation. We briefly introduce the design considerations needed to optimize detection sensitivity. Characterization of the PA-based THz detector is demonstrated. We also conduct THz imaging of an aluminum foil. The low-cost PA technique can significantly benefit THz sensing systems.

7.2 Principle of photoacoustic detection

As previously discussed, the PA waves are generated when a sample absorbs EM radiation. The EM energy causes a temperature rise, resulting in local volume expansion by the thermal elastic mechanism. The consequent thermal expansion produces a pressure pulse that propagates and can then be detected by ultrasonic hydrophones. Upon illumination by a short laser pulse, the amplitude of the initial pressure is described by $P \propto \Gamma \mu_a F$ assuming that all laser energy is converted into heat [143], where $\Gamma = \kappa\beta / \rho C_p$, κ is the bulk modulus, β is the thermal coefficient of volume expansion, ρ is the mass density, C_p is the specific heat capacity, μ_a is the optical absorption coefficient, and F is the optical fluence. The Γ is determined by the absorber and is spectrally independent, while the absorption coefficient is usually spectrally dependent. With a fixed spot size and constant pulse width, the THz power at a certain wavelength is

proportional to optical fluence, and thus to the initial pressure P considering the same sample used, serving the THz detection mechanism by PA effect. To enable broadband detection over the entire THz range, the sample with high absorption over the spectral bands of interest is desired.

Although it is known that THz radiation can be effectively absorbed by water, the converted PA signals would be weak due to the high specific heat capacity and the moderate coefficient of thermal expansion of water. Previously, we demonstrated carbon nanotube (CNT)-polymer composites, comprising CNTs embedded in elastomeric polymer, for efficient generation of PA pressure under the excitation of pulsed laser light at visible wavelength [105]. CNTs are known for efficient conversion of absorbed light into thermal energy [144] because of their high absorption and low specific heat. Moreover, the elastomeric polymer, polydimethylsiloxane (PDMS), has been used as an acoustic transfer medium, aided by its large thermal expansion coefficient [145]. Separately, it has been shown that CNTs are able to achieve extremely high absorption in a wide wavelength range, from visible wavelengths to 200 μm [146]. Thus, the CNT-PDMS composite is attractive absorber for PA detection of THz. Note that PDMS has power absorption of ~10 cm^{-1}, and the absorption does not contribute to efficient photoacoustic generation [147]. Fortunately, we can optimize the photoacoustic conversion by making densely distributed CNTs in thin PDMS films. For example, a low absorption of 3.2% can be achieved for a 25 μm-thick PDMS film at 0.5 THz radiation [147]. To our knowledge, the PA effect with illumination at THz wavelength has never been exploited.

Multi-walled CNTs were grown on a fused silica substrate. Thereafter, the PDMS was poured to infiltrate the CNTs. Before curing, the composite was pressed with a fluorosilane-treated slide glass and a 25 μm-thick spacer was placed in between the substrate and the slide glass to roughly control the film thickness. After curing, the composite was carefully torn off as a free-standing thin film, in order to avoid either THz reflection/absorption or ultrasound attenuation due to the substrate. The process resulted in a thin film with dense CNTs, enabling low acoustic attenuation and high THz absorption, maximizing the detected PA peak pressure. A scanning electron microscope image of the cross-sectional view of the CNT-PDMS composite is shown in right lower part in Figure 7.1.

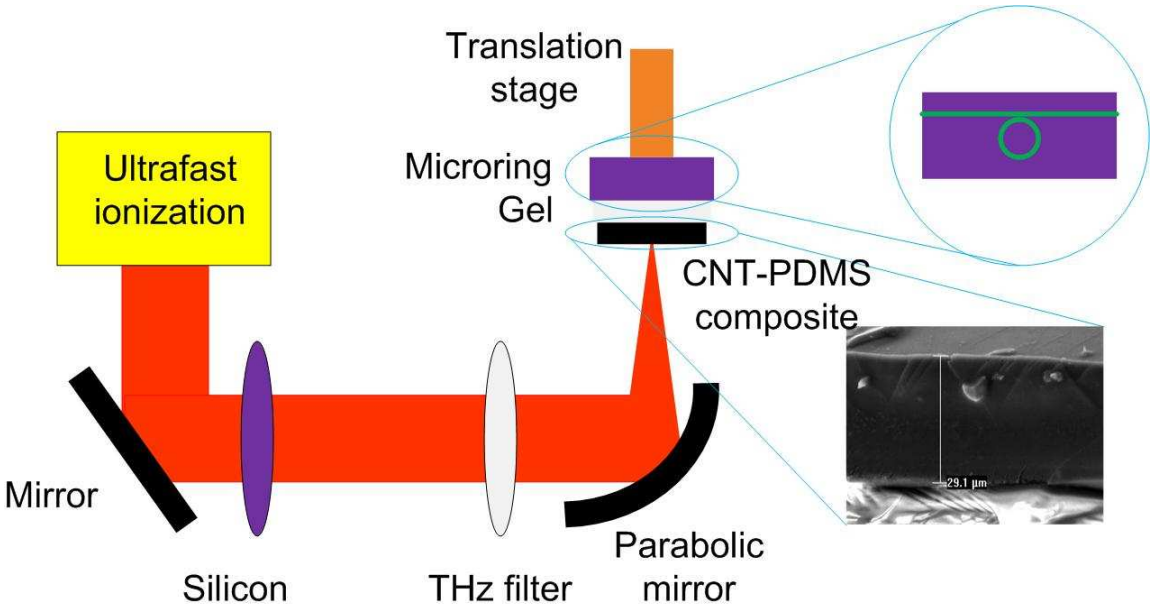

Figure 7.1 Schematic of experimental setup.

7.3 Experimental results and discussion

We placed the composite on a highly sensitive microring ultrasonic hydrophone. The working principles and the systems of microring ultrasonic detectors can be found in our previous publications [19, 22, 24]. The gel was put between the composite and detector to enable ultrasound coupling. A schematic of the experimental setup is shown in Figure 7.1. A two-color air ionization scheme, requiring a femtosecond laser with mJ-energy pulses [148-149], is used to generate a broadband radiation covering THz to mid-infrared. A silicon wafer was used to remove the short wavelengths of the femtosecond laser while a low-pass filter (LPF 10.9, Tydex, Peterburg, Russia) was added to obtain pulses with frequencies less than 6 THz at –6 dB and with cutting frequencies at ~11 THz. The THz radiation is focused by a parabolic metal mirror (f = 5.08 cm). The PA-based THz detector, including the absorber and microring resonator, was mounted on a three-dimensional translation stage and aligned at the focus of the THz radiation. The PA signals were recorded by a digital oscilloscope (WaveSurfer 452, LeCroy, Chestnut Ridge, New York) with a sampling rate of 1 GHz.

We used a microring ultrasonic detector (diameter: 90 μm) [22]. The device's transmission spectrum is shown in Figure 7.2(a). In this measurement, the THz beam was focused to a size of about 0.8 mm. The illuminated THz power was calibrated with a pyroelectric detector (THZ5I-MT-BNC, Gentec-EO, Quebec, QC, Canada) and a lock-in amplifier. Its sensitivity from the manufacturer is 70 kV/W. The detected average PA signals were recorded. Figure 7.2(b) shows the time-domain signals at the calibrated average THz power of 7 μW. Considering a 500 Hz pulse repetition rate, the laser energy

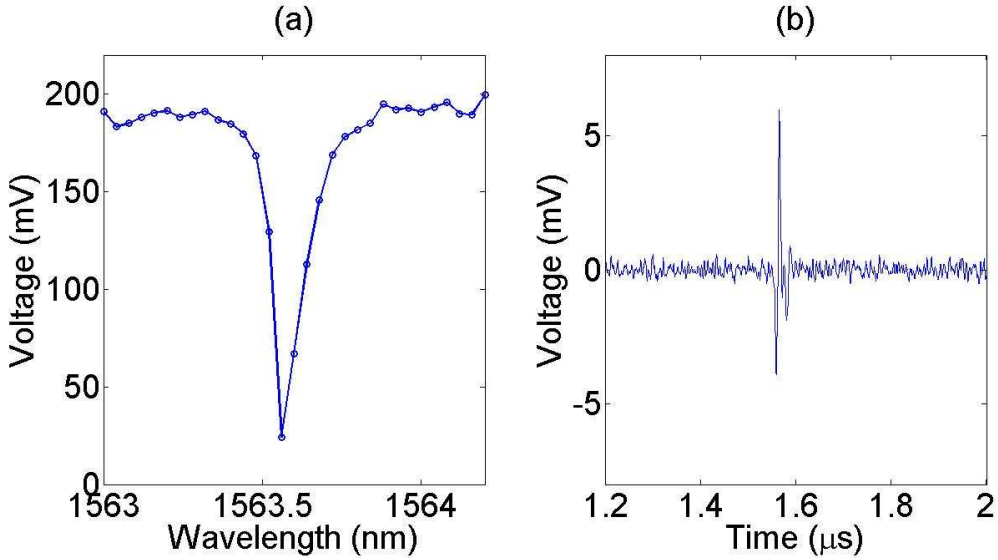

Figure 7.2 (a) Optical transmission spectrum of a polymer microring resonator. (b) The time-domain photoacoustic signal excited by THz pulses.

and fluence of one pulse are 14 nJ and 2.8 μJ/cm^2 [=(14 nJ)/(π(0.8/2)^2 mm^2)], respectively. The measured peak-to-peak voltage is 9.9 mV, corresponding to a sensitivity of 1.4 mV/μW. We also demonstrated the real-time detection of one THz pulse. Figure 7.3 shows the time-domain PA signal excited by one THz pulse without

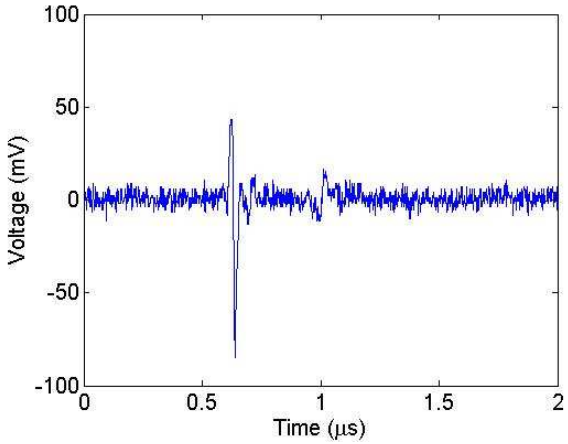

Figure 7.3 The time-domain photoacoustic signal excited by one THz pulse.

signal averaging. With known sound speed of gel (~ 1500 m/s), a 0.9 mm distance between the CNT-PDMS composite and the microring can be obtained. The detector response time is limited by a combination of the time required to generate a photoacoustic signal, the time for the ensuing propagation, and the detected acoustic impulse response. In our current setup, the propagation time dominates, resulting a ~0.6 μs response time, which can be enhanced further by putting the CNT-PDMS composite closer to the microring. Such real-time detection is difficult by the pyroelectric detector because it usually operates at low frequency (several to tens of Hz) and then takes a long time for the following lock-in amplifier gets stabilized (several to tens of seconds) to acquire the power value.

The THz detector by photoacoustic method has also been used for imaging demonstration. A photograph of the sample, an aluminum foil with cut out patterns attached on a visually transparent tape, is shown in Figure 7.4(a). As shown in Figure 7.4(b), the samples were mounted on a x-z stage and scanned through the position slightly prior to focus generated by a parabolic mirror with f = 5.08 cm focal length. Figure 7.4(c) shows the measurement by photoacoustic detection, where as Figure 7.4(d) is a reference image taken with the pyroelectric detector. Both methods are able to clearly image the aluminum pattern. In Figure 7.4 (c), the sensitivity is slightly decreasing from left to right due to changing sensitivity of microring detectors. The resonance wavelength of microring is also sensitive to environmental change, such as temperature variation. Thus, the sensitivity changes for a fixed operation wavelength. Fortunately, the issue can be easily solved by tuning wavelength to similar slope in transmission spectrum, e.g.: similar sensitivity, during imaging acquisition. In Figure 7.4(d), a slightly lower THz

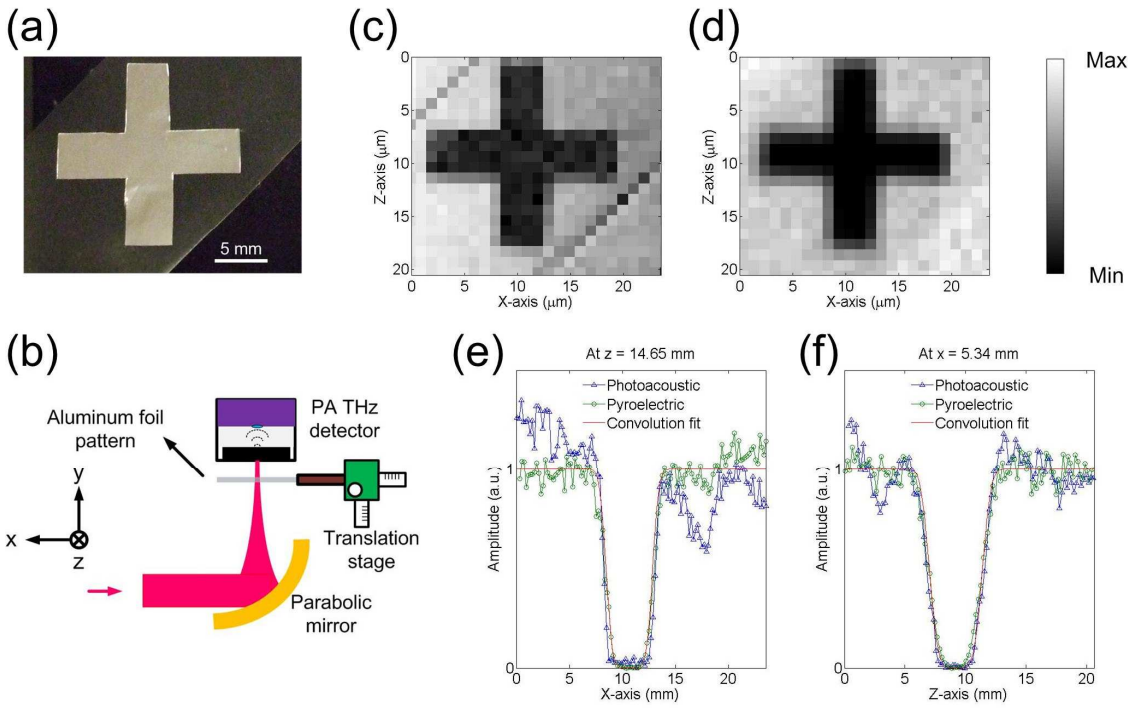

Figure 7.4 (a) A photograph of a sample of aluminum foil. (b) Schematic of experimental setup for THz imaging. Scanned images: (c) taken with the PA THz detector, (d) taken with the pyroelectric detector. One-dimensional images: (e) taken along x direction, (f) taken along z direction.

transmission through the tape than that through the air can be observed in the image. One interesting finding is that photoacoustic detection measured lower signals on the boundary of the tape and the air, while pyroelectric detection does not. This might be because THz beam scattered on the boundary, resulting in lower energy density. Photoacoustic method detects fluence (spatial energy density), while the pyroelectric detector measures the power inside its aperture. In this case, the pyroelectric detector has an aperture of 5 mm, which is larger than the THz beam size, as will be described below. Thus, it can still detect the scattered power. The exact reason is under investigation. The resolution for both images is restricted by the step size for the scanning and is 1 mm in

each direction. Figure 7.4(e) and (f) shows the THz image in one dimension with a resolution of 0.2 mm in each direction. It can be clearly seen that the two methods have good agreement. For quantitative analysis, we perform a convolution of a THz Gaussian beam and a THz transmission function, produced by the aluminum sample, to fit the one-dimensional images. The width of THz transmission function is measured as 4.5 and 4.4 mm along x and z, respectively. By the convolution fits, we can extract the THz beam size are 1.9 and 2.2 mm in x and z direction, respectively. Beam size is defined at the point where the intensity equals e^{-2} times the peak intensity. Note that one pixel by the pyroelectric detector with lock-in amplifier takes several to tens of seconds. The proposed photoacoustic detection has potential for real-time pulsed THz imaging.

7.4 Summary

To conclude, we used the photoacoustic effect for THz sensing. Using a CNT-PDMS composite as a photoacoustic absorber combined with the on-chip microring hydrophone, a small-size THz detector can be realized. The sensitivity of PA-based THz detector was calibrated. We also showed its ability for real-time detection, which is challenging by the pyroelectric detector. The application to THz imaging is also demonstrated. The THz detector using photoacoustic technique offers unique advantages such as room temperature operation, small size, on-chip design for easy integration, rf immunity, low manufacturing cost, and μs detection, which could be beneficial in various THz applications. Further improvement of sensitivity would be possible by reduction of

specular reflection of the CNT-PDMS sample [150], increasing the Q-factor of the microring resonator, making the composite as a form of acoustic lens [21].

Chapter 8 Conclusions and future work

8.1 Conclusions

The goal of this work is to explore exciting photoacoustic (PA) applications by taking advantage of microring ultrasonic sensors. Previously, piezoelectric detectors are commonly used in most photoacoustic applications. The state of the art piezoelectric detectors have several limitations. First, the detection sensitivity depends on element size. Thus, the element size is usually larger than 2 mm to achieve reasonable signal-to-noise ratio (SNR). Second, the large element size results in narrow acceptance angles. Third, the narrow bandwidth, from 60% to 150%, degrades the performances in photoacoustic imaging and detection.

The thesis presents a series of photoacoustic imaging and detection using optical microring resonators. Each application utilizes different advantages of microring resonators to provide outstanding performance. The characteristics of each application are summarized in Table 8.1. Chapter summaries with key contributions are also described below:

Applications	Utilized advantages of microrings	Enhanced performance by microrings
PAT	(1) High sensitivity; (2) Wideband; (3) Wide directivity	(1) Multi-scale imaging; (2) High resolutions over a large region of interest
PAM	(1) High sensitivity; (2) Wideband	(1) High imaging depth; (2) High axial resolution
PACS	High sensitivity	Ability to detect signals from single cells
PAE	(1) High sensitivity; (2) Miniaturized size	(1) High imaging depth; (2) Suitable for imaging internal organs
PA for THz	High sensitivity	Sensitive detection

Table 8.1 The characteristics of each application using microring ultrasonic sensors.

In **Chapter 2**, several unique merits of microring ultrasonic sensors have been calibrated. In our latest generation of microring resonators with diameter of 60 μm, the noise-equivalent pressure (NEP) was about 21.4 Pa over 1 MHz to 75 MHz. The measured detection bandwidth was over 90 MHz at –3 dB. For a 60 μm element size, the detection angle was calibrated as +/− 40° at –6 dB for a 20 MHz acoustic signal. As a comparison, a 75 μm piezoelectric polyvinylidene fluoride hydrophone (HPM075/1, Precision Acoustics, Dorchester, Dorset, United Kingdom) has an NEP around 6 kPa over a 100 MHz bandwidth considering only the noise from its matched preamplifier (HP1, Precision Acoustics). With similar detection bandwidth and element size,

microring resonators are much more sensitive, which is favorable for in vivo photoacoustic applications.

The main contributions of this work are:

1. Experimental calibration of microring's sensitivity and low NEP, 21.4 Pa over 1 MHz to 75 MHz.
2. Experimental calibration of microring's wideband response, over 90 MHz at –3 dB.
3. Experimental calibration of microring's angular response, +/− 40° at –6 dB for a 20 MHz acoustic signal for a 60 μm microring.

In **Chapter 3**, we have performed photoacoustic tomography (PAT) imaging experiments using microring resonators. Piezoelectric detectors have difficulties to achieve high sensitivity, wide bandwidth, and wide directivity simultaneously. These characteristics are required to obtain good PAT imaging quality. Microrings possess these characteristics, as described above. The high sensitivity of microrings enables PAT imaging with sufficient SNR at low laser fluence. Besides the sensitivity, we demonstrated the ability to image different scales of objects owing to the exceptionally wide bandwidth, which can potentially be used in imaging multi-scale vasculatures or tissues. In addition, utilizing the wide acceptance angle and wide bandwidth of microrings, the uniform high resolution in PAT over a large imaging area has been produced. Numerical simulation to evaluate the resolution as a function of microring's sizes at different imaging positions has also been plotted. Following the simulation work, the improved experimental PAT images were clearly depicted.

The major portion of the work contained in Chapter 3 were published in Journal of Biomedical Optics and IEEE Transactions on Ultrasonics, Ferroelectrics, and Frequency Control, and presented at 2009 SPIE Photonics West. The relevant citations are:

- **S.-L. Chen**, T. Ling, and L. J. Guo, "Low-noise small size microring ultrasonic detectors for high resolution photoacoustic imaging," Journal of Biomedical Optics, vol. 16, 056001, 2011.
- **S.-L. Chen**, S.-W. Huang, T. Ling, S. Ashkenazi, and L. J. Guo, "Polymer microring resonators for high-sensitivity and wideband photoacoustic imaging," IEEE Transactions on Ultrasonics, Ferroelectrics, and Frequency Control, vol. 56, pp. 2482-2491, 2009.
- **S.-L. Chen**, S.-W. Huang, T. Ling, S. Ashkenazi, and L. J. Guo, "Wideband photoacoustic tomography using polymer microring resonators," Proc. SPIE 7177, 71772B, 2009.

The main contributions of this work are:

1. Demonstrated the significantly improved imaging quality of PAT using microring detectors.
2. For high-sensitivity photoacoustic imaging, a 49 μm black bead was imaged at a low laser fluence of 0.35 mJ/cm^2 using good microring resonators. Compared with our previous results using poor microring resonators, a high laser fluence of 112 mJ/cm^2 was needed to obtain good SNR.
3. For wideband PAT, we compared the imaging performance of black beads using microring resonators and piezoelectric detectors. The former was able to faithfully

detect both the boundaries and the inner structure. Piezoelectric detectors can only preserve one of the two aspects. Moreover, a high resolution of 12.5 μm was obtained by microrings because of their wideband response.

4. For high-resolution PAT over a large imaging area, we compared the imaging performance of black beads using 40 μm microring resonators and 500 μm piezoelectric detectors with similar NEP and wideband response. In imaging 50 μm black beads, microrings produced high-resolution imaging over a 16-mm-diameter imaging area while the 500 μm piezoelectric detectors only obtained high-resolution imaging over a small area around the scanning center.

In **Chapter 4**, we demonstrated pure optical photoacoustic microscopy (PAM) based on the microring resonators. Piezoelectric detectors have difficulties to achieve high sensitivity and wide bandwidth simultaneously. These characteristics are important to obtain good PAM imaging quality. Microrings are good candidates in PAM applications. The *in vivo* and *ex vivo* PAM imaging using microrings were conducted for the first time. By taking advantage of the high sensitivity and wideband response of microrings, the good imaging SNR and high resolutions were obtained. With the pure optical system, the individual red blood cells can be discerned more clearly because of a much higher axial resolution of 8 μm. As a comparison, an Onda hydrophone with similar NEP produced a similar SNR but low axial resolution of 105 μm due to its very limited bandwidth. We also theoretically analyzed a maximum ultrasound modulation frequency of 570 MHz for 1.4-μm-thick microring resonators.

The major portion of the work contained in Chapter 4 was published in Optics Express. The relevant citation is:

- Z. Xie,[+] **S.-L. Chen**,[+] T. Ling,[+] L. J. Guo, P. L. Carson, X. Wang, "Pure optical photoacoustic microscopy," Optics Express, vol. 19, pp. 9027-9034, 2011. ([+]: Equal contribution)

The main contributions of this work are:

1. Microring ultrasonic resonators were applied to *in vivo* photoacoustic imaging for the first time.
2. The high axial resolution of 8 μm was obtained using pure optical PAM based on microring resonators, while a commercial hydrophone produced a low axial resolution of 105 μm.

In **Chapter 5**, photoacoustic endoscopy based on microrings was demonstrated. The sensitivity of piezoelectric detectors decreases as their element size decreases. We can potentially make the microring device less than 1 mm for endoscopic photoacoustic applications without sacrificing the sensitivity. In this work, we have fabricated a 5-mm-diameter probe including a fiber to deliver 532 nm pulsed laser and a microring detector on a fused silica transparent substrate. A high radial resolution of 21 μm was obtained by imaging a 6 μm carbon fiber. As a comparison, other types photoacoustic probes based on piezoelectric detectors achieved a radial resolution of around 40 μm or larger.

The major portion of the work contained in Chapter 5 was presented 2011 SPIE Photonics West. The relevant citation is:

- **S.-L. Chen**, T. Ling, H. W. Baac, and L. J. Guo, "Photoacoustic endoscopy using polymer microring resonators," Proc. SPIE 7899, 78992T, 2011.

  The main contributions of this work are:

1. Developed a fabrication process of microrings on fused silica substrates.
2. A 5 mm miniaturized probe capable of photoacoustic excitation and detection were fabricated. The high radial resolution of 21 μm was higher than other types of endoscopic photoacoustic probes.

In **Chapter 6**, we proposed a photoacoustic correlation spectroscopy (PACS) technique. Current blood velocimeters such as laser Doppler velocimetry and optical/ultrasound particle image velocimetry have limited sensitivity and resolution, restricting their applications to measure blood flow speed in capillaries. We expected that PACS was able measure it. PACS was motivated from fluorescence correlation spectroscopy to obtain dynamic information from light-absorbing particles. As a proof-of-concept experiment, we first showed the PACS application to low-speed flow measurement, ~15 μm/s. The high sensitivity of microring resonators enabled high SNR from tracer particles. As a practical application of PACS, we demonstrated *in vivo* flow speed measurement of capillaries in a chick embryo model. The work suggests a fairly simple method to measure flow speeds of capillaries. Other techniques might have difficulties to measure blood speed in capillaries due to the low signal contrast and/or poor resolutions.

The major portion of the work contained in Chapter 6 were published in Optics Letters and presented at 2010 SPIE Photonics West. The relevant citations are:

- **S.-L. Chen**,[+] Z. Xie,[+] P. L. Carson, X. Wang, L. J. Guo, "*In vivo* flow speed measurement of capillaries by photoacoustic correlation spectroscopy," Optics Letters, vol. 36, pp. 4017-4019, 2011. ([+]: Equal contribution)
- **S.-L. Chen**, T. Ling, S.-W. Huang, H. W. Baac, and L. J. Guo, "Photoacoustic correlation spectroscopy and its applications to low speed flow measurement," Optics Letters, vol. 35, pp. 1200-1202, 2010.
- **S.-L. Chen**, T. Ling, S.-W. Huang, H. W. Baac, Y.-C. Chang, and L. J. Guo, "Photoacoustic correlation technique for low-speed flow measurement," Proc. SPIE 7564, 75642I, 2010.

In addition, this work has been selected for publication in the Virtual Journal for Biomedical Optics:

- Optics Letters, vol. 36, pp. 4017-4019, 2011.
- Optics Letters, vol. 35, pp. 1200-1202, 2010.

The main contributions of this work are:

1. Proposed a photoacoustic correlation spectroscopy technique for the first time.
2. Demonstrated low-speed flow measurement of 15 μm/s by the PACS technique.
3. Demonstrated the PACS technique for *in vivo* blood flow speed measurement in capillaries in a chick embryo model. Other techniques might have difficulties to measure blood speed in capillaries due to the low signal contrast and/or poor resolutions.

In **Chapter 7**, terahertz (THz) detection by the photoacoustic method is implemented by combing a highly efficient photoacoustic transmitter, carbon nanotube-

polydimethylsiloxane composite, and the highly sensitive microring resonators. A bolometer and a pyroelectric detector are commonly used to measure THz power. However, the former requires low temperature operation, resulting in high costs for cooling, and the latter operates at low modulation frequency, limiting real-time detection. We calibrated the sensitivity as 1.4 mV/μW of PA-based THz detector. Besides, we showed its feasibility for real-time THz detection. THz imaging by PA-based detection and pyroelectric detection are also compared. The PA-based THz detector provides several advantages such as small size, operation at room temperature, fast response on the order of μs.

The major portion of the work contained in Chapter 7 was in preparation and will be submitted. The relevant citation is:

- S.-L. Chen et al., "Photoacoustic detection of terahertz," in preparation.

The main contributions of this work are:

1. Proposed a new approach to THz detection.
2. Calibrated the sensitivity of PA-based THz detector as 1.4 mV/μW.
3. Demonstrated its feasibility for real-time THz detection, which is difficult by a bolometer or a pyroelectric detector.
4. Compared THz imaging by PA-based THz detector and pyroelectric detector and obtained similar images.

8.2 Future work

8.2.1 Multi-scale photoacoustic imaging

Microrings, with the unique merit of broadband response, enable the imaging of various sizes of objects, which generate different photoacoustic frequencies. Obviously, the imaging-depth limit is dependent on object sizes, i.e. frequencies. To quantitatively evaluate the frequency-dependent penetration for photoacoustic imaging using our low noise and wideband microring detectors, the acoustic pressure as a function of depth and frequency are analyzed. We adopt a reflection-mode photoacoustic setup in the evaluation. The noise-equivalent pressure (NEP) of microrings is about 20 Pa over a full bandwidth. Consider a blood-like water-based object with an effective optical absorption coefficient of $\mu_{eff}^{blood} = 5\,\mathrm{cm}^{-1}$ (typical for blood at 800 nm wavelength) embedded in a normal water-based tissue with an effective optical absorption coefficient of $\mu_{eff}^{tissue} = 1\,\mathrm{cm}^{-1}$. The acoustic pressure at bands of $0.5f_c$ to $1.5f_c$ at the detector surface, generated by light absorption in the object at a depth z, is given by

$$P(z, f_c) = \frac{\beta c^2 (\mu_{\mathrm{eff}}^{\mathrm{blood}} - \mu_{\mathrm{eff}}^{\mathrm{tissue}}) J_0 \exp(-\mu_{\mathrm{eff}}^{\mathrm{tissue}} z)}{2C_p z} \times R \times 10^{-af_c z/20} \times k \quad (8.1)$$

where $J_0 = 20$ mJ/cm^2 is the surface optical fluence, R is the object radius, $c = 1500$ m/s is the sound speed, $\beta = 360\times10^{-6}$ K^{-1} is the thermal expansion coefficient, $C_P = 4.2$ kJ/kg/K is the specific heat capacity, $a = 5$ dB/cm/MHz is the ultrasound attenuation in the tissue, and k is a scaling factor due to a 100% bandwidth, instead of full bandwidth, used. Note that to match the different frequency bands, different object radius $R = c/(3f_c)$ as a function of central frequency is used. At this relation, k is a constant of 0.50. Figure 8.1

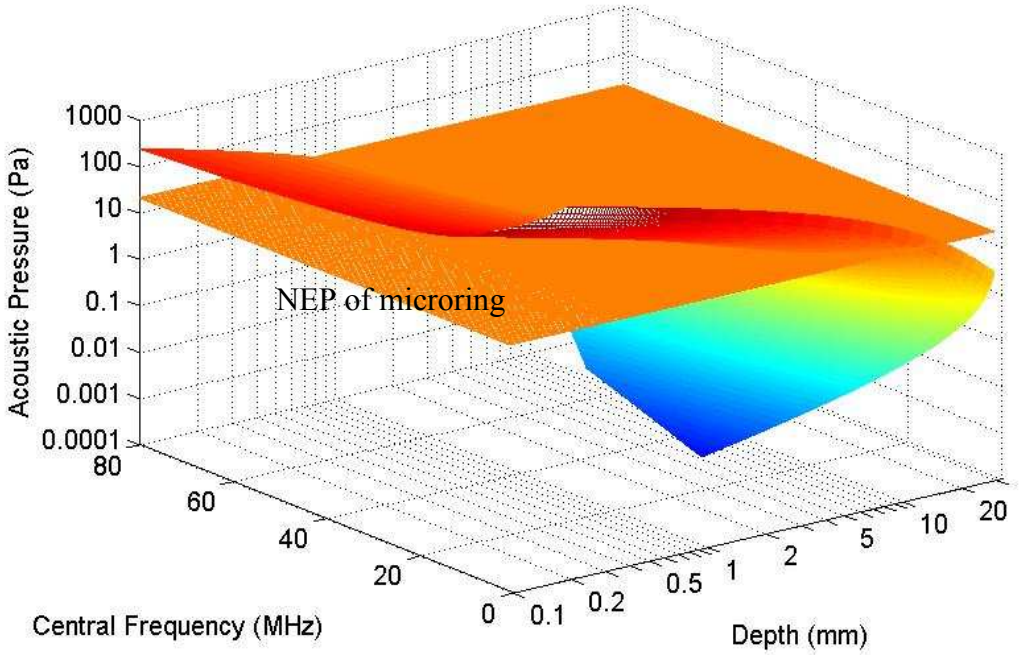

Figure 8.1 Acoustic pressure as a function of depth and frequency bands. Microring's NEPs are also plotted for comparisons.

shows the fusion plot of microring's NEPs as a function of frequency only and acoustic pressure as a function of depth and frequency. From Figure 8.1, we can obtain the imaging depth at different frequency bands, as shown in Figure 8.2. The results show the multi-scale capability of microrings, which means that with a single device, high resolution can be achieved at small imaging depth and capturing the high frequency components; and high imaging depth can be achieved due to flat response at low frequency.

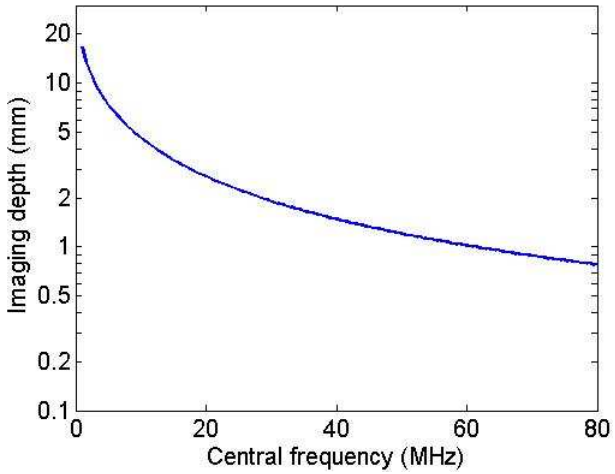

Figure 8.2 Imaging depth as a function of different frequency bands.

8.2.2 Improved probe for photoacoustic endoscopy

We have demonstrated an integrated probe in Chapter 6 using microrings on transparent substrates and a fiber to deliver excitation light source. We have done the preliminary calibration for the imaging purpose. To improve the probe for more clinical application, more advanced design such as fast imaging capability and further reduction of size are needed. For the former, a mechanical micromotor to rotate a mirror is very promising to replace rotary scanning of the whole device. The imaging method in most photoacoustic endoscopy scans the laser on the region of interest. Mirror rotation using a micromotor can effectively increase the speed by quickly scanning the laser light. For the latter, currently the device size is limited by the fact that two fibers are needed to access the input and output bus waveguides of microring resonators. To use only one fiber as input and output, the circulator is one potential solution. Other than faster scanning and smaller size, this dual imaging modality can be equipped to acquire complementary

information. For example, pulse-echo ultrasound imaging can provide the anatomical details. Combining with the functional information from photoacoustic imaging, the multimodality imaging by such probe are quite useful for disease diagnosis and image-guided treatment. Therefore, further study which can shape the probe into more practical application is desired.

8.2.3 Very high frequency calibration of microrings

In Chapter 4, we demonstrated that the theoretical limit of detector's frequency response can be up to sub GHz. However, the calibration of several hundreds of MHz is challenging due to fabrication difficulties of such high-frequency transducers. Photoacoustic method may provide a opportunity to generate sub-GHz acoustic signals [151]. To generate such high frequencies, a short laser pulse is required. For example, to generate more than 500 MHz signals, the laser pulse should be less than 1 ns. A thin film absorber may be good for the calibration. Assuming a uniform absorption by a water-based thin film, Figure 8.3 shows the generated frequency spectrum with different pulse durations and film thickness. Besides, a close distance between the absorber and microring detectors is required to minimize the high-frequency attenuation. Microring's ability to detect sub-GHz ultrasound can find applications in either biomedical imaging or testing industry.

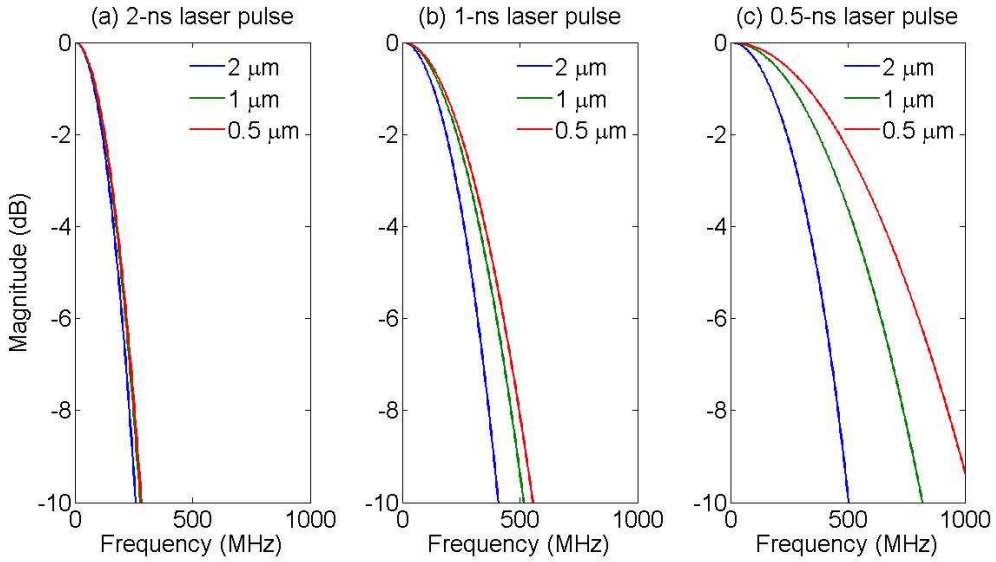

Figure 8.3 Generated frequency spectrum by absorbers with film thickness of 2, 1, 0.5 μm and the pulsed laser with durations of (a) 2 ns, (b) 1 ns, and (c) 0.5 ns, respectively.

Bibliography

[1] A. A. Oraevsky and A. A. Karabutov, in Biomedical Photonics Handbook, vol. PM125 (ed. Vo-Dinh, T.) Ch. 34, pp. 3401–3434, CRC Press, 2003.

[2] M. H. Xu and L. V. Wang, "Photoacoustic imaging in biomedicine," Rev. Sci. Instrum., vol. 77, 041101, 2006.

[3] L. V. Wang (ed.), Photoacoustic Imaging and Spectroscopy, CRC Press, 2009.

[4] O. Oralkan, A. S. Ergun, J. A. Johnson, M. Karaman, U. Demirci, K. Kaviani, T. H. Lee, and B. T. Khuri-Yakub, "Capacitive micromachined ultrasonic transducers: next generation arrays for for acoustic imaging?," IEEE Trans. Ultrason. Ferroelect. Freq. Contr., vol. 49, pp. 1596–1610, 2002.

[5] B. Bayram, E. Haeggstrom, G. G. Yaralioglu, and B. T. Khuri-Yakub, "A new regime for operating capacitive micromachined ultrasonic transducers," IEEE Trans. Ultrason. Ferroelect. Freq. Contr., vol. 50, pp. 1184–1190, 2003.

[6] O. Oralkan, A. S. Ergun, C. H. Cheng, J. A. Johnson, M. Karaman, T. H. Lee, and B. T. Khuri-Yakub, "Volumetric ultrasound imaging using 2-D CMUT arrays," IEEE Trans. Ultrason. Ferroelect. Freq. Contr., vol. 50, pp. 1581–1594, 2003.

[7] D. T. Yeh, O. Oralkan, I. O. Wygant, M. O'Donnell, and B. T. Khuri-Yakub, "3-D ultrasound imaging using a forward-looking CMUT ring array for intravascular/intracardiac applications," IEEE Trans. Ultrason. Ferroelect. Freq. Contr., vol. 53, pp. 1202–1211, 2006.

[8] Y. L. Huang, E. Haeggstrom, B. Bayram, X. F. Zhuang, A. S. Ergun, C. H. Cheng, and B. T. Khuri-Yakub, "Comparison of conventional and collapsed region operation of capacitive micromachined ultrasonic transducers," IEEE Trans. Ultrason. Ferroelect. Freq. Contr., vol. 53, pp. 1918–1932, 2006.

[9] H. jagannathan, G. G. Yaralioglu, A. S. Ergun, F. L. Degertekin, and B. T. Khuri-Yakub, "Micro-fluidic channels with integrated ultrasonic transducers," Proc. 2001 IEEE Ultrason. Symp., pp. 859–862, 2001.

[10] A. S. Ergun, Y. Huang, C. H. Cheng, O. Oralkan, J. Johnson, H. Jagannathan, U. Demirci, G. G. Yaralioglu, M. Karaman, and B. T. Khuri-Yakub, "Broadband capacitive micromachined ultrasonic transducers ranging from 10 kHz to 60 MHz for imaging arrays and more," Proc. 2002 IEEE Ultrason. Symp., pp. 1013–1017, 2002.

[11] C. Daft, S. Calmes, D. da Graca, K. Patel, P. Wagner, and I. Ladabaum, "Microfabricated ultrasonic transducers monolithically integrated with high voltage electronics," Proc. 2004 IEEE Ultrason. Symp., pp. 493–496, 2004.

[12] C. Daft, P. Wagner, B. Bymaster, S. Panda, K. Patel, and I. Ladabaum, "cMUTs and electronics for 2D and 3D imaging: monolithic integration, in-handle chip sets and system implications," Proc. 2005 IEEE Ultrason. Symp., pp. 463–474, 2005.

[13] I. Wygant, X. Zhuang, D. Yeh, O. Oralkan, A. S. Ergun, M. Karaman, and B. T. Khuri-Yakub, "Integration of 2S CMUT arrays with front-end electronics for volumetric ultrasound imaging," IEEE Trans. Ultrason. Ferroelect. Freq. Contr., vol. 55, pp. 327-342, 2008.

[14] D. Utkan, A. S. Ergun, Ö. Oralkan, and M. Karaman, and B. T. Khuri-Yakub, "Forward-Viewing CMUT Arrays for Medical Imaging," IEEE Trans. Ultrason. Ferroelect. Freq. Contr., vol. 51, pp. 886–894, 2004.

[15] S. Zhou, JA. Hossack, "Reducing inter-element acoustic crosstalk in capacitive micromachined ultrasound transducers," IEEE Trans. Ultrason. Ferroelect. Freq. Contr., vol. 54, pp. 1217–1228, 2007.

[16] S. Ashkenazi, C.-Y. Chao, L. J. Guo, and M. O'Donnell, "Ultrasound detection using polymer microring optical resonator," Appl. Phys. Lett., vol. 85, pp. 5418–5420, 2004.

[17] C-Y. Chao, S. Ashkenazi, S. W. Huang, M. O'Donnell, and L. J. Guo, "High-frequency ultrasound sensors using polymer microring resonators," IEEE Trans. Ultrason. Ferroelect. Freq. Contr., vol. 54, pp. 957–965, 2007.

[18] A. Maxwell, S.-W. Huang, T. Ling, J.-S. Kim, S. Ashkenazi, and L. J. Guo, "Polymer microring resonators for high-frequency ultrasound detection and imaging," IEEE J. Sel. Top. Quantum Electron., vol. 14, pp. 191-197, 2008.

[19] S.-W. Huang, S.-L. Chen, T. Ling, A. Maxwell, M. O'Donnell, L. J. Guo, and S. Ashkenazi, "Low-noise wideband ultrasound detection using polymer microring resonators," Appl. Phys. Lett., vol. 92, 193509, 2008.

[20] S.-L. Chen, S.-W. Huang, T. Ling, S. Ashkenazi, and L. J. Guo, "Polymer microring resonators for high-sensitivity and wideband photoacoustic imaging," IEEE Trans. Ultrason. Ferroelect. Freq. Contr., vol. 56, pp. 2482–2491, 2009.

[21] H. W. Baac, T. Ling, S.-W. Huang, S. Ashkenazi, and L. J. Guo, "Characterization of optical microring ultrasound detector by using a high frequency focused photoacoustic transmitter," Appl. Phys. Lett., vol. 95, 144105, 2009.

[22] T. Ling, S.-L. Chen, and L. J. Guo, "Fabrication and characterization of high Q polymer micro-ring resonator and its application as a sensitive ultrasonic detector," Opt. Express, vol. 19, pp. 861-869, 2011.

[23] S.-L. Chen, T. Ling, and L. Jay Guo, "Low-noise small size microring ultrasonic detectors for high-resolution photoacoustic imaging," J. Biomed. Opt., vol. 16, 056001, 2011.

[24] T. Ling, S.-L. Chen, and L. J. Guo, "High-sensitivity and wide-directivity ultrasound detection using high Q polymer micro-ring resonators," App. Phys. Lett., vol. 98, 204103, 2011.

[25] J. P. Monchalin, "Optical detection of ultrasound at a distance using a confocal Fabry-Perot interferometer," Appl. Phys. Lett. vol. 47, pp. 14–16, 1985.

[26] J. P. Monchalin, "Optical detection of ultrasound," IEEE Trans. Ultrason. Ferroelect. Freq. Contr., vol. 33, pp. 485–499, 1986.
[27] J. P. Monchalin, and R. Heon, "Broadband optical detection of ultrasound by optical sideband stripping with a confocal Fabry-Perot," Appl. Phys. Lett. vol. 55, pp. 1612–1614, 1989.
[28] H. Sontag and A. C. Tam, "Optical detection of nanosecond acoustic pulses," IEEE Trans. Ultrason. Ferroelect. Freq. Contr., vol. 33, pp. 500–506, 1986.
[29] R. J. Dewhurst, and Q. Shan, "Modeling of confocal Fabry-Perot interferometers for the measurement of ultrasound," J. Meas. Sci. Technol., vol. 5, pp. 655–662, 1994.
[30] Q. Shan, C. M. Chen, and R. J. Dewhurst, "A conjugate optical Fabry-Perot interferometer for enhanced ultrasound detection," J. Meas. Sci. Technol., vol. 6, pp. 921–928, 1995.
[31] P. C. Beard and T. N. Mills, "Extrinsic optical-fiber ultrasound sensor using a thin polymer film as a low-finesse Fabry-Perot interferometer," Appl. Opt., vol. 35, pp. 663–675, 1996.
[32] P. C. Beard, F. Perennes, and T. N. Mills, "Transduction mechanisms of the Fabry- Perot polymer film sensing concept for wideband ultrasound detection," IEEE Trans. Ultrason. Ferroelect. Freq. Contr., vol. 46, pp. 1575–1582, 1999.
[33] P. C. Beard, A. Hurrell, T. N. Mills, "Characterization of a polymer film optical fiber hydrophone for the measurement of ultrasound fields for use in the range 1 to 20 MHz: a comparison with PVDF needle and membrane hydrophones," IEEE Trans. Ultrason. Ferroelect. Freq. Contr., vol. 47, pp. 256–264, 2000.
[34] P. C. Beard, "2D ultrasound receive array using an angle-tuned Fabry Perot polymer film sensor for transducer field characterization and transmission ultrasound imaging," IEEE Trans. Ultrason. Ferroelect. Freq. Contr., vol. 52, pp. 1002–1012, 2005.
[35] B. T. Cox, and P. C. Beard, "Frequency dependent directivity of a planar Fabry Perot polymer film ultrasound sensor," IEEE Trans. Ultrason. Ferroelect. Freq. Contr., vol. 54, pp. 394–404, 2007.
[36] J. D. Hamilton, C. J. Brooks, G. L. Vossler, and M. O'Donnell, "High frequency ultrasound imaging using active optical detection," IEEE Trans. Ultrason. Ferroelect. Freq. Contr., vol. 45, pp. 719–727, 1998.
[37] J. D. Hamilton, T. Buma, M. Spisar, and M. O'Donnell, "High frequency optoacoustic arrays using etalon detection," IEEE Trans. Ultrason. Ferroelect. Freq. Contr., vol. 47, pp. 160–169, 2000.
[38] S. Ashkenazi, Y. Hou, T. Buma, and M O'Donnell, "Optoacoustic imaging using thin polymer etalon," Appl. Phys. Lett., vol. 86, 134102, 2005.
[39] S.-W. Huang, Y. Hou, S. Ashkenazi, and M O'Donnell, "High-resolution ultrasonic imaging using an etalon detector array," Appl. Phys. Lett., vol. 93, 113501, 2008.
[40] J. G. Laufer, P. C. Beard, and T. N. Mills, "Comparison of the Photothermal sensitivity of an interferometric optical fiber probe with pulsed photothermal radiometry," Rev. Sci. Instrum., vol. 73, pp. 3345–3352, 2002.

[41] V. Wilkens, "Characterization of an optical multilayer hydrophone with constant frequency response in the range from 1 to 75 MHz," J. Acoust. Soc. Amer., vol. 113, pp. 1431–1438, 2003.

[42] V. Govindan and S. Ashkenazi, "Polymer Bragg waveguide ultrasound detectors," Proc. SPIE, vol. 7899, 78991E-1, 2011.

[43] R. A. Smith, V. Cokkinides, and H. J. Eyre, "American cancer society guidelines for the early detection of cancer, 2003," CA Cancer J. Clin., Vol. 53, pp. 27–43, 2003.

[44] U. Pastorino, M. Bellomi, C. Landomi, E. D. Fiori, P. Arnaldi, M. Picchio, G. Pelosi, P. Boyle, and P. Fazio, "Early lung-cancer detection with spiral CT and positron emission tomography in heavy smokers: 2-year results," Lancet, vol. 362, pp. 593–597, 2003.

[45] A. W. H. Lin, N. A. Lewinski, J. L. West, N. J. Halas, and R. A. Drezek, "Optically tunable nanoparticles contrast agents for early cancer detection: model- based analysis of gold nanoshells," J. Biomed. Opt., vol. 10, 064035, 2005.

[46] C. I. Henschke, D. I. McCauley, D. F. Yankelevitz, D. P. Naidich, G. McGuinness, O. S. Miettinen, D. M. Libby, M. W. Pasmantier, J. Koizumi, N. K. Altorki, and J. P. Smith, "Early lung cancer action project: overall design and findings from baseline screening," Lancet, vol. 354, pp. 99–105,1999.

[47] S. Diederich, D. Wormanns, M. Semik, M. Thomas, H. Lenzen, N. Roos, and W. Heindel, "Screening for early lung cancer with low-dose spiral CT: prevalence in 817 asymptomatic smokers," Radiology, vol. 222, pp. 773–781, 2002.

[48] P. D. DePriest and C. P. DeSimone, "Ultrasound screening for the early detection of ovarian cancer," J. Clin. Oncol., vol. 21, pp. 194–199, 2003.

[49] A. Blana, B. Walter, S. Rogenhofer, and W. F. Wieland, "High-intensity focused ultrasound for the treatment of localized prostate cancer: 5-year experience," Urology, vol. 63, pp. 297–300, 2004.

[50] K. F. Pirollo, J. Dagata, P. Wang, M. Freedman, A. Vladar, S. Fricke, L. Ileva, Q. Zhou, and E. H. Chang, "A tumor-targeted nanodelivery system to improve early MRI detection of cancer," Mol. Imaging, vol. 5, pp. 41–52, 2006.

[51] T. Q. Xie, M. L. Zeidel, and Y. T. Pan, "Detection of tumorigenesis in urinary bladder with optical coherence tomography: optical characterization of morphological changes," Opt. Express, vol. 10, pp. 1431–1443, 2002.

[52] J. G. Fujimoto, "Optical coherence tomography for ultrahigh resolution in vivo imaging," Nat. Biotechnol., vol. 21, pp. 1361–1367, 2003.

[53] E. S. Matheny, N. M. Hanna, W. G. Jung, Z. Chen, P. Wilder-Simth, R. Mina-Araghi, and M. Brenner, "Optical coherence tomography of malignancy in hamster cheek pounces," J. Biomed. Opt., vol. 9, pp. 978–981, 2004.

[54] B. Pogue, M. Testorf, T. McBride, U. Osterberg, and K. Paulsen, "Instrumentation and design of a frequency-domain diffuse optical tomography imager for breast cancer detection," Opt. Express, vol. 1, pp. 391–403, 1997.

[55] S. R. Arridge, and W. R. B. Lionheart, "Nonuniqueness in diffusion-based optical tomography," Opt. Lett., vol. 23, pp. 882–884, 1998.

[56] J. P. Culver, R. Choe, M. J. Holboke, L. Zubkov, T. Durduran, A. Slemp, V.Ntziachristos, B. Chance, and A. G. Yodh, "Three-dimensional diffuse optical tomography in the parallel plane transmission geometry: evaluation of a hybrid frequency domain/continuous wave clinical system for breast imaging," Med. Phys., vol. 30, pp. 235–247, 2003.

[57] L. Sun, W. D. Richard, J. M. Cannata, C. C. Feng, J. A. Johnson, J. T. Yen, and K. K. Shung, "A high-frame rate high-frequency ultrasonic system for cardiac imaging in mice," IEEE Trans. Ultrason. Ferroelect. Freq. Contr., vol. 54, pp. 1648–1655, 2007.

[58] A. A. Oraevsky, A. A. Karabutov, S. V. Solomatin, E. V. Savateeva, V. A. Andreev, Z. Gatalica, H. Singh, and R. D. Fleming, "Laser optoacoustic imaging of breast cancer in vivo," Proc. SPIE, vol. 4256, pp. 6–15, 2001.

[59] A. A. Oraevsky, E. V. Savateeva, S. V. Solomatin, A. A. Karabutov, V. G. Andreev, Z. Gatalica, T. Khamapirad, and P. M. Henrichs, "Optoacoustic imaging of blood for visualization and diagnostics of breast cancer," Proc. SPIE, vol. 4618, pp. 81–94, 2002.

[60] X. Wang, Y. Pang, G. Ku, X. Xie, G. Stoica, and L. V. Wang, "Non-invasive laser-induced photoacoustic tomography for structural and functional imaging of the brain in vivo," Nat. Biotech., vol. 21, pp. 803–806, 2003.

[61] L. V. Wang, "Ultrasound-mediated biophotonic imaging: a review of acousto-optical tomography and photo-acoustic tomography," J. Disease Markers, vol. 19, pp. 123–138, 2004.

[62] V. Ntziachristos, J. Ripoll, L. V. Wang, and R. Weissleder, "Looking and listening to light: the revolution of photonic imaging," Nat. Biotech., vol. 23, pp. 313–320, 2005.

[63] Y. Xu, and L. V. Wang, "Rhesus monkey brain imaging through skull intact skull with thermoacoustic tomography," IEEE Trans. Ultrason. Ferroelect. Freq. Contr., vol. 53, pp. 542–548, 2006.

[64] D. Lapotko, E. Lukianova, M. Potapnev, O. Aleinikova, A. A. Oraevsky, "Method of laser activated nano-thermolysis for elimination pf tumor cells," Cancer Lett., vol. 239, pp. 36–45, 2006.

[65] H. F. Zhang, K. Maslov, M. Sivaramakrishnan, G. Stoica, and L. V. Wang, "Imaging of hemoglobin oxygen saturation variations in single vessels in vivo using photoacoustic microscopy," Appl. Phys. Lett., vol. 90, 053901, 2007.

[66] L. Li, R. Zemp, G. Lungu, G. Stoica, and L. V. Wang, "Photoacoustic imaging of gene LacZ expression in living mice," J. Biomed. Opt., vol. 12, 020504, 2007.

[67] R. Zemp, M. Li, R. Bitton, K. K. Shung, G. Stoica, and L. V. Wang, "Photoacoustic imaging of the microvasculature with a high-frequency ultrasound array transducer," Journal of Biomedical Optics, vol. 12, 010501, 2007.

[68] S. Sethuraman, S. R. Aglyamov, J. H. Amirian, R. W. Smalling, and S. Y. Emelianov, "Intravascular photoacoustic imaging using an IVUS imaging catheter," IEEE Trans. Ultrason. Ferroelectr. Freq. Control, vol. 54, pp. 978–986, 2007.

[69] S. Sethuraman, J. H. Amirian, S. H. Litovsky, R. W. Smalling, and S. Y. Emelianov, "Ex vivo characterization of atherosclerosis using intravascular photoacoustic imaging," Opt. Express, vol. 15, pp. 16657–16666, 2007.
[70] F. Kong, Y. C. Chen, H. O. Lloyd, R. H. Silverman, H. H. Kim, J. M. Cannata, and K. K. Shung, "High-resolution photoacoustic imaging with focused laser and ultrasonic beams," Appl. Phys. Lett., vol. 94, 033902, 2009.
[71] B. Wang, J. L. Su, A. B. Karpiouk, K. V. Sokolov, R. W. Smalling, and S. Y. Emelianov, "Intravascular photoacoustic imaging," IEEE J. Sel. Top. Quantum Electron., vol. 16, pp. 588-599, 2010.
[72] S. Y. Chou, P. R. Krauss, W. Zhang, L. Guo, and L. Zhuang, "Sub-10 nm imprint lithography and applications," J. Vac. Sci. Technol. B, vol. 15, pp. 2897-2904, 1997.
[73] C.-Y. Chao and L. J. Guo, "Polymer micro-ring resonators fabricated by nanoimprint technique," J. Vac. Sci. & Technol. B., vol. 20, pp. 2862-2866, 2002.
[74] E. D. Zhang and P. Beard, "Ultrahigh-sensitivity, wideband Fabry-Perot ultrasound sensors as an alternative to piezoelectric PVDF transducers for biomedical photoacoustic detection," Proc. SPIE, vol. 5320, pp. 222-229, 2004.
[75] G. J. Diebold, T. Sun, and M. I. Khan, "Photoacoustic monopole radiation in one, two, and three dimensions," Phys. Rev. Lett., vol. 67, pp. 3384–3387, 1991.
[76] T. Buma, M. Spisar, and M. O'Donnell, "Thermoelastic generation of ultrasound using an erbium doped fiber amplifier", Proc.-IEEE Ultrason. Symp., pp. 1253-1256, 1999.
[77] J. M. Cannata, J. A. Williams, Q. Zhou, T. A. Ritter, and K. K. Shung, "Development of a 35-MHz piezo-composite ultrasound array for medical imaging," IEEE Trans. Ultrason. Ferroelectr. Freq. Control, vol. 53, pp. 224–236, 2006.
[78] D. T. Blackstock, Fundamentals of Physical Acoustics. NewYork: Wiley, 2000.
[79] M. A. Moehring and J. A. Ritcey, "Sizing emboli in blood using pulse doppler ultrasound—I: Verification of the EBR model," IEEE Trans. Biomed. Eng., vol. 43, pp. 572–580, 1996.
[80] J. Brandrup, E. H. Immergut, and E. A. Grulke, Polymer Handbook, 2nd ed. New York: Wiley, p. V-59, 1989.
[81] R. W. Warfield and M. C. Petree, "Thermodynamic properties of polystyrene and styrene," J. of Polym. Sci., vol. 55, pp. 497–505, 1961.
[82] S. Yang, D. Xing, Q. Zhou, L. Xiang, and Y. Lao, "Functional imaging of cerebrovascular activities in small animals using high-resolution photoacoustic tomography," Med. Phys., vol. 34, pp. 3294–3301, 2007.
[83] D. Razansky and V. Ntziachristos, "Hybrid photoacoustic fluorescence molecular tomography using finite-element-based inversion," Med. Phys., vol. 34, pp. 4293–4301, 2007.
[84] M.-L. Li, J.-T. Oh, X. Xie, G. Ku, W. Wang, C. Li, G. Lungu, G. Stoica, and L. V. Wang, "Simultaneous molecular and hypoxia imaging of brain tumors in vivo using spectroscopic photoacoustic tomography," Proc. IEEE, vol. 96, pp. 481–489, 2008.

[85] M. Xu and L. V. Wang, “Universal back-projection algorithm for photoacoustic computed tomography,” Phys. Rev. E, vol. 71, 016706, 2005.
[86] G. Ku, X. Wang, G. Stoica, and L. V. Wang, “Multiple-bandwidth photoacoustic tomography,” Phys. Med. Biol., vol. 49, pp. 1329–1338, 2004.
[87] G. Ku, B. D. Fomage, X. Jin, M. Xu, K. K. Hunt, and L. V. Wang, “Thermoacoustic and photoacoustic tomography of thick biological tissues toward breast imaging,” Technol. Cancer Res. Treat., vol. 4, pp. 559–565, 2005.
[88] M. Xu and L. V. Wang, “Analytic explanation of spatial resolution related to bandwidth and detector aperture size in thermoacoustic or photoacoustic reconstruction,” Phys. Rev. E, vol. 67, 056605, 2003.
[89] T. Loupas, S. D. Pye, and W. N. McDicken, “Deconvolution in medical ultrasonics: practical considerations,” Phys. Med. Biol., vol. 34, pp. 1691-1700, 1989.
[90] X. Yang, M.-L. Li, and L. V. Wang, “Ring-based ultrasonic virtual point detector with applications to photoacoustic tomography,” Appl. Phys. Lett., vol. 90, 251103, 2007.
[91] C. Li and L. V. Wang, “High-numerical-aperture-based virtual point detectors for photoacoustic tomography,” Appl. Phys. Lett., vol. 93, 033902, 2008.
[92] M. Xu, Y. Xu, and L. V. Wang, “Time-domain reconstruction algorithms and numerical simulations for thermoacoustic tomography in various geometries,” IEEE Trans. Biomed. Eng., vol. 50, pp. 1086-1099, 2003.
[93] X. Wang, Y. Xu, M. Xu, S. Yokoo, E. S. Fry, and L. V. Wang, “Photoacoustic tomography of biological tissues with high cross-section resolution: reconstruction and experiment,” Am. Assoc. Phys. Med., vol. 29, pp. 2799-2805, 2002.
[94] C. G. A. Hoelen and F. F. M. de Mul, “A new theoretical approach to photoacoustic signal generation,” J. of Acoust. Soc. Am., vol. 106, pp. 695-706, 1999.
[95] H. Li, S. Xie, and L. Lin, “Refractive index of bio-tissue and its thermal response,” CLEO/Pacific Rim '99, vol. 3, pp. 1018-1019, 1999.
[96] J. J. J. Dirckx, L. C. Kuypers, and W. F. Decraemer, “Refractive index of tissue measured with confocal microscopy,” J. of Biomed. Opt., vol. 10, 044014, 2005.
[97] H. F. Zhang, K. Maslov, G. Stoica, and L. V. Wang, “Functional photoacoustic microscopy for high-resolution and noninvasive in vivo imaging,” Nat. Biotech., vol. 24, pp. 848-851, 2006.
[98] H. F. Zhang, K. Maslov, and L. V. Wang, “In vivo imaging of subcutaneous structure using functional photoacoustic microscopy,” Nat. Protocal, vol. 2, pp. 797-804, 2007.
[99] K. H. Song, E. W. Stein, J. A. Margenthaler, and L. V. Wang, “Noninvasive photoacoustic identification of sentinel lymph nodes containing methylene blue in vivo in a rat model,” J. Biomed. Opt., vol. 13, 054033, 2008.
[100] E. W. Stein, K. Maslov, and L. V. Wang, “Noninvasive, in vivo imaging of the mouse brain using photoacoustic microscopy,” J. Appl. Phys., vol. 105, 102027, 2009.

[101] E. W. Stein, K. Maslov, and L. V. Wang, "Noninvasive, in vivo imaging of blood-oxygenation dynamics within the mouse brain using photoacoustic microscopy," J. Biomed. Opt., vol. 14, 020502, 2009.
[102] K. Maslov, H. F. Zhang, S. Hu, and L. V. Wang, "Optical-resolution photoacoustic microscopy for in vivo imaging of single capillaries," Opt. Lett., vol. 33, pp. 929–931, 2008.
[103] L. V. Wang and H. Wu, Biomedical Optics: Principles and Imaging, Wiley, 2007.
[104] E. Zhang, J. Laufer, and P. Beard, "Backward-mode multiwavelength photoacoustic scanner using a planar Fabry-Perot polymer film ultrasound sensor for high-resolution three-dimensional imaging of biological tissues," Appl. Opt., vol. 47, pp. 561-577, 2008.
[105] H. W. Baac, J. G. Ok, H. J. Park, T. Ling, S.-L. Chen, A. J. Hart and L. J. Guo, "Carbon nanotube composite optoacoustic transmitters for strong and high frequency ultrasound generation," Appl. Phys. Lett., vol. 97, 234104, 2010.
[106] D.K. Armani, T.J. Kippenberg, S.M. Spillane and K.J. Vahala, "Ultra-high-Q toroid microcavity on chip," Nature, vol. 421, pp. 925-928, 2003.
[107] Z. Xie, S. Jiao, H. F. Zhang, and C. A. Puliafito, "Laser-scanning optical-resolution photoacoustic microscopy," Optics Letters, vol. 34, pp. 1771-1773, 2009.
[108] S. Sethuraman, J. H. Amirian, S. H. Litovsky, R. W. Smalling, and S. Y. Emelianov, "Spectroscopic intravascular photoacoustic imaging to differentiate atherosclerotic plaques," Opt. Express, vol. 16, pp. 3362-3367, 2008.
[109] J.-M. Yang, K. Maslov, H.-C. Yang, Q. Zhou, K. K. Shung, and L. V. Wang, "Photoacoustic endoscopy," Opt. Lett., vol. 34, pp. 1591-1593, 2009.
[110] Y. Yuan, S. Yang, and D. Xing, "Preclinical photoacoustic imaging endoscope based on acoustic-optic coaxial system using ring transducer array," Opt. Lett., vol. 35, pp. 2266-2268, 2010.
[111] B.-Y. Hsieh, S.-L. Chen, T. Ling, L. J. Guo, and P.-C. Li, "Integrated intravascular ultrasound and photoacoustic imaging scan head," Opti. Lett., vol. 35, pp. 2892-2894, 2010.
[112] E. L. Elson, "Quick tour of fluorescence correlation spectroscopy from its inception," J. of Biomed. Opt., vol. 9, pp. 857-864, 2004.
[113] S. T. Hess, A. A. Heikal, and W. W. Webb, "Biological and chemical applications of fluorescence correlation spectroscopy: A review," Biochemistry, vol. 41, pp. 697-705, 2002.
[114] S. A. Kim, K. G. Heinze, M. N. Waxham, and P. Schwille, "Intracellular calmodulin availability accessed with two-photon cross-correlation," Proc. Natl. Acad. Sci., vol. 101, pp. 105-110, 2004.
[115] J. Irudayaraj and H. Yang, "Depth profiling of a heterogeneous food-packaging model using stepscan Fourier transform infrared photoacoustic spectroscopy," J. Food Eng., vol. 55, pp. 25-33, 2002.
[116] S. A. Telenkov and A. Mandelis, "Fourier-domain biophotoacoustic subsurface depth selective amplitude and phase imaging of turbid phantoms and biological tissue," J. Biomed. Opt., vol. 11, 044006, 2006.

[117] J. A. Martin and A. Roorda, "Pulsatility of parafoveal capillary leukocytes," Exp. Eye Res., vol. 88, pp. 356–360, 2009.
[118] J. Tam, P. Tiruveedhula, and A. Roorda, "Characterization of single-file flow through human retinal parafoveal capillaries using an adaptive optics scanning laser ophthalmoscope," Biomed. Opt. Express, vol. 2, pp. 781-793, 2011.
[119] S. Wolf, O. Arend, K. Schulte, TH Ittel and, M. Reim, "Quantification of retinal capillary density and flow velocity in patients with essential hypertension," Hypertension, vol. 23, pp. 464-467, 1994.
[120] P. Vennemann, R. Lindken, and J. Westerweel, "In vivo whole-field blood velocity measurement techniques," Exp Fluids, vol. 42, pp. 495–511, 2007.
[121] D. A. Christopher, P. N. Burns, J. Armstrong, and F. S. Foster, "A high-frequency continuous-wave Doppler ultrasound system for the detection of blood flow in the microcirculation," Ultrasound in Med. & Biol., vol. 22, pp. 1191-1203, 1996.
[122] J. Moger, S. J. Matcher, C. P. Winlove, and A. Shore, "The effect of multiple scattering on velocity profiles measured using Doppler OCT," J. Phys. D, vol. 38, pp. 2597-2605, 2005.
[123] H. Fang, K. Maslov, and L. V. Wang, "Photoacoustic Doppler effect from flowing small light-absorbing particles," Phys. Rev. Lett., vol. 99, 184501, 2007.
[124] H. Fang and L. V. Wang, "M-mode photoacoustic particle flow imaging," Opt. Lett., vol. 34, pp. 671-673, 2009.
[125] S.-L. Chen, T. Ling, S.-W. Huang, H. W. Baac, and L. J. Guo, "Photoacoustic correlation spectroscopy and its application to low-speed flow measurement," Opt. Lett., vol. 35, pp. 1200-1202, 2010.
[126] J. Yao, K. I. Maslov, Y. Shi, L. A. Taber, and L. V. Wang, "In vivo photoacoustic imaging of transverse blood flow by using Doppler broadening of bandwidth," Opt. Lett., vol. 35, pp. 1419-1421, 2010.
[127] R. G. M. Kolkman, E. Hondebrink, W. Steenbergen, and F. F. M. de Mul., "In vivo photoacoustic imaging of blood vessels using an extreme-narrow aperture sensor," IEEE J. Sel. Top. Quantum Electron., vol. 9, pp. 343-346, 2003.
[128] E. Haustein and P. Schwille, "Single-molecule spectroscopic methods," Current Opinion in Structural Biology, vol. 14, pp. 531-540, 2004.
[129] H. Asai, "Proposal of a simple method of fluorescence correlation spectroscopy for measuring the direction and magnitude of a flow of fluorophores," Japanese J. Appl. Phys., vol. 19, pp. 2279-2282, 1980.
[130] Y.-C. Chang, J. Y. Ye, T. Thomas, Y. Chen, J. R. Baker, and T. B. Norris, "Two-photon fluorescence correlation spectroscopy through a dual-clad optical fiber," Opt. Express, vol. 16, pp. 12640-12649, 2008.
[131] D. Vobornik, D. S. Banks, Z. Lu, C. Fradin, R. Taylor, and L. J. Johnston, "Fluorescence correlation spectroscopy with sub-diffraction-limited resolution using near-field optical probes," Appl. Phys. Lett., vol. 93, 163904, 2008.
[132] X. Pan, X. Shi, V. Korzh, H. Yu, and T. Wohland, "Line scan fluorescence correlation spectroscopy for three-dimensional microfluidic flow velocity measurements," J. Biomed. Opt., vol. 14, 024049, 2009.
[133] J. Mertz, C. Xu, and W. W. Webb, "Single-molecule detection by two-photon-excited fluorescence," Opt. Lett., vol. 20, pp.2532-2534, 1995.

[134] Z. Xie, S.-L. Chen, T. Ling, L. J. Guo, P. L. Carson, X. Wang, "Pure optical photoacoustic microscopy," Opt. Express, vol. 19, pp. 9027-9034, 2011.
[135] R. H. Köhler, P. Schwille, W. W. Webb, and M.R. Hanson, "Active protein transport through plastid tubules: velocity quantified by fluorescence correlation spectroscopy," J. Cell Sci., vol. 113, pp. 3921-3930, 2000.
[136] V. M. Belichenko and K. A. Shoshenko, "Circulatory system in chicken skeletal muscle in the second half of embryogenesis: Shape, blood flow, and vascular reactivity," Russ. J. of Dev. Biol., vol. 40, pp. 95-103, 2009.
[137] H. C. Yalcin, A. Shekhar, A. A. Rane, and J. T. Butcher, "An ex-ovo chicken embryo culture system suitable for imaging and microsurgery applications," J. Vis. Exp., vol. 44, doi: 10.3791/2154, 2010.
[138] P. Horn, M. M. Cortese-Krott, S. Keymel1, I. Kumara, S. Burghoff, J. Schrader, M. Kelm, and P. Kleinbongard, "Nitric oxide influences red blood cell velocity independently of changes in the vascular tone," Free Radical Research, vol. 45, pp. 653-661, 2011.
[139] H. Fang and L. V. Wang, "M-mode photoacoustic particle flow imaging," Opt. Lett., vol. 34, pp. 671-673, 2009.
[140] R. Baumann and H.-J. MEUER, "Blood oxygen transport in the early avian embryo," Physiol. Rev., vol. 72, pp. 941-965, 1992.
[141] B. S. Williams, "Terahertz quantum-cascade lasers," Nat. Photonics, vol. 1, pp. 517–525, 2007.
[142] M. Tani, P. Gu, M. Hyodo, K. Sakai, and T. Hidaka, "Generation of coherent terahertz radiation by photomixing of dual-mode lasers," Opt. Quantum Electron., vol. 32, pp. 503–520, 2000.
[143] L. V. Wang, "Tutorial on photoacoustic microscopy and computed tomography," IEEE J. Sel. Top. Quantum Electron., vol. 14, pp. 171–179, 2008.
[144] P. M. Ajayan, M. Terrones, A. de la Guardia, V. Huc, N. Grobert, B. Q. Wei, H. Lezec, G. Ramanath, and T. W. Ebbesen, "Nanotubes in a flash–ignition and reconstruction,"Science, vol. 296, p. 705, 2002.
[145] Y. Hou, J.-S. Kim, S. Ashkenazi, M. O'Donnell, and L. J. Guo, "Optical generation of high frequency ultrasound using two-dimensional gold nanostructure," Appl. Phys. Lett., vol. 89, 093901, 2006.
[146] K. Mizuno, J. Ishii, H. Kishida, Y. Hayamizu, S. Yasuda, D. N. Futaba, M. Yumura, and K. Hata, "A black body absorber from vertically aligned single-walled carbon nanotubes," Proc. Natl. Acad. Sci., vol. 106, pp. 6044–6047, 2009.
[147] A. Podzorov and G. Gallot, "Low-loss polymers for terahertz applications," Appl. Opt., vol. 47, pp. 3254–3257, 2008.
[148] T. Bartel, P Gaal, K. Reimann, M. Woerner, and T. Elsaesser, "Generation of single-cycle THz transients with high electric-field amplitudes," Opt. Lett., vol. 30, 2805–2807, 2005.
[149] K. Y. Kim, A. J. Taylor, J. H. Glownia, and G. Rodriguez, "Coherent control of terahertz supercontinuum generation in ultrafast laser-gas interactions," Nat. Photonics, vol. 2, pp. 605–609, 2008.

[150] J. H. Lehman, B. Lee, and N. Grossman, “Far infrared thermal detectors for laser radiometry using a carbon nanotube array,” Appl. Opt., vol. 50, pp. 4099–4104, 2011.
[151] U. Störkel, K. L. Vodopyanov, and W. Grill, “GHz ultrasound wave packets in water generated by an Er laser,” J. Phys. D: Appl. Phys., vol. 31, pp. 2258–2263, 1998.